HYPERSPECTRAL IMAGERY SUPER-RESOLUTION

A THESIS SUBMITTED TO
THE GRADUATE SCHOOL OF NATURAL AND APPLIED SCIENCES
OF
MIDDLE EAST TECHNICAL UNIVERSITY

BY
HASAN IRMAK

IN PARTIAL FULFILLMENT OF THE REQUIREMENTS
FOR
THE DEGREE OF DOCTOR OF PHILOSOPHY
IN
ELECTRICAL AND ELECTRONICS ENGINEERING

MAY 2017

Approval of the thesis:

HYPERSPECTRAL IMAGERY SUPER-RESOLUTION

submitted by **HASAN IRMAK** in partial fulfillment of the requirements for the degree of **Doctor of Philosophy in Electrical and Electronics Engineering Department, Middle East Technical University** by,

Prof. Dr. Gülbin Dural Ünver
Dean, Graduate School of **Natural and Applied Sciences** _______________

Prof. Dr. Tolga Çiloğlu
Head of Department, **Electrical and Electronics Engineering** _______________

Prof. Dr. Gözde Bozdağı Akar
Supervisor,
Electrical and Electronics Eng. Dept., METU _______________

Assist. Prof. Dr. Seniha Esen Yüksel
Co-supervisor,
Electrical and Electronics Eng. Dept., Hacettepe University _______________

Examining Committee Members:

Prof. Dr. Aydın Alatan
Electrical and Electronics Engineering Department, METU _______________

Prof. Dr. Gözde Bozdağı Akar
Electrical and Electronics Engineering Department, METU _______________

Prof. Dr. Yasemin Yardımcı Çetin
Informatics Institute, METU _______________

Assoc. Prof. Dr. Selim Aksoy
Computer Engineering Department, Bilkent University _______________

Assist. Prof. Dr. Alp Ertürk
Electronics and Communication Eng. Dept., Kocaeli University _______________

Date: _______________

I hereby declare that all information in this document has been obtained and presented in accordance with academic rules and ethical conduct. I also declare that, as required by these rules and conduct, I have fully cited and referenced all material and results that are not original to this work.

Name, Last Name: HASAN IRMAK

Signature :

ABSTRACT

HYPERSPECTRAL IMAGERY SUPER-RESOLUTION

Irmak, Hasan
Ph.D., Department of Electrical and Electronics Engineering
Supervisor : Prof. Dr. Gözde Bozdağı Akar
Co-Supervisor : Assist. Prof. Dr. Seniha Esen Yüksel

May 2017, 112 pages

Hyperspectral (HS) imagery consists of hundred of narrow contiguous bands extending beyond the visible spectrum. It is a three dimensional data cube with two dimensional spatial information and a spectral dimension. Despite having high spectral resolution, HS images have lower spatial resolution due to technological restrictions. This degrades the performance in HS imaging applications. Therefore, increasing the resolution is a necessity, however the problem is an ill-posed problem. In this thesis, we address this problem, namely super-resolution reconstruction (SRR) of HS images from different perspectives and propose robust solutions.

First method proposes a maximum a posteriori (MAP) based SRR technique for HS images when there is only one HS image and no other source of information. The novelty of the method is converting ill-posed SRR problem in spectral domain to a quadratic optimization problem in abundance map domain. Using smoothness prior and inherent properties of abundance maps in the quadratic optimization, a unique solution is obtained. Moreover, in order to avoid over smoothing, a post processing is applied to preserve textures in the abundance maps. Finally, high resolution (HR) HS image is reconstructed using the extracted endmembers and the enhanced abundances.

Second proposed method is a fusion based SRR method. This method enhances the spatial resolution of HS image by fusing with a coinciding HR RGB or multispectral (MS) image. Again, fusion problem is converted to a quadratic optimization problem in the abundance map domain. Moreover, proposed MAP based approach is also merged into the quadratic equation. That is, this method is a superposition of MAP based and fusion based approaches and closing the gaps of the both methods. Superposition of two methods leads to more robust and efficient SRR method. Similarly, after solving quadratic problem, HR HS image reconstructed from HR abundance maps and endmember signatures.

Experiments are implemented on real HS datasets and compared to state-of-the-art alternative methods using different quantitative image metrics. Spectral consistency, a critical issue for HS images, is also analysed in the experiments. Results demonstrate that proposed methods perform better than competitors based on quantitative metrics while keeping spectral consistency.

Keywords: Hyperspectral, Super-resolution, Maximum a Posteriori, Fusion, Quadratic Optimization

ÖZ

HİPERSPEKTRAL GÖRÜNTÜLERDE SÜPERÇÖZÜNÜRLÜK

Irmak, Hasan
Doktora, Elektrik ve Elektronik Mühendisliği Bölümü
Tez Yöneticisi : Prof. Dr. Gözde Bozdağı Akar
Ortak Tez Yöneticisi : Yrd. Doç. Dr. Seniha Esen Yüksel

Mayıs 2017 , 112 sayfa

Hiperspektral (HS) görüntü, görünür tayfın da dışına uzanan dar ve sürekli yüzlerce banttan oluşmaktadır. Bu görüntü iki adet uzamsal ve bir adet spektral boyuttan oluşan üç boyutlu bir veri küpüdür. HS görüntüler, sahip oldukları yüksek spektral çözünürlüğe rağmen, teknolojik kısıtlardan dolayı düşük uzamsal çözünürlüğe sahiptirler. Bu durum HS görüntü uygulamalarında performansı olumsuz etkilemektedir. Bu tezde farklı süper çözünürlük yapılandırma (SÇY) metotları kullanılarak HS görüntülerin uzamsal çözünürlüğünün arttırılması amaçlanmaktadır.

İlk metot sadece bir HS görüntü olduğu ve başka bir bilgi kaynağı olmadığı durumlarda MAP tabanlı SÇY tekniği önermektedir. Metodun yeniliği kötü konumlanmış SÇY problemini spektral alandan bolluk haritaları alanında ikinci dereceden bir optimizasyon problemine dönüştürmesidir. İkinci dereceden optimizasyonda düzgünlük önseli ve bolluk haritalarının özünde olan özellikler kullanılarak tek bir çözüm elde edilmiştir. Buna ek olarak, aşırı düzgünlükten kaçınmak için, görüntüdeki ayrıntıları koruyan rötuş uygulanmıştır. Son olarak, açığa çıkartılan son elemanlar ve çözünürlüğü artırılmış bolluk haritaları kullanılarak yüksek çözünürlüklü (YÇ) HS görüntü yeniden oluşturulmuştur.

İkinci önerilen yöntem kaynaştırma tabanlı bir SÇY yöntemidir. Bu metot YÇ RGB veya multispektral görüntüyü HS görüntü ile kaynaştırarak uzamsal çözünürlüğü iyileştirmektedir. Aynı şekilde kaynaştırma problemi, bolluk haritaları alanındaki ikinci dereceden bir optimizasyon problemine çevrilmiştir. Buna ek olarak, önerilen MAP tabanlı yöntem kaynaştırmadaki optimizasyon problemiyle birleştirilmiştir. Yani bu yöntem kaynaştırma ve MAP tabanlı yöntemlerin birleşiminden oluşmakta ve ikisinin de açıklarını kapatmaktadır. İki yöntemin birleşimi daha gürbüz ve etkili bir yöntem sağlamaktadır. Benzer şekilde, YÇ HS görüntü, YÇ bolluk haritalarından ve son eleman imzalarından oluşturulmaktadır.

Gerçek HS veri kümelerinde deneyler uygulanmış ve modern metotlar ile nicel görüntü metrikleri kullanılarak karşılaştırmalar yapılmıştır. HS görüntüler için kritik bir konu olan spektral tutarlılık açısından da deneyler analiz edilmiştir. Sonuçlar, önerilen yöntemlerin bahsedilen metriklere göre rakiplerine oranla, spektral tutarlığı da koruyarak, daha iyi performans sergilediği göstermiştir.

Anahtar Kelimeler: Hiperspektral, Süperçözünürlük, MAP, Kaynaştırma, İkinci Derece Optimizasyon

To my little Zeynep..

ACKNOWLEDGMENTS

First of all, I wish to express my deepest thanksgiving to my supervisor Prof. Dr. Gözde Bozdağı Akar and my co-supervisor Assist. Prof. Dr. Seniha Esen Yüksel for excellent supervision. Thank you for all of your support along the way.

I would like to thank Prof. Dr. Aydın Alatan and Prof. Dr. Yasemin Yardımcı Çetin for their valuable critics through the stages of this thesis.

I would like to express my special appreciation to my family for their continuous support and encouragements.

I would like to express my gratitude to my colleagues, my managers and ASELSAN Inc. for their understanding and concern.

I would also like to thank TÜBİTAK BİDEB for their financial support during my graduate education.

And finally for Meltem, “This thesis would never be complete without you, as everything in my life."

TABLE OF CONTENTS

LIST OF TABLES

TABLES

LIST OF FIGURES

FIGURES

LIST OF ABBREVIATIONS

ATGP	Automatic Target Generation Process
BC	Boundary Constraint
CCD	Charge Coupled Device
FCLS	Fully Constraint Least Squares
HFC	Harsanyi Farrand Chang
HR	High Resolution
HRSS	Hyperspectral Remote Sensing Scenes
HS	Hyperspectral
ICE	Iterated Constrained Endmembers
LMM	Linear Mixing Model
LR	Low Resolution
LS	Least Squares
MAP	Maximum A Posteriori
MS	Multispectral
MVT	Minimum Volume Transform
NLMM	Non Linear Mixing Model
NNLS	Non Negative Least Squares
NWHFC	Noise Whitening Harsanyi Farrand Chang
PAN	Panchromatic
PCA	Principal Component Analysis
PPI	Pixel Purity Index
QP	Quadratic Programming
RGB	Red Green Blue
SC	Smoothness Constraint
SCLS	Sum to one Constraint Least Squares
SISAL	Simplex Identification via Split Augmented Lagrangian
SPICE	Sparsity Promoting Iterated Constrained Endmembers
SRM	Superresolution Map
SRR	Superresolution Reconstruction

TV	Total Variation
UC	Unity Constraint
VCA	Vertex Component Analysis
VD	Virtual Dimensionality

CHAPTER 1

INTRODUCTION

Hyperspectral (HS) imaging is the acquisition of images in many narrow spectral bands of the electromagnetic spectrum ranging from visible, near infra-red, medium infra-red to thermal infra-red. These images are produced by instruments called imaging spectrometers, which acquire spectrally-resolved image of an object of scene. In HS imaging, the data is represented as a three dimensional data cube. Two dimensions are the spatial dimensions and the third dimension is the wavelength. As compared to multispectral (MS) imaging, HS imaging has much more information to resolve the observed scene in terms of targets or material substances. Although, targets may appear mixed with a number of materials in a single pixel, HS data analysis allows for the detection of them at sub-pixel level using spectral processing techniques. A good example to understand the difference between MS image and HS image is that MS image can be used to detect the planted areas in a town, whereas HS image can detect the wheat-planted areas in the town. Therefore, HS imaging is a powerful tool for various imaging applications such as environmental monitoring, biotechnology, medical imaging and remote sensing.

1.1 Statement of the Problem

HS sensors enable to collect a set of images across the electromagnetic spectrum. Therefore, each individual pixel can be characterized by a complete spectra in the observed spectrum as shown in Figure 1.1. The spectra of the pixels can be used to differentiate and identify materials in the scene. Therefore, HS imaging improves the capability to detect materials in the scene using spectral processing techniques.

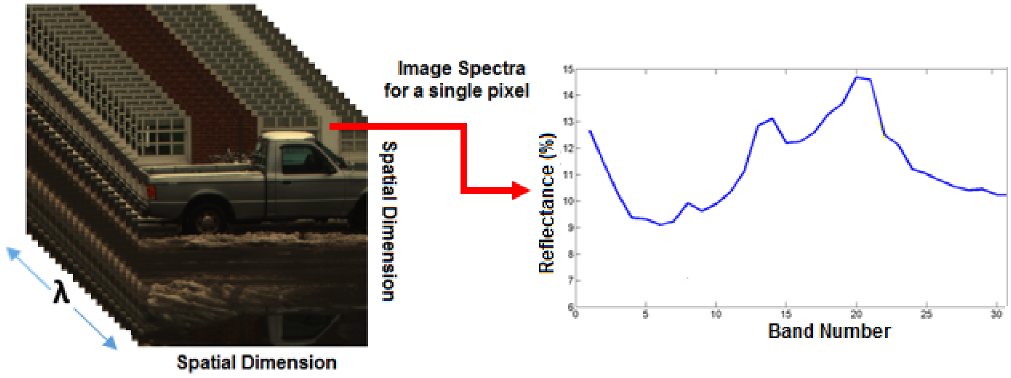

Figure 1.1: Illustration of Hyperspectral Imaging

Despite having high spectral resolution, low spatial resolution is the major limitation of HS sensors. Low spatial resolution results in mixture of different materials in a single pixel, which degrades the performance in HS image processing applications. Therefore, enhancement of the spatial resolution of HS images becomes a very promising research area in image processing. Super resolution reconstruction (SRR) is a software solution which aims to find high frequency details in the image and estimates the high resolution (HR) image using a set of low resolution (LR) images. SRR has been one of the active research areas from the first formulation of the problem [2]. It is used in many applications such as surveillance, medical imaging, face recognition to overcome the limitation of the cameras [3, 4, 5]. Therefore, SRR can be used as a post processing technique to enhance the resolution of HS images.

Many algorithms are proposed in the literature for the SRR of HS images. SRR methods for HS images can be categorized into two: single image based SRR and fusion based SRR. In the former method, SRR is more difficult and severely ill-posed. SRR of a single HS image is defined as either obtaining HR super resolution maps (SRM) showing the distributions of the materials in the sub-pixel level or HR HS image. Total variation (TV) based regularization or dictionary based learning can be used in the SRR process for single HS image SRR. On the other hand, image fusion can be used for SRR of HS images when a coinciding auxiliary HR image is available. In fusion based methods, high spatial resolution with low spectral resolution image is fused with LR HS image to enhance the spatial resolution of hyperspectral image. A review on SRR methods for both natural images and HS images is presented in detail in Chapter 3.

1.2 Contribution of the Thesis

In this thesis, SRR of HS images are investigated from different perspectives. Firstly, SRR problem is addressed using single HS image without using any other source of information. The contribution of the proposed method is converting single frame HS SRR problem to a maximum a posteriori (MAP) based quadratic optimization problem in abundance map domain. Since single image HS SRR problem is severely ill-posed, SRR problem is regularized using a Markov Random Fields (MRF) based smoothness prior. Moreover, unity constraint (UC) and boundary constraint (BC), specific constraints for the abundance maps, are used to narrow down solution space. This convex function with mentioned constraints is jointly minimized using quadratic programming (QP). In order to cope with over smoothing, a texture preserving post processing is applied to the HR abundance maps. Using these maps and spectral signatures of the materials in the scene, HR HS image is reconstructed.

Single image HS SRR is well suited for the applications when obtaining auxiliary information related to the HS image is difficult or sometimes impossible. However, performance of these type of methods are limited, especially when zoom factor is high. If any HR image is available, then it can be fused with the LR HS image to enhance the spatial resolution of HS image. Second proposed method is a HS SRR technique when another source of information (i.e. HR image) is available. In this method, not only HR image but also smoothness prior is used in the reconstruction of HR HS image. MAP based SRR has limited performance as compared to the fusion based methods, however, spectral consistency and ease of embedding prior informations are the stronger properties of MAP based solutions. On the other hand, fusion based methods have superior performance in the matching bands of the HR image whereas performance and spectrum consistency are sharply decreased in the remaining bands of the spectrum. Therefore, joint usage of these two concepts gives optimal solution for the SRR problem. In other words, MAP based fusion gives spectrally consistent, robust and high performance results for SRR of HS images.

Proposed approaches are tested on three real hyperspectral datasets and compared to two other state-of-the-art SRR methods for HS images. First method is a type of single image HS SRR and second is a fusion based SRR algorithm. The results show that proposed MAP-based algorithm produces better results as compared to its competitor. Moreover, proposed MAP based fusion method has significantly better results in selected quantitative metrics as compared with the other methods. In addition, upon observing the individual pixels for spectral consistency, the proposed methods are closest to the ground truth in all experiments.

1.3 Thesis Outline

The outline of this thesis is as follows:

Chapter 2 provides an introduction to the fundamental concepts on HS imaging. Moreover, HS unmixing methods are given in this chapter.

Chapter 3 gives a review about SRR methods for both natural and HS images.

In Chapter 4, the methodologies of the proposed methods on SRR of HS images are described in detail.

In Chapter 5, quantitative experimental results on various HS datasets with different methods are given.

Conclusions are given in Chapter 6.

CHAPTER 2

HYPERSPECTRAL IMAGING AND UNMIXING

2.1 Hyperspectral Imaging

A typical HS sensor measures the spectral radiance information emitted or reflected by the materials in hundreds of very narrow spectral bands throughout the visible, near-infra-red, and mid-infra-red portions of the electromagnetic spectrum. Atmospheric absorption by water vapor or oxygen and scattering affect the measurements [6].

In general, a HS camera has three main components; a charge-coupled device (CCD) camera, a spectrograph to measure the relative amounts of radiation at each wavelength and an optical lens. In HS imaging, first spatial dimension is obtained by scanning the scene orthogonally to the camera motion. Second spatial dimension is obtained in time while camera is moving. Moreover, each pixel has a spectral dimension. Therefore, HS image is a three dimensional data cube consisting of two spatial dimensions and a spectral dimension.

There are many advantages of HS imaging. First, since entire spectrum is sampled for each pixel, it allows to identify the materials in the scene using spectral processing techniques. Moreover, using the neighbourhood relations of the pixels among all the spectral bands, more accurate segmentations and classifications can be achieved. On the other hand, complexity is the primary disadvantage of HS data. Huge data requires both larger memories and higher processing power. Cost is another disadvantage of HS imaging. The costs of HS imaging systems are significantly higher than the MS or RGB cameras. However, with the recent airborne hyperspectral imaging systems, hyperspectral data are commercially available for research purposes.

2.2 Spectral Unmixing

Spatial resolution of a HS camera defines the size of the area on the ground for a single pixel in the HS image. Since the spatial resolution of HS cameras is low, multiple materials can occupy the same pixel. Radiance of the pixel is the combination of radiances of the materials in that pixel. These pixels are called mixed pixels. On the other hand, if a pixel is occupied by a single material then it is called pure pixel. In a HS image, both mixed and pure pixels can exist and be found using spectral unmixing approach. Spectral unmixing is the process of identifying the pure materials and finding the fractions of them in the scene. These pure materials are called endmembers and their fractions in a given pixel are called abundance maps.

Before performing spectral unmixing, a mixing model should be determined. Mixing model describes how the endmembers in a single pixel constitute the pixel spectra. There are two types of mixing models namely linear mixing model (LMM) and non-linear mixing model (NLMM)[7]. In LMM, the main assumption is that proportions of the endmembers in each pixel are well-defined with a single reflection of the illuminating radiation as shown in Figure 2.1. In other words, spectrum of each pixel in the HS image is a linear combination of the spectrum of endmembers and can be rewritten using the endmembers and their abundances linearly. On the contrary, the NLMM assumes materials are distributed randomly in the mixed pixel in a homogeneous manner. Multiple reflections exist and linear proportions does not hold for the NLMM model.

LMM is widely used instead of NLMM because LMM gives an acceptable first order approximation to the observed scene whereas NLMM is much more difficult and complicated to analyse HS image as compared to LMM [8]. Therefore, NLMM is not mentioned and spectral unmixing is applied using the LMM model. Mathematical representation of the LMM for a single pixel x is given in (2.1). The dimension of x is equal to the number of bands in the HS image.

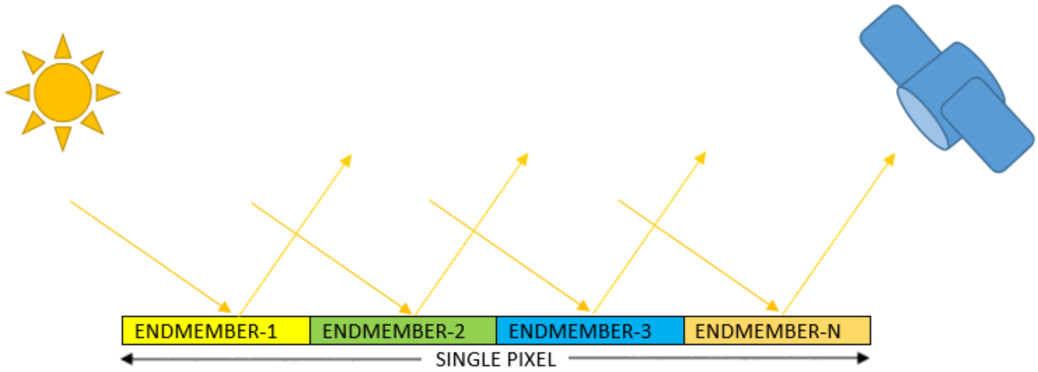

Figure 2.1: Linear Mixture Model

$$\begin{aligned} x &= a_1 s_1 + a_2 s_2 + \cdots + a_E s_E + n \\ &= \sum_{i=1}^{E} a_i s_i + n = S a_x + n \end{aligned} \tag{2.1}$$

where E is the number of endmembers, a_x is the abundance vector for pixel x with size E, S is a $p \times E$ matrix showing the spectral signatures of the endmembers, p is the number of spectral bands and n is the noise term. If matrix X is the image pixels which are organized in columns in all spectral bands, the expression can be rewritten in a compact form:

$$X = SA + G \tag{2.2}$$

In this matrix notation, A and G are the abundance matrix and noise matrix with sizes $E \times N$ and $p \times N$, respectively. N is the number of pixels in the single band HS image. Columns of the abundance matrix show the proportions of materials in the scene. The maps showing the distribution of the material are called abundance maps. The main aim of the spectral unmixing is to find these abundance maps (i.e. matrix A).

Linear unmixing consist of three main stages. First, the number of endmembers should be determined either using a priori information or unsupervised methods. After the number of endmembers are found, the spectra of the endmembers are extracted using endmember identification algorithms. Finally, abundance maps of the endmembers are estimated using the extracted endmember spectra. Each stage is explained in detail in the upcoming subsections.

2.2.1 Determination of the Number of Endmembers

A HS scene consists of a few materials (i.e. endmembers) and lack of knowledge on ground truth makes the estimation of these materials difficult. The number of endmembers can be estimated through supervised (user-selected) or unsupervised algorithms [9]. In supervised methods, the user selects the pure pixels of the different materials in the image [10]. Unsupervised methods, on the other hand, use the dimensionality of HS image as the basis for estimating the number of endmembers [11].

Virtual dimensionality (VD) is defined as the minimum number of spectrally distinct signal sources that characterize the spectral data. VD is analogous to the number of endmembers in an image. Many criteria are suggested to estimate the VD of HS image in the literature [12, 13, 14, 15].

A very popular method is principal component analysis (PCA). In PCA, an estimate for the number of endmembers is given by the number of eigenvectors which contains a user-defined percentage of image variability [16]. In other words, the number of endmembers (i.e. e) is the smallest number for which inequality in (2.3) holds. In (2.3) , λ indicates the eigenvalues of the hyperspectral data, and p shows the number of spectral bands.

$$\frac{\sum_{j=1}^{e} \lambda_j}{\sum_{i=1}^{p} \lambda_i} \geq \quad Threshold \tag{2.3}$$

A practical problem related to the PCA is the difficulty of determining $Threshold$ especially when the change between two adjacent eigenvalues is not significant [17].

PCA only utilizes the eigenvalues to find the dimensionality of the HS image. However, there can be anomalies related to the signal sources that have a little effect on the eigenvalues. Therefore, eigenvalues may not be enough to determine dimensionality.

The Harsanyi Farrand Chang (HFC) method uses a Neyman-Pearson detection theory based thresholding [18] to determine VD. Detection can be achieved using the eigenvalues of correlation and covariance matrices of related spectral band. Let (2.4) show the eigenvalues of the correlation matrix of HS image and (2.5) show the eigenvalues of the covariance matrix:

$$\lambda_{cor1} \geq \lambda_{cor2} \geq \cdots \lambda_{corL} \tag{2.4}$$

$$\lambda_{cov1} \geq \lambda_{cov2} \geq \cdots \lambda_{covL} \tag{2.5}$$

Assuming noise is white with zero mean and σ_l^2 variance for the l^{th} spectral band, if there are N distinct signal sources in HS image, then eigenvalues can be related by:

$$\lambda_{corl} \geq \lambda_{covl} \geq \sigma_l^2 \quad for \quad l = 1, ..., N \tag{2.6}$$

$$\lambda_{corl} \geq \lambda_{covl} = \sigma_l^2 \quad for \quad l = N+1, ..., L \tag{2.7}$$

In order to determine the VD, HFC method applies a binary hypotheses problem as follows:

$$H_0 : \lambda_{corl} - \lambda_{covl} = 0 \quad and \quad H_1 : \lambda_{corl} - \lambda_{covl} > 0 \tag{2.8}$$

H_0 and H_1 are the null and alternative hypotheses, respectively. On the basis of Neyman-Pearson detection theory, the number of test failures (i.e. H_0 true) is explored for all spectral bands for a given false-alarm probability, P_F. The number of failures gives the VD of the data. The VD is completely determined by P_F.

In HFC method, noise is assumed to be zero mean white Gaussian. However, there are cases in which this assumption does not hold. Noise Whitening HFC (NWHFC) is a modified version of HFC to solve that problem and enhance signal detection performance. NWHFC has a preprocessing noise whitening step to remove the second order statistical correlation [17]. In this case, noise estimation is required for the NWHFC method.

Hyperspectral signal subspace identification by minimum error (HySime) is another approach to determine the number of endmembers by estimating the signal and noise correlation matrices [19]. In HySime, a signal subspace is represented using a certain amount of eigenvectors of the signal correlation matrix. The dimension of the subspace is checked by comparing the sum of the projection error power with noise power. If the latter is dominant, then the subspace dimension is overestimated. However, if the projection error power is dominant, then subspace dimension is underestimated.

2.2.2 Endmember Selection

Endmember selection is the hardest part of the spectral unmixing problem [7]. For a better subpixel composition, the determination of the endmembers in the image should be performed accurately. Early approaches of endmember determination is based on the laboratory analysis of the part of the terrain. The prior knowledge about the contents of the part of the image terrain is used for the whole endmembers in the image [9]. However, this approach is not feasible when trying to analyze large quantities of data. Therefore, for the last two decades efficient unsupervised endmember selection methods have been developed in the literature and majority of them rely on the convex geometry model based on the expression in (2.1)[11, 6].

Extraction algorithms can be divided into two groups: with or without the assumption that pure pixels are present in the image for each endmember.

Pixel Purity Index (PPI) is a popular technique widely used in endmember extraction [20]. It uses orthogonal projection to determine the endmembers in the image. The main idea of the PPI is that the orthogonal projection of an endmember to a vector in a p-dimensional spectral space is either minimum or maximum. Using this idea, PPI algorithm is developed. In PPI, first, random unit vectors are generated in p-dimensional space which are called skewers. Then, all the data pixels are projected onto these skewers and the maximal and minimal projections are selected as extreme pixels which are potential endmembers for each skewer. In Figure 2.2, the skewers and extreme pixels are shown clearly. Finally, the endmembers are selected from these extreme pixels using a voting procedure. In other words, the endmembers are the extreme pixels which are more frequently selected in projections on skewers than other extreme pixels.

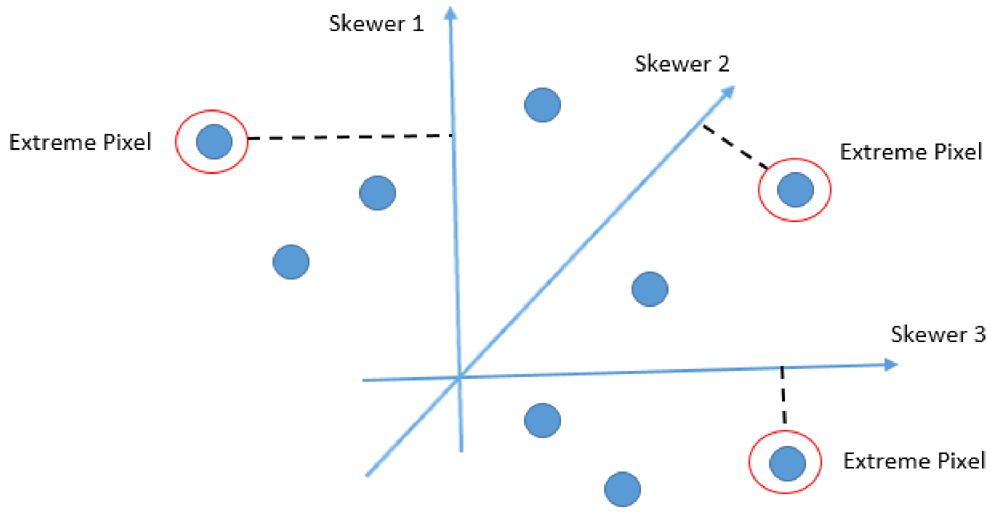

Figure 2.2: Illustration of PPI

One of the major issues in PPI is determining the number of skewers and endmembers in the algorithm. These parameters directly affect the PPI performance and there is no criteria how to select appropriate values of these two parameters [21].

The Automatic Target Generation Process (ATGP) was proposed by [22]. The basic idea is to search most distinctive pixels whose projections in the orthogonal subspace of other pixels are the most dissimilar. First, an initial signature is selected which is the brightest pixel in the image. Then, iteratively other endmembers which have the maximum orthogonal projection to the existing endmembers are extracted. The iteration stops when the desired number of endmembers are estimated.

Minimum Volume Transform (MVT) is a non-orthogonal linear transformation that transforms the data to set of new coordinates. Since every pixel is a linear combination of the materials (pure spectral signatures) in LMM, pixel scatter diagram should be a simplex. Moreover, the vertices of the simplex is the sought endmembers in the image. In MVT, the minimal volume data simplex will be found in the image which gives the set of endmembers. On the contrary, maximum simplex volume based algorithms also exist. N-FINDR and Vertex Component Analysis (VCA) are two examples of automated approaches that find the set of pixels which define the simplex with the maximum volume [23, 24]. The idea is that for p spectral bands, p-dimensional simplex volume formed by pure pixels is the largest volume. To exemplify, scatter plot of three endmembers and two spectral bands is shown in Figure 2.3. The volume of the red triangle is larger than any other volume defined by any other combination of pixels.

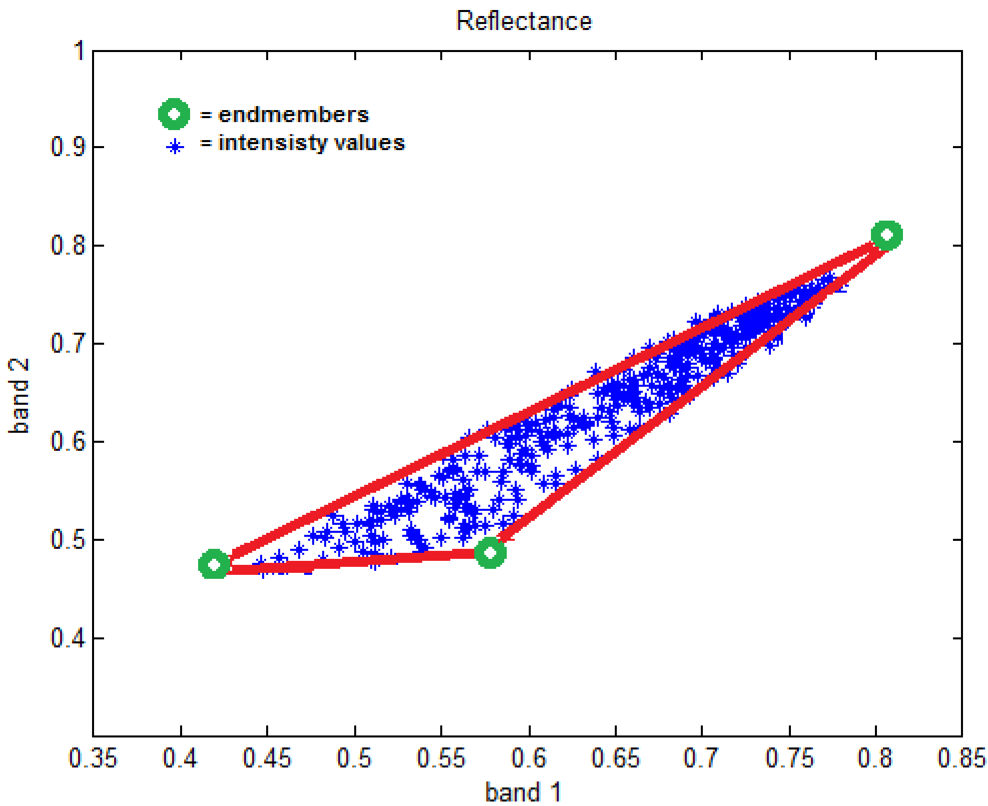

Figure 2.3: Illustration scatterplot and maximum volume simplex

N-FINDR is a selection algorithm that starts with a random selection of pixels as candidate endmembers[23]. In each iteration, remaining image pixels are replaced with candidate if volume of the simplex increases. The process is exhausted when no replacement increases the volume. The vertices show the endmembers in the hyperspectral data.

VCA is another algorithm that searches the maximum volume simplex [24]. It uses two facts. First, if pure endmembers in the scene exist then they should be the vertices of a simplex. Secondly, the affine transformation of a simplex is also a simplex.

The algorithm iteratively projects data onto a direction orthogonal to the subspace spanned by the endmembers, which are already determined. The new endmember signature corresponds to the extreme of the projection. The algorithm iterates until all endmembers are exhausted.

In [24], VCA is compared with PPI and N-FINDR. The conclusion is that VCA performs better than PPI and has a closer performance to N-FINDR. However, the main contribution of VCA is the computational complexity. VCA is between one and two orders of magnitude faster than N-FINDR and PPI.

PPI, ATGP, MVT, VCA and N-FINDR are the algorithms that assume at least one pure pixel exists in the image for each endmember. However, hyperspectral data generally dominated by mixed pixels and some of the endmembers has not pure pixel in the image. Therefore, using an algorithm without pure pixel assumption is more suitable in many applications. However, unmixing without pure pixel assumption is more challenging as compared to the pure pixel assumption based algorithms. There are number of studies that extract the endmembers without pure pixel assumption.

The simplex identification via split augmented Lagrangian (SISAL) algorithm is used to unmix hyperspectral data in which the pure pixel assumption is violated [25]. In SISAL, the abundance matrix (A) and spectral signature matrix (S) given in (2.9) fit a minimum volume simplex to the data subject to non-negativity and sum to one constraints. The volume defined by columns of A is proportional to its determinant. Therefore, finding the minimum point of the determinant of A subject to the constraints gives endmembers in the HS image as given in (2.10).

$$X = SA \tag{2.9}$$

$$\widehat{A} = arg\, min_A |det(A)| \qquad subject\ to \quad A^{-1}X \geq 0 \quad and \quad 1_p^T A^{-1} X = 1_N^T \tag{2.10}$$

Where N shows the number of pixels, p is the number of spectral bands, 1_N and 1_p are the N and p dimensional column vector of all 1s. Using (2.11), (2.12) and (2.13), the problem simplifies to (2.14).

$$Q = A^{-1} \tag{2.11}$$

$$det(Q) = \frac{1}{det(A)} \tag{2.12}$$

$$a^T \equiv X^T(XX^T)^{-1} \tag{2.13}$$

$$\widehat{Q} = arg\, min_Q - log|det(Q)| \qquad subject\ to \quad QX \geq 0 \quad and \quad 1_p^T Q = a^T \tag{2.14}$$

Non-negativity constraints can be replaced by a soft constraint whose strength is controlled by a regularization parameter. The following modified version is obtained:

$$\widehat{Q} = arg\, min_M - log|det(Q)| + \lambda \|QX\|_h \qquad subject\ to \quad 1_p^T Q = a^T \tag{2.15}$$

where,

$$\|X\|_h \equiv \sum_{ij} h([X]_{ij}) \tag{2.16}$$

$$h(x) \equiv max(-x, 0) \tag{2.17}$$

The function $h(x)$ is the hinge function and penalizes the negative solutions. Using non-negativity as a regularizer yields solutions that are robust to outliers, noise, and poor initialization. The amount of regularization is controlled by a positive regularization parameter λ. Finally, minimization problem given in (2.15) is solved by a sequence of variable splitting augmented Lagrangian optimizations to find the endmembers in the HS image.

Iterated Constrained Endmembers (ICE) is a statistical approach to identify the endmembers without pure pixel assumption [26]. It suggests a least squares (LS) minimization based on LMM. The expression that needs to be minimized is called the residual sum of squares (RSS) given in (2.18):

$$RSS = \sum_{i=1}^{N} (X_i - \sum_{k=1}^{E} p_{ik} E_k)^T (X_i - \sum_{k=1}^{E} p_{ik} E_k) \tag{2.18}$$

where X_i is the i^{th} pixel value, E is the number of endmembers, p_{ik} is the proportion of k^{th} endmember for i^{th} pixel and N is the number of pixels in the image. It can be shown that minimizer for (2.18) is not unique. Therefore, it needs to be constrained by additional terms to RSS. In ICE, sum of squared distances (SSD) between endmembers is used to constrain the solution space. SSD is given in (2.19).

$$RSS = \sum_{i=1}^{N} (X_i - \sum_{k=1}^{E} p_{ik} E_k)^T (X_i - \sum_{k=1}^{E} p_{ik} E_k) \tag{2.19}$$

It is also shown that SSD is equivalent to (2.20):

$$SSD = E(E-1)V \tag{2.20}$$

where V is the sum of variances (over the bands) of the simplex vertices.

Using RSS and SSD, the objective function called regularized RSS (R_{reg}) that needs to be minimized is given in (2.21):

$$RSS_{reg} = (1-\mu)\frac{RSS}{N} + \mu V \tag{2.21}$$

where μ is the regularization parameter.

An extension of ICE algorithm that incorporates sparsity-promoting priors to find the correct number of endmembers is sparsity-promoting ICE (SPICE) [27]. SPICE has an automated mechanism to determine the correct number of endmembers. In order to do so, SPICE algorithm adds a sparsity-promoting term (SPT) to the regularized RSS. The form of SPT term is given in (2.22):

$$SPT = \sum_{k=1}^{E} \frac{\Gamma}{\sum_{i=1}^{N} \rho_{ik}} \sum_{i=1}^{N} \rho_{ik} \tag{2.22}$$

where Γ is a constant. The advantage of ρ_k is that if a proportion of a particular endmember becomes small, then ρ_k for that endmember becomes larger. This weight change accelerates the minimization. In order to minimize the objective function of SPICE, the iterative minimization can be used as in ICE.

ICE and SPICE may not generate physically possible endmember spectra. To solve this problem an extension of SPICE (SPICEE) can be used to estimate the endmembers having values between zero and unity [28]. In [28], instead of taking pseudo-inverse as in SPICE, a quadratic optimization is applied with the boundary constraint to estimate the endmembers and physically meaningful results are obtained.

Minimum volume constrained nonnegative matrix factorization (MVC-NMF) is another unsupervised endmember extraction algorithm from highly mixed hyperspectral data [29]. MVC-NMF algorithm combines minimum approximation error with the minimum simplex volume determined by the estimated endmembers. This is achieved by solving the optimization problem given in (2.23).

$$\begin{aligned} &minimize \quad f(A,S) = \frac{1}{2}\|X - AS\|_2^2 + \lambda J(A) \\ &subject\ to \quad A \geq 0, \quad S \geq 0 \quad and \quad 1_C^T S = 1_N^T \end{aligned} \tag{2.23}$$

where 1_C and 1_N are the C and N dimensional column vector of all 1s and $J(A)$ is the regularizer. It forces the simplex volume to be small. Using the volume constraint as a regularizer makes the algorithm more robust to the noisy pixels, since the simplex can be made without including all the data points. Compared to ICE or SPICE, instead of solving a quadratic optimization problem, in MVC-NMF algorithm, the minimization is treated as a LS problem and solved iteratively in an analytical way.

SPICE and MVC-MNF algorithms give not only spectral signatures of endmembers but also their abundances. Therefore, there is no need to use any abundance estimation method. However, for the other endmember extraction algorithms, the abundances should be estimated.

2.2.3 Abundance Estimation

Estimation of abundances is the final output of linear unmixing. This step aims to find the fractions of the determined endmembers. In other words, it gives the percentage of the materials in each pixel. Using this information, sub-pixel analysis can be made in the HS image. In the previous section, the endmembers are extracted and spectral signature matrix S is obtained. By knowing the S matrix, abundance map matrix A in equation (2.2) can be found using LS analysis. The LS solution is given in (2.24):

$$A_{LS} = (S^T S)^{-1} S^T X \tag{2.24}$$

Equation 2.2 is valid when the system is overdetermined. In other words, LS solution exists when number of bands is greater than the number of endmembers in the image. This is a reasonable assumption since spectral bands are generally much greater than the number of endmembers for HS image. The main drawback of LS solution is that LS estimate have no physical constraints related to the abundance maps. LS solution is a mathematical point of view to the abundance estimate which can converge a solution which is unrealizable (e.g. negative fractions). The only advantage of LS solution is being a quick way to extract the abundance maps from the image.

Since LS solution has no physical restrictions onto abundance maps, some constraints can be added to the LS solution in order to obtain physically meaningful solutions. Abundance maps are imposed to two constraints namely non negativity constraint and sum to one constraint. These constraints state that abundances of the endmembers are non-negative and sum of abundances of a single pixel is unity. Considering the former constraint, a non-negative abundance restriction should be added to the equation in order to get more accurate results. In other words, the elements of matrix A should be non-negative. LS solution with this constraint is called Non Negative Least Square (NNLS) solution. The NNLS problem is given in 2.25.

$$A_{NNLS} = (S^T S)^{-1} S^T X \quad subject \quad to \quad a_i \geq 0, \quad i = 1, ..., E \tag{2.25}$$

In [30], abundance maps are estimated by enforcing the abundances of each pixel to sum one. LS solution including the sum to one constraint is called sum to one constraint LS (SCLS) and the formulation is given in 2.26.

$$A_{SCLS} = (S^T S)^{-1} S^T X \quad subject \quad to \quad \sum_{i=1}^{E} a_i = 1 \tag{2.26}$$

NNLS and SCLS solutions are more accurate then the LS solution and they are simple to implement. However, there are still problems with resulting abundances. NNLS solution could violate the sum to one constraint and SCLS solution could have negative abundances. Therefore, these two constraints should restrict the solution space together. This solution is called Fully Constrained Least Squares (FCLS) solution which has both non-negativity and sum to one constraints. The formulation of the FCLS is given in 2.27.

$$A_{FCLS} = (S^T S)^{-1} S^T X \quad subject \quad to \quad a_i \geq 0, \quad i = 1, ..., E \quad and \quad \sum_{i=1}^{E} a_i = 1 \tag{2.27}$$

The main drawback of FCLS solution is the higher computational complexity. However, it gives the most accurate and reliable way of the abundance map estimation [30].

CHAPTER 3

SUPERRESOLUTION RECONSTRUCTION

Spatial resolution of an image is determined by the imaging sensor. Sensor size and optics of the camera limit the spatial resolution of the image. The cost of reducing sensor size and manufacturing high precision optical devices are not practical in real life applications. Therefore, using image processing techniques to increase the resolution of images is an essential research area. In image processing, SRR refers to obtaining HR image from set of LR images and single image enhancement is often referred as image interpolation. However, in recent years, both methods are called SRR [31]. In the literature, there are substantial amount of studies related to SRR for RGB and MS images in the last two decades. In recent years, with the recent advances in HS imaging systems and the ease of access to the HS data, great efforts have also been made to the SRR of HS images.

3.1 Observation Model and SRR Problem

The goal of multi-frame SRR is to reconstruct a HR image from a set of LR images. The first step to examine the SRR problem, except learning based methods, is to define an image observation model which relates the HR image with the LR images. Optical blur, motion of sensor and aliasing effects should be in the observation model. A typical observation model for an imaging system is shown in Figure 3.1.

In this observation model, firstly band limited continuous scene is sampled above the Nyquist rate and discrete HR image is obtained. Then, multiple HR images are formed because of camera motion. These HR images are affected by sensor and optical blur. Blurred observations are sub-sampled with aliasing. Finally, these observa-

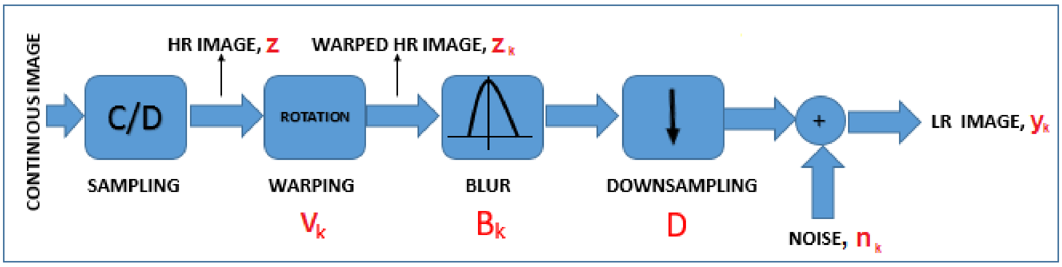

Figure 3.1: Observation model for Multi-frame SRR

tions are corrupted by additive noise and LR images are formed. In other words, the observed LR images result from warping, blurring, and down-sampling operations performed on the HR image. The mathematical representation of the observation model is given in (3.1).

$$y_k = DB_kV_kz + n_k \tag{3.1}$$

In (3.1), z is the HR image and y_k is the k^{th} LR image. z and y_k are used in lexicographical representation in which the rows of are concatenated to form a column vector. In this way, y_k is an MN size vector and z is a vector of size l_1Ml_2N, where LR single band image size is $M \times N$, l_1 and l_2 are down sampling factors in vertical and horizontal directions respectively. D is an $MN \times l_1Ml_2N$ matrix representing the down sampling operation, B and V are the $l_1Ml_2N \times l_1Ml_2N$ matrices representing the blurring and warping, respectively and n_k is additive noise vector of size MN.

Equation (3.1) can be rearranged to cover all the LR images into a single linear equation as given in (3.2) or equivalently in (3.3).

$$\begin{bmatrix} y_1 \\ y_2 \\ \vdots \\ y_K \end{bmatrix} = \begin{bmatrix} DB_1V_1 \\ DB_2V_2 \\ \vdots \\ DB_KV_K \end{bmatrix} z + \begin{bmatrix} n_1 \\ n_2 \\ \vdots \\ n_K \end{bmatrix} \tag{3.2}$$

$$y = Wz + n \tag{3.3}$$

In (3.3), decimation, blur and motion matrices are very sparse which makes the in-

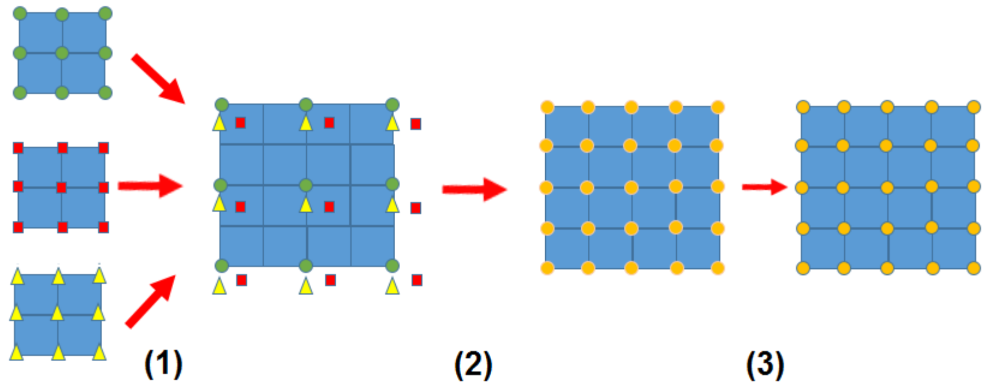

Figure 3.2: Super-resolution Concept

verse problem severely ill-posed. Equation (3.3) can be made overdetermined using more LR images having different sub-pixel shifts. If these shifts are known or estimated within sub-pixel accuracy, then multi-frame SRR is possible.

Initial study of SRR started with [2] in frequency domain. Their solution based on shifting and aliasing properties of Continuous and Discrete Fourier Transform (CFT and DFT). However, frequency domain SRR theory did not go beyond and later works have been almost in spatial domain [32].

Figure 3.2 shows a simplified diagram of the multi-frame SRR in the spatial domain. First, LR image pixels are registered on HR image grid using image registration algorithms [33, 34]. Secondly, unknown pixels are found using restoration methods [35, 36]. Finally, non-uniform interpolated image deblurred and removed from noise to obtaining the HR image.

SRR problem is more challenging when there is only one LR image. The goal of single image SRR methods is to generate HR image from a single LR image. Since there is no motion in single image, the observation model is simplified to Figure 3.3. This observation model can also be used for SRR of HS images.

3.2 SRR Methods

In HS imaging, SRR can be obtained either using single image or using an auxiliary HR image for fusion. Therefore, single image SRR methods can also be used for SRR

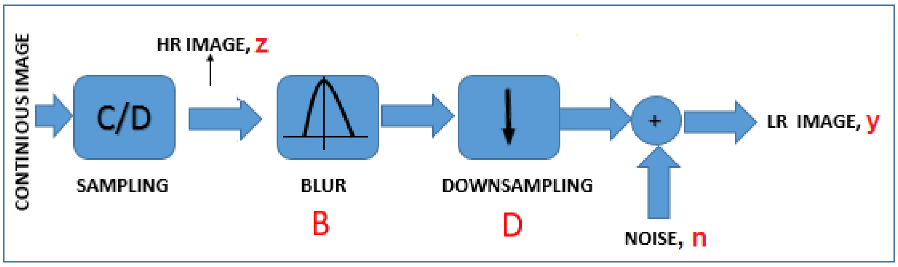

Figure 3.3: Observation model for Single Image SRR

of HS images. In this section, SRR methods are introduced assuming K different LR images exist, however, they can be easily adapted for the single LR image (i.e. $K = 1$).

3.2.1 Bayesian Methods

Bayesian approaches insert probabilistic information to the SRR problem. In this approach, a Bayesian framework is established using HR image and noise probability density functions (pdfs) to estimate the HR image [37]. Since the SRR problem is ill-posed and there is no unique solution, HR image pdf regularizes the solution and narrows down the solution space.

Let z is HR image and y_k is the k^{th} LR image generated from z. Essentially, the most probable estimate of z given set of K LR images is:

$$\widehat{Z} = argmax_z Pr(z|y_1, y_2, ..., y_K) \tag{3.4}$$

Equation in (3.4) is the maximum a posteriori (MAP) solution which maximizes a posteriori pdf with respect to z. Bayes' law converts prior information about the HR image into a posterior probability. According to Bayes' law, (3.4) is equivalent to:

$$Pr(z|y_1, y_2, ..., y_K) = \frac{Pr(y_1, y_2, ..., y_K|z)Pr(z)}{Pr(y_1, y_2, ..., y_K)} \tag{3.5}$$

Thus, using Bayes' law, the maximum a-posteriori (MAP) estimate of z is defined as:

$$\widehat{z}_{MAP} = argmax_z(Pr(y_1, y_2, ..., y_K|z)Pr(z)) \tag{3.6}$$

$Pr(y_1, y_2, ..., y_K)$ has no effect on maximization; thus, it is not included in the estimate in (3.6).

Taking the logarithm of (3.6), the MAP estimate becomes:

$$\widehat{z}_{MAP} = argmax_z(ln[Pr(y_1, y_2, ..., y_K|Z)] + ln[Pr(z)]) \tag{3.7}$$

In (3.7), $ln[Pr(y_1, y_2, ..., y_K|z)]$ is the data log-likelihood term and $ln[Pr(z)]$ is the prior information related to the HR image. MAP estimation gives regularized solutions for the SRR problem using this prior knowledge about HR image. Bayesian approaches vary according to the assumption about prior knowledge. If there is no information about the HR image, pdf of HR image can be considered as uniformly distributed. In this case, SRR problem is reduced and called as the Maximum Likelihood (ML) solution given in (3.8) for the independent LR observations.

$$\widehat{z}_{ML} = argmax_z ln[Pr(y_1|z)] + ln[Pr(y_2|z)] + ... + ln[Pr(y_K|z)]] \tag{3.8}$$

Using the equation of the obervation model in (3.1) with assuming Gaussian noise with $N(0, \sigma^2)$ as given in (3.9), (3.9) is obtained for the conditional probabilities.

$$Pr(n) = \frac{1}{(2\pi r)^{N/2}} e^{\frac{-n^T n}{2\sigma^2}} \tag{3.9}$$

$$Pr(y_k \mid z) = \frac{1}{(2\pi r)^{N/2}} e^{\frac{-(y_k - DB_kV_kz)^T(y_k - DB_kV_kz)}{2\sigma^2}} \tag{3.10}$$

Using (3.8) with (3.10), ML estimation becomes:

$$\widehat{z}_{ML} = argmin_z(\sum_{k=1}^{K} \frac{1}{2\sigma^2}(y_k - DB_kV_kz)^T(y_k - DB_kV_kz) + ln(\frac{K}{(2\pi r)^{N/2}})) \tag{3.11}$$

The terms which has no effect on the minimization can be removed from (3.11) and ML solution is reduced to:

$$\widehat{z}_{ML} = argmin_z(\sum_{k=1}^{K} \|y_k - DB_kV_kz\|^2) \tag{3.12}$$

ML solution relies on the observations and seeks the most likely solution. However, ML solution is ill-posed when the number of LR observations are limited and zoom factor is large. Therefore, ML solution requires a regularization term to find the solution in a stable manner. MAP estimation regularizes the solution using the image priors and different kinds of priors are suggested in the literature [38, 39, 40].

Markov Random Field (MRF) model is a common image prior model which assumes that there is a statistical correlation between neighbouring pixels [41]. In other words, the configuration of a pixel is given the configuration of the rest of the image is same as the configuration of a pixel given the configuration of the neighbouring pixels. Therefore, MRF models neighbouring relations of the pixels in the image. Gaussian MRF (GMRF) [42] is a widely used MRF prior. Despite the simplicity of GMRF, over smoothing is the main disadvantage of GMRFs. In order to preserve edges, more complex priors such as Huber MRF (HMRF) are suggested in the literature [38]. HMRFs preserve the edges while keeping the smoothness in the image. In [1], another approach is proposed for edge preserving. In this study, two SRR with different regularization parameters (λ_1, λ_2) are used. First regularization parameter is very close to zero (i.e. $\lambda_1 \approx 0$) and it creates a noisy estimate of the image with preserving textures. It is called as the MAP_1 estimate. However, second regularization parameter is much greater than the first one ($\lambda_1 \ll \lambda_2$) and creates an over-smoothed SRR estimate. Similarly, it is called as the MAP_2 estimate. The pixel difference of first estimate and second estimate gives the high frequency (HF) image composed of edges and textures. After HF image is extracted, Gabor Filter is applied to the HF Image to detect textures. Finally, textures and MAP_2 estimate are combined to obtain a texture preserved MAP estimate. This method can be easily integrated to MAP solutions as a post-processing technique for texture preserving. The block diagram of the method is given in Figure 3.4.

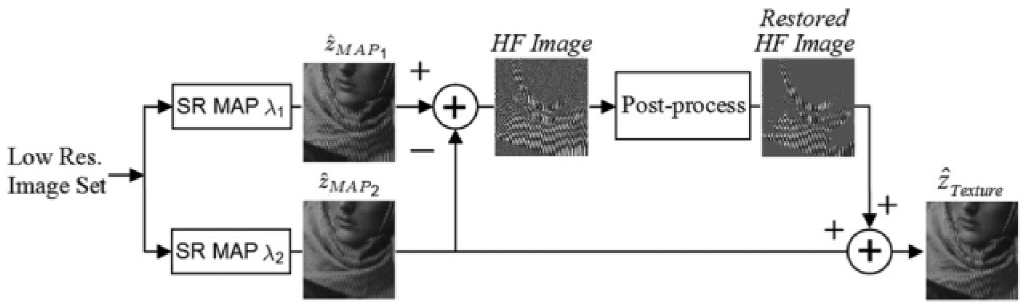

Figure 3.4: Texture preserving SRR method, Adapted from [1]

3.2.2 Iterative Back Projection Method

Iterative Back Projection (IBP) method for SRR is formulated in [43] which is adapted from back projection used in tomography. IBP is an iterative process, in each iteration new HR image is estimated by back projecting the difference between the simulated LR image and real LR image. Simulated LR image is obtained using the observation model and estimated HR image in the previous iteration using the expression in (3.13).The iterative process is repeated to minimize the error as given in (3.14).

$$\widehat{y}_k^n(m_1, m_2) = W_k(m_1, m_2; n_1, n_2) \cdot \widehat{z}^n(n_1, n_2) \tag{3.13}$$

$$\widehat{z}^{n+1}(n_1, n_2) = \widehat{z}^n(n_1, n_2) + \sum_{m_1, m_2} H_{BP}(m_1, m_2; n_1, n_2)[y(m_1, m_2) - \widehat{y}_k^n(m_1, m_2)] \tag{3.14}$$

In (3.14), H_{BP} is the projection kernel and various kernels can be used for regularizing the process and they affect the characteristics of the solution [43]. In the literature, there are improved methods based on IBP. In [44], IBP extended to consider multiple motion models. In [45], IBP method combined with the Canny edge detection to recover high frequency information. The method is much faster and more robust to noise. Simplicity and lower complexity are the advantages of IBP. However, the solution space of IBP is not unique and adding prior constraints is hard to apply. Moreover, choosing correct projection kernel is generally difficult [46].

3.2.3 Projection onto Convex Sets Method

Projection Onto Convex Sets (POCS) method is first formulated in [47] for SRR. It is an iterative method using a priori information of HR image as constraints. Each constraint is a convex set for the solution space. LR images, smoothness etc. can be a constraint. Solution of SRR is the intersection of these convex sets. The intersection is found using (3.15):

$$z^{n+1} = P_i P_{i-1} ... P_2 P_1 z^n \tag{3.15}$$

Where P_i is the projection operator of the convex set C_i for the i^{th} constraint and z^n shows the HR image at the n^{th} iteration.

Different constraints can be used in POCS method. The basic constraint is the data constraint and can be modelled as [48]:

$$C_D = \{z[n_1, n_2] : y[m_1, m_2] = \sum_{n_1, n_2} W_k[m_1, m_2; n_1, n_2] z[n_1, n_2]\} \tag{3.16}$$

Where $W_k[m_1, m_2; n_1, n_2]$ is the weight matrix determined by the observation model.

Smoothness [49] and amplitude [48] constraints are the other common constraints given in (3.17) and (3.18) respectively.

$$C_S = \{z : \|S_z(n_1, n_2) \leq Threshold\|\} \tag{3.17}$$

$$C_A = \{z(n_1, n_2) : a \leq z(n_1, n_2) \leq b\} \tag{3.18}$$

In (3.17), S_z shows the high pass filtered version of z.

After defining convex sets, the optimal solution (i.e. HR image) lies in the intersection of these convex sets.

3.2.4 Learning Based Methods

In general, learning based methods aim to find the HR image from a single LR image with the help of a pre-trained database. Database stores the HR patches of the corresponding LR patches. For each LR patch in the LR image, first, the most similar LR patch in the database is found, then the corresponding HR patch is used to increase the resolution. There are also studies that store mid-frequency and high frequency image patches in the database obtained from training LR and HR images [50, 51, 52]. Since the functional mapping of LR patch to HR patch is ill-posed, the performance strictly depends on the selection of the corresponding HR patch of the LR patch. In other words, for a single LR patch, there can be more matching than a single HR patch. Different matching metrics can be used to select the HR patch [53, 52]. False mapping leads to unwanted outliers or blurring in the superresolved images. Therefore, additional constraints should be added to eliminate the possible selection of wrong HR patches in the database. One simple way of that is using overlapping patches in the image, and applying smoothness constraint in the decision of the correct HR patch [54].

In learning based methods, patch size is a critical parameter on the performance of the method. Small patch sizes result in wrong estimation of HR patch whereas higher patch sizes make the training set enormous. Moreover, performance strictly depends on the correlation of the training dataset and the LR input image.

3.3 SRR Methods for HS Images

Adapting SRR methods to HS images becomes one of the active research area in image processing. However, there is a conceptual difference in SRR for HS images. In RGB or MS images, a general SRR problem is to reconstruct HR image given a set of LR images. On the contrary, it is hard to find real HS images which have sub-pixel shifts between them. Although there are few studies in SRR for HS images using sub-pixel shifts across bands [55, 56], they are either synthetically generated from the original HS images or using Chris/Proba images, taken from different angles. [57]. Therefore, these type of methods are not included in this study and SRR methods for HS is categorized in two, namely single image based and fusion based. In single image SRR, main aim is either to increase the spatial resolution of landcovers to provide more accurate representation of land covers or spatially enhanced HS image as compared to original image [58]. Second method is the fusion based reconstructing HR HS image by combining LR HS image with a high spatial resolution auxiliary image.

3.3.1 Single Image SRR

SRR problem is more challenging when the observed data is single frame in which there is only one LR HS image and not any other source of data. Since LR HS image has fewer measurements than the number of unknown pixels in the HR image, SRR problem is severely ill-posed. In general, SRR methods using auxiliary data such as sub-pixel shifted LR images or HR RGB or MS image generates better results [58]. However, single image SRR for HS images are taking considerable attention since sometimes supplementary data may not exist for the HS image. The output of single SRR can be either super-resolution maps (SRM) [59, 60, 61], a map to describe the most likely distribution of mixed pixels, or HR HS image [58, 62, 63].

Single SRR problem can be divided into two groups. In the first category, original HS image is transformed to a finer resolution by dividing pixels to sub-pixels and assigning pixel values according to prior assumptions (spatial correlation, low rank, etc.). This is the regularization based method. In addition, learning based method is the other category using the pre-trained dictionaries in the resolution enhancement process.

3.3.1.1 Spatial Optimization Based Methods

Spatial correlation of the endmembers is a widely used prior in the literature [64, 59]. According to the desired zoom factor, each endmember is initially assigned a pixel according to the fractional abundances. In the SRR step, a spatial regularization is applied to find the final positions of the endmembers using the tendency of spatial correlation of endmembers. A typical example of neighbouring relation is given in

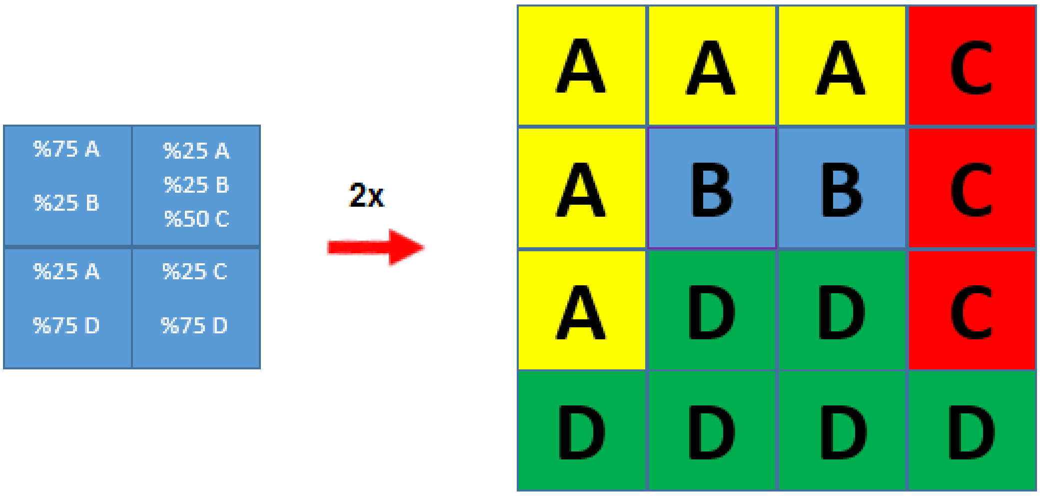

Figure 3.5: Neighbouring relation of endmembers

Figure 3.5 for four endmembers and 2x2 LR image is interpolated to 4x4 HR image. In this example, locations of the materials in the interpolated image are assigned according to the fractions of the materials in corresponding LR pixel and its neighbours. Different techniques are developed for SRR based on the spatial optimization.

In [59], the endmember pixels are repositioned to minimize the perimeter of the area belonging the same endmember. Simulated annealing is used in the minimization procedure. In [65], a similar approach is applied without using any minimization method, each sub-pixel is assigned according to the highest contribution endmember in the neighbouring pixel. This process is repeated for all of the sub-pixels within all the pixels and HR classification maps are obtained.

In [60], spatial regularization is achieved by a modified version of binary particle swarm optimization (BPSO). To do so, first, abundance maps are found using unmixing and pure pixels are determined via applying a threshold to abundances. Then for the remaining pixels, endmembers are assigned for each sub-pixel according to its fraction. Finally, spatial distributions are found using modified BPSO.

In [61], an adaptive sub-pixel mapping algorithm is proposed. After finding the abundance maps, each pixel is divided along columns into smaller units and fractions are duplicated in the divided pixels. Fractions of these pixels are re-predicted according to the neighbour pixels. The pixel division is repeated for the rows of the image and fractions are recalculated. The output of the method is a land cover map with higher spatial resolution than the original HS image.

In [58], a joint spectral-spatial sub-pixel mapping is proposed. Integrating the sub-pixel mapping model with linear mixture model, a joint sub-pixel model is obtained with sum-to-one and non-negativity constraints as given in (3.19).

$$Y = BZ_{prob}D + N \quad s.t. \quad Z_{prob} \geq 0 \quad 1_p^T Z_{prob} = 1_{ns}^T \tag{3.19}$$

Where B and D show the blur and down-sampling operators. Y is the LR HS image and Z_{prob} is sub-pixel probability map of HR HS image. In order to regularize the solution the isotropic total variation (TV) model is used which is represented as:

$$TV(Z_{prob}) = \sqrt{|\nabla_x Z_{prob}|^2 + |\nabla_y Z_{prob}|^2} \tag{3.20}$$

Where ∇_x and ∇_y are the first order differences operators. Finally, the expression given in (3.21) is minimized using the gradient descent algorithm to obtain the optimal sub-pixel probability map Z_{prob}. HR HS image is generated using Z_{prob} and spectral signature matrix.

$$\widehat{Z}_{prob} = argmin_{Z_{prob}}(\|Y - MZ_{prob}D\|_2^2 + \|1_p^T Z_{prob} - 1_{ns}^T\|_2^2 + \lambda TV(Z_{prob}) \tag{3.21}$$

In [62], SRR is achieved regularizing the ill-posed data fidelity term via minimizing l_2 norm of the gradient summed over all pixels and all bands. Moreover, two models are proposed with different additional regularization using the spectral unmixing information. In the first model, endmember based TV model, additional regularization is a soft constraint and penalizes the mixed pixels producing HR HS images. Second model, quantum TV, forces the mixed pixels to be pure producing HR classification maps.

In [63], 3D TV (3DTV) regularization and low rank are combined for regularization of the ill-posed data term. In TV, local spatial consistency is preserved as in (3.20) whereas in 3DTV a local spatial-spectral consistency is considered. 3D TV is expressed in (3.22). Observation model consists of blurring and downsampling operators with observation noise and the regularization model is given in (3.23). Model is minimized using the alternating direction method of multipliers (ADMM) [66].

$$3DTV(Z) = \sum_{ijk} |Z_{ijk} - Z_{ij,k-1}| + |Z_{ijk} - Z_{i,j-1,k}| + |Z_{ijk} - Z_{i-1,j,k}| \tag{3.22}$$

$$\widehat{Z} = argmin_Z \|DBZ - Y\|_2^2 + \lambda_1 3DTV(Z) + \lambda_2 Rank(Z) \tag{3.23}$$

Where D and B are the down-sampling and blurring matrices, respectively. $Rank()$ is the rank function penalizing the higher rank matrices.

In [67], using abundance maps, a joint energy function is constructed using different regularizers for the SRR of HS images. Smoothness, edge preserving and sum-to-one constraints are used together to regularize the ill-posed data constraint. Moreover, graph cut expansion algorithm is used to minimize the energy function. Finally, using HR abundances, HR HS image is reconstructed. A similar concept is introduced in [68], in this work, smoothness and sum-to-one property of abundances are used for regularization. However, gradient descent is used for the energy minimization which is a time efficient way of minimization. The main problem related to energy minimization problems is the difficulty in finding the unique solution. Instead of finding global minima, graph cut expansion and gradient descent can be stuck at local minima. However, using quadratic programming techniques gives better results as compared the other minimization methods. In [69], quadratic programming is used for the minimization of the SRR problem which significantly increases the performance as compared to other minimization methods.

3.3.1.2 Learning Based Methods

Learning based algorithms for SRR of RGB images can be adapted to SRR of HS images. In [70], a back propagation neural network (BPNN) is proposed for SRM. In order to train the BPNN, LR fractional images and downsampled LR fractional images are used. After training BPNN, HR SR maps are found using LR fractional images. Self training and low computational cost are the main advantages of this method, however, there is limited metric comparison to analyse the performance of the method. In [71], SRM is achieved by a Hopfield Neural Network (HNN). The method converts SRM to a optimization problem according to spatial dependence. Minimizing the energy function gives the SRM of the LR HS image.

In [72], transfer learning is used for SRR. In this paper, it is assumed that the relationship between LR-HR RGB image is the same as LR-HR HS images. Instead of using LR-HR HS dictionary, end to end mapping is learned by convolutional neural network on the natural images and using pre-trained dictionary each HS band image is enhanced individually. In order to enforce the extracted endmembers to be same both LR and HR HS image, collaborative non matrix factorization is used.

In [73], a compressive sensing (CS) based SRR over a learned dictionary is proposed. According to the CS theory, images or signals can be well-approximated by a suitable basis and fewer measurements or samples can be sufficient to recover them [74]. In this method, first LR HS image is interpolated using bicubic interpolation and called pre-HR HS image. Moreover, using the similarity of spectral curves of the neighbouring pixels,the pre-HR HS image is regularized. Using the samples of pre-HR image, a sparse dictionary is learned. Finally, using the dictionary and sparse coefficients of the regularized pre-HR HS image, HR HS image is obtained. Since sparse representation is capable of expressing the HS images as a linear combination of a few atoms from a predefined dictionary, dimensionality is efficiently reduced in this method. Different sparse representation methods such as K-SVD, ODL and Bayesian can be used in dictionary learning of HS SRR [75].

3.3.2 Fusion Based Methods

Image fusion, also called pan-sharpening, is the process of combining spatial information of HR panchromatic image with the spectral information of LR MS image [76] to obtain a HR MS image. It has been used in many applications such as remote sensing, astronomy, medical imaging, military, security, and surveillance areas [77].

In HS imaging, pan-sharpening is a special case of image fusion problem since the image with high spatial resolution can also be MS image or RGB image. In HS image fusion, the aim is to enhance the resolution of HS image using a MS, RGB or panchromatic (PAN) image. HS images have low spatial resolution with high spectral resolution whereas MS, RGB or PAN images have low spectral with high spatial resolution. Therefore, obtaining an image with both high spectral and spatial resolution using HS image and MS image or RGB image is an attractive research area in HS image processing. However, as compared to MS image fusion, HS image fusion is more challenging task since the spectral range of HS image much wider and number of spectral bands are much higher than MS image.

In the literature, although there are studies which are adapted from the MS fusion methods, more sophisticated methods are also developed for the HS fusion problem [78]. HS fusion problem can be roughly categorized into two classes: Pan-sharpening Based Methods and Subspace Based Methods. It is important to say that image fusion require a good registration, however, in remote sensing images are generally geo-referenced using GPS and IMU data [79]. Therefore, there is no need to apply registration unless more precise registration is required. If so, different image processing techniques can be employed [80].

3.3.2.1 Pan-sharpening Based Methods

Pansharpening based methods are originally developed for pansharpening of MS images [81]. However, they can be extended for fusing HS data [82]. Component Substitution (CS) and Multi resolution analysis (MRA) are widely used pan-sharpening methods used in HS imaging.

CS projects LR HS to another space to separate spatial and spectral information [83]. To do so, first HS image is interpolated to the sizes of PAN image, then sharpened by substituting from the PAN image. The formulation of the method for the panchromatic image P is given in :

$$\widehat{Z}_k = \widehat{Y}_k + g_k \times (P - O_L) \tag{3.24}$$

where g_k is the gain coefficients and O_L is defined as:

$$O_L = \sum_{k=1}^{p} w_k Y_k \tag{3.25}$$

Where weights w measure the spectral overlap among spectral bands and the HR image, Z_k and Y_k are the k^{th} band HR and LR images respectively.

CS based pansharpening method can be extended to solve HS-MS fusion problems using the expression in (3.24) for multiple image sets. In [78], an improved CS based fusion approach for MS-PAN fusion in [84] is adapted for HS-MS fusion problems. In general, CS based fusion is simple to implement and computationally cheap. It renders the spatial details well. On the contrary, spectral distortion caused by discrepancy between HS-MS pair is a critical problem in this method.

Another pansharpening method, MRA, injects the details of the MS image to the interpolated HS image. Details in the MS image are high frequency components of the image. In order to obtain the high pass version of the MS image, original MS image is subtracted from the low pass version of MS image. High passed MS image is multiplied by the gain coefficients to adjust the degree of the injection. According selection of the gain coefficients, injection scheme can differ [81]. The MRA formulation is given in (3.26). M_{LPF} is the low pass filtered version of multispectral image M and G_k is the gain coefficients for the k^{th} band. Different low pass filters can be used to find the details in the MS image [85]. Although MRA based methods have spectral consistency and robustness to aliasing, computational complexity and complicated implementation are the major concerns related to MRA. SFIM-HS and GLP-HS are two extensions of MRA to the HS-MS fusion problem. MRA have better spectral consistency than CS whereas complicated implementation and complexity make the method not preferable [78]. Hybrid methods are also developed using CS and MRA together [86].

$$\widehat{Z}_k = \widehat{Y}_k + G_k \times (M - M_{LPF}) \tag{3.26}$$

3.3.2.2 Subspace Based Methods

Subspace based methods apply a subspace transformation in the fusion process. Both HS and MS data are represented as a set of basis vectors and coefficients in a lower dimensional space. Subspace methods can be further sub-divided into two categories, namely unmixing based and Bayesian based [78]. In the former type, basis vectors are the endmembers in the scene whereas first few principal components of the HS image are used in the latter type.

Coupled Nonnegative Matrix Factorization (CNMF) uses unmixing in the fusion process [87]. HS image is unmixed using VCA and endmembers are initialized. Relating the HS-MS images using the sensor characteristics, HS and MS images alternately unmixed using the NMF according to the cost functions promoting the data fidelity. However, no physical constraint is used in the alternating unmixing process. Convergence condition of the method is reaching the change ratio of the cost functions below a given threshold. HR HS image is reconstructed using spectral signatures and final abundance maps.

In [88], HR image and HR abundances are jointly solved using spectral unmixing and image fusion concepts together. It is stated that LR HS image is a spatially down-sampled version of HS image; and HR RGB image is a spectrally down-sampled version of HR HS image. Firstly, endmembers of HS image are initialized using SISAL. Then, a joint projected gradient based minimization is used to alternately unmix the data and update the endmembers and corresponding HR abundance maps. In the minimization, the physical constraints are also included.

Bayesian approach combines MAP estimation with the fusion process in order to obtain HR HS image [89, 90]. Since the fusion problem is ill-posed, Bayesian approach regularizes the solution by defining prior distributions related to the scene. The observation model relates HR HS image with LR HS image and HR MS image is given in (3.27), (3.28) respectively. According to that model, LR HS image is the blurred and spatially down-sampled version of HR HS image and HR MS is the spectrally down-sampled version of HR HS image.

$$Y = DBZ + N_H \tag{3.27}$$

$$M = RZ + N_M \tag{3.28}$$

Where D and B are the down-sampling and blur operators and R is the spectral response function of the MS camera.Bayesian approaches are using (3.27) and (3.28) as the basic data constraint, they regularize the solution with prior informations.

HySure (hyperspectral superresolution) combines Bayesian and unmixing approaches together suggested by [91]. Different from the previously mentioned fusion methods, HySure imports a vector total variation regularizer (VTV) to the fusion process. Unlike TV, VTV promotes the edges and other details in the scene. Convex optimization problem consists of two data terms; one for the HS measurement and one for the MS measurement. It is minimized by split augmented Lagrangian shrinkage algorithm (SALSA). Moreover, relative spectral and spatial responses of the sensors are also estimated in this study.

Subspace methods are more robust to noise as compared the pansharpening based methods. However, determining the subspace dimension is a critical parameter on the performance of subspace based methods. Moreover, accuracy of the fusion process strictly depends on the reconstruction error of the subspace transformation. In general, data and spectrum consistency on non-overlapping bands of the MS-HS images are two significant metrics showing the actual performance of the fusion method [78].

CHAPTER 4

PROPOSED METHODS

This chapter gives the proposed methods for SRR of HS images. Although there is a large menu of SRR methods using the spectral unmixing concept and abundances for regularization or dictionary learning, there is no attempt to use completely abundances in the SRR process except the SRM methods. However, SRM methods have a different concept and aim to find HR land cover maps instead of HR HS image. To do so, SRM methods assign the sub-pixels to pure endmembers.

It is proposed two approaches for SRR of HS images. First proposed method suggests a MAP based SRR technique for HS images without using any secondary image information. Instead of spectral domain, method uses the abundance map domain in the resolution enhancement process. Since there is no auxiliary information, the SRR problem is severely ill-posed. However, using the correlation of abundances between neighbouring pixels, a smoothness constraint is used to regularize the solution. Moreover, boundary and unity constraints are used to jointly solve the SRR problem. Over smoothing problem is handled using a texture preserved post processing technique.

MAP based method has satisfactory performance when there is no other source of information. However, if an auxiliary HR image is available, it can significantly increase the performance of the SRR. Second method proposes a fusion based SRR method when there exists a secondary HR image. The method also uses abundance map domain in SRR process. Similar to the MAP based approach, quadratic expression is obtained for the SRR problem. The proposed method is the combination of MAP and fusion based approaches. Using MAP approach with fusion concept in a single optimization problem gives the ability to overcome the limitations of both methods. Therefore, the second method gives the optimal solution for the SRR of HS

Figure 4.1: Observation model used in SRR of HS image

images in terms of performance, spectrum consistency and robustness.

4.1 A MAP based Approach

In this section, a MAP based SRR for HS image is proposed, where properties of HS image is used to improve the performance. Moreover, post processing is applied to preserve edges and textures for further improvement. As mentioned in Chapter 3, in SRR, a real imaging system relating an HR HS image *Z* to the LR observation scene *Y* is defined as the observation model. The proposed approach is based on the observation model given in Figure 4.1. Since there exists single HS image, warping operation is not in the observation model. The corresponding mathematical representation of Figure 4.1 is given in (4.1). In this observation model, *Z* and *Y* are used in lexicographical representation in which the rows of each spectral image band is concatenated to construct HR HS image and LR HS image matrices as given in (4.2) and (4.3). In this way, LR HS image *Y* with *p* spectral bands is represented as an *MNxp* size matrix and HR HS image *Z* is a matrix of size $l_1Ml_2N\times p$, where LR single band image size is *MxN*, l_1 and l_2 are down sampling factors in vertical and horizontal directions respectively.

$$Y = DBZ + n \tag{4.1}$$

where

$$Z \triangleq \begin{bmatrix} Z(1) & Z(2) & \cdots & Z(p) \end{bmatrix} \tag{4.2}$$

$$Y \triangleq \begin{bmatrix} Y(1) & Y(2) & \cdots & Y(p) \end{bmatrix} \tag{4.3}$$

$Y(p)$ corresponding to the p^{th} band of LR HS image is of length MN and $Z(p)$ corresponding to the p^{th} band of HR HS image is of length $l_1 M l_2 N$. D is of size $MN \times l_1 M l_2 N$, B is $l_1 M l_2 N \times l_1 M l_2 N$ and n is of size $MN \times p$.

Using this observation model, the HR HS image estimate can be found by minimizing l-norm of the difference between the observed LR HS image and the blurred and down-sampled HR HS image as below:

$$\widehat{Z} = arg\, min_Z ||DBZ - Y||_l^l \tag{4.4}$$

In this study, Frobenius norm is chosen (i.e. l=2) to estimate the HR HS image. From LMM, HR and LR HS image can be written using the HR and LR abundance map matrices (A_z and A_y) multiplied by the spectral signature matrix of *P*; as given in (4.5) and (4.6):

$$Z = A_z P \tag{4.5}$$

$$Y = A_y P \tag{4.6}$$

$$A_z \triangleq \begin{bmatrix} A_z(1) & A_z(2) & \cdots & A_z(E) \end{bmatrix} \tag{4.7}$$

$$A_y \triangleq \begin{bmatrix} A_y(1) & A_y(2) & \cdots & A_y(E) \end{bmatrix} \tag{4.8}$$

where *E* shows the number of endmembers in the scene and *P* is a matrix of size $E \times p$ and each row of *P* shows the spectral signature of an endmember. $A_z(i)$ and $A_y(i)$ are the i^{th} column of the matrix A_z and A_y respectively.

Plugging (4.5) and (4.6) into the minimization problem given in (4.4), the expression can be written in terms of spectral signatures and abundances of the scene:

$$\widehat{A_z P(i)} = argmin_{A_z P(i)} ||DBA_z P(i) - A_y P(i)||_2^2 \tag{4.9}$$

where $P(i)$ shows the i^{th} column of the matrix *P*. In (4.9), matrix *P* has no effect on minimization and can be removed. Hence, (4.9) can be written using summation:

$$\widehat{A}_z = argmin_{A_z} \sum_{e=1}^{E} ||DBA_z(e) - A_y(e)||_2^2 \tag{4.10}$$

Thus, in the proposed approach, (4.10) is minimized. In doing so, the SRR minimization problem can be solved in the abundance map domain, as opposed to the spectral domain. However, since the SRR is an ill-posed inverse problem, the data constraint (DC) term in (4.10) should be regularized with additional constraints. It is utilized the smoothness constraint (SC) that promotes smooth HR abundances, the unity constraint (UC) that guarantees the sum of abundances for each pixel in a HS image to be equal to one and the bounding constraint (BC) that abundances are between zero and one. Using these constraints, the total energy function is minimized and solved for the HR abundances of endmembers. The block diagram of whole process is given in Figure 4.2.

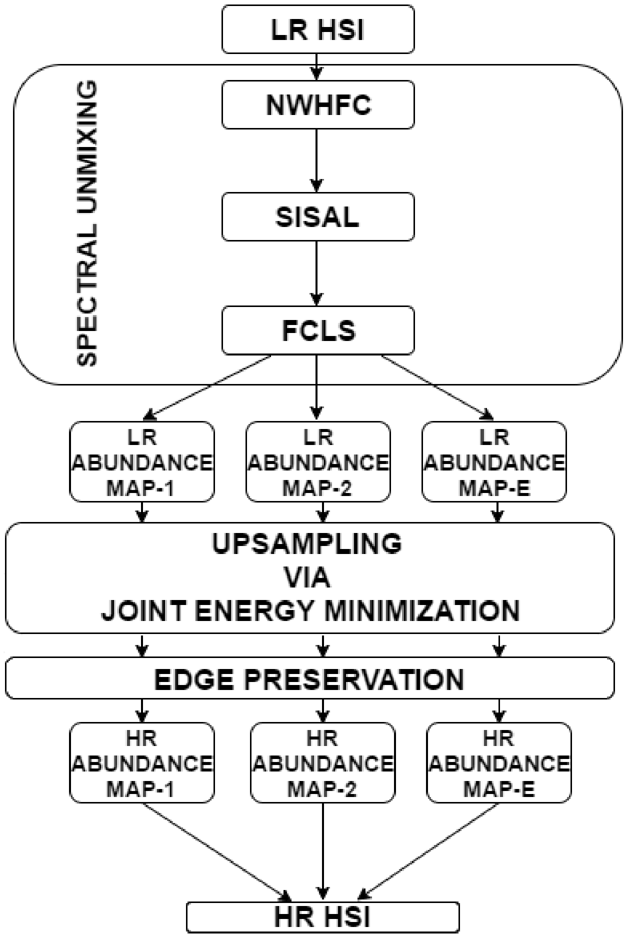

Figure 4.2: Block diagram of the proposed method

4.1.1 Spectral Unmixing

Hyperspectral images are typically low resolution, as a result each pixel may contain more than one endmember in a single pixel. However, it is known that there is a spatial correlation of endmembers between neighborhood pixels [92]. Moreover, there is a dependency between endmembers in each pixel which can be used as an information in SRR. Therefore, using the abundance domain instead of the spectral domain gives the ability to use the information that is present across the spectral bands since separate band SRR does not make use of the inherent low dimensionality of the spectral data which which can effectively improve the robustness against noise. Therefore, in the proposed approach, first step is to apply spectral unmixing to find the abundances in the observed scene. Since the proposed approach has sequential stages, an error in any stage is forwarded to the next stage. In other words, error is accumulating between stages. Therefore, spectral unmixing becomes the most crucial part of the proposed method. Small errors in spectral unmixing could result in critical performance decrease in the proposed approach.

As mentioned in Chapter 2, unmixing consists of three main steps, namely determination of number of endmembers, endmember extraction and estimation of abundances. VD concept is introduced in Chapter 2. In [18], the VD of HS image is determined by HFC method, which uses a Neyman-Pearson detection theory based thresholding. A modified version, noise whitened HFC (NWHFC) has a preprocessing noise whitening step to remove the second order statistical correlation [17]. In proposed approach, after comparing various methods suggested in Chapter 2, NWHFC-based thresholding VD is selected for its better performance.

After the number of endmembers in the scene is determined, the endmembers are extracted from HS data. Since the pure pixel assumption is a hard constraint for LR images, an endmember detection algorithm without the pure pixel assumption is more suitable. In [93], the endmember extraction algorithms without pure pixel assumption were compared and Splitted Augmented Lagrangian (SISAL) was found to perform better than the competing algorithms in the literature. Thus, in this study, SISAL algorithm is used for endmember extraction. In SISAL, unmixing is achieved by finding the minimum volume simplex containing the HS data. This optimization problem is solved by a sequence of variable splitting augmented Lagrangian optimizations [25]. Finally using FCLS, abundance maps of the extracted endmembers are estimated. These abundance maps, called as LR abundance maps, are used in the SRR process.

4.1.2 SRR using Joint Energy Minimization

Once the LR abundance maps are known, (4.10) is the basic data cost function for the estimation of the HR abundance maps. However, this is an ill-posed inverse problem (i.e. there is no unique solution and the solutions are not stable). Additional information is needed to compensate the missing solution. Regularization is the process of introducing additional information in order to solve ill-posed inverse problems [94]. In other words, regularization is implemented as a penalty factor in the cost function.

In image processing, smoothness prior has been one of the most popular prior assumptions [95]. It assumes that a particular point in an image, there are no sharp changes. There is a coherency between neighbouring pixels. In the proposed approach, smoothness prior used as the regularizer and the cost function is constructed as in (4.11). Here, C_D is the data cost function and C_S is the smoothness cost function used as regularizer. C_{MAP} is the total cost function and λ adjusts the degree of the smoothness. Higher λ values give smoother solution whereas lower λ results in a rough image.

$$C_{MAP} = C_D + \lambda C_S \tag{4.11}$$

The equation in (4.10) is a quadratic function for each endmember. Concatenating these equations with defining new matrices gives a single quadratic function for the data cost function which is given in (4.12). This gives the ability to solve a single quadratic cost function.

$$C_D = z^T D_{DB}^T D_{DB} z - z^T D_{DB}^T y - y^T D_{DB} z + y^T y \tag{4.12}$$

where

$$z \triangleq \begin{bmatrix} A_z(1) \\ A_z(2) \\ \vdots \\ A_z(E) \end{bmatrix} \tag{4.13}$$

$$y \triangleq \begin{bmatrix} A_y(1) \\ A_y(2) \\ \vdots \\ A_y(E) \end{bmatrix} \tag{4.14}$$

$$D_{DB} \triangleq \begin{bmatrix} DB & 0 & \cdots & 0 \\ 0 & DB & \cdots & 0 \\ \vdots & \vdots & \ddots & \vdots \\ 0 & 0 & \cdots & DB \end{bmatrix} \tag{4.15}$$

In (4.12), $z^T D_{DB}^T y$ and $y^T D_{DB} z$ are scalar terms. As seen from (4.16), they are equal to each other.

$$(z^T D_{DB}^T y)^T = y^T D_{DB} z \tag{4.16}$$

Moreover, $y^T y$ is a constant term and has no effect on the minimization of (4.12). Therefore, it can removed; and the final form of C_D is given in (4.17):

$$C_D = z_T D_{DB}^T D_{DB} z - 2y^T D_{DB} z \tag{4.17}$$

After obtaining the data cost function, the regularization term should be determined. In this study, it is used an MRF-based smoothness prior as our regularizer, which assumes that the physical properties in a neighborhood present a coherency and do not change abruptly [96]. An MRF model constructs the global joint distribution from local neighbourhood relations. It is an undirected graph in which the nodes represent the random variables. A node is independent of all other nodes except the neighbour nodes, which are called as cliques.

For a HR abundance map $A_z(e)$ of endmember *e*, the MRF based smoothness regularizer, C_{Se}, is given in (4.18):

$$C_{Se} = \sum_{j=1}^{4} ||A_z(e) - \tilde{A}_{zclique}(e)(j)||_2^2 \tag{4.18}$$

where $\tilde{A}_{zclique}(e)(j)$ is the 4-neighbourhood pixel vector for endmember *e*. Extending the MRF regularizer, equation (4.18) becomes:

$$C_{Se} = [||A_z(e) - S_x^1 A_z(e)||_2^2 + ||A_z(e) - S_x^{-1} A_z(e)||_2^2 + \\ ||A_z(e) - S_y^1 A_z(e)||_2^2 + ||A_z(e) - S_y^{-1} A_z(e)||_2^2] \tag{4.19}$$

In (4.19), S_x^n and S_y^n show the *n* pixel shift operations in horizontal and vertical directions respectively. Analysing the first term in (4.19), it can be rewritten as:

$$\begin{aligned} ||A_z(e) - S_x^1 A_z(e)||_2^2 &= ||(I - S_x^1) A_z(e)||_2^2 \\ &= A_z(e)^T (I - {S_x}^1)^T (I - {S_x}^1) A_z(e) \end{aligned} \tag{4.20}$$

Using (4.20), equation (4.19) can be expressed as:

$$\begin{aligned} C_{Se} = & A_z(e)^T (I - {S_x}^1)^T (I - {S_x}^1) A_z(e) \\ & + A_z(e)^T (I - {S_x}^{-1})^T (I - {S_x}^{-1}) A_z(e) \\ & + A_z(e)^T (I - {S_y}^1)^T (I - {S_y}^1) A_z(e) \\ & + A_z(e)^T (I - {S_y}^{-1})^T (I - {S_y}^{-1}) A_z(e) \end{aligned} \tag{4.21}$$

Equation (4.21) is the smoothness regularizer for each endmember. Similar to the data cost function, (4.21) can be extended to cover all endmembers in a single quadratic smoothness function. Defining new matrices, the final quadratic regularizer is given in (4.22).

$$C_S = z^T [(I - D_{S_x}^1)^T (I - D_{S_x}^1) + (I - D_{S_x}^{-1})^T (I - D_{S_x}^{-1}) \\ + (I - D_{S_y}^1)^T (I - D_{S_y}^1) + (I - D_{S_y}^{-1})^T (I - D_{S_y}^{-1})] z \tag{4.22}$$

where

$$D_{Sx} \triangleq \begin{bmatrix} S_x & 0 & \cdots & 0 \\ 0 & S_x & \cdots & 0 \\ \vdots & \vdots & \ddots & \vdots \\ 0 & 0 & \cdots & S_x \end{bmatrix} \tag{4.23}$$

$$D_{Sy} \triangleq \begin{bmatrix} S_y & 0 & \cdots & 0 \\ 0 & S_y & \cdots & 0 \\ \vdots & \vdots & \ddots & \vdots \\ 0 & 0 & \cdots & S_y \end{bmatrix} \tag{4.24}$$

After finding the data and smoothness quadratic functions, the total quadratic cost function, C_{MAP}, can be reconstructed combining the cost functions given in (4.17) and in (4.22) with a regularizer coefficient λ and (4.11) is obtained.

To find the local minimum, solution space can be narrowed using the constraints specific to abundance maps. First constraint is the unity constraint (UC) in which the sum of the abundances in hyperspectral data for a single pixel should be unity and mathematical formulation is given in (4.25). Second constraint is the bounding constraint (BC) that restricts range of the values of $A_z(e)$ between zero and unity.

$$UC = \sum_{e=1}^{E} A_z(e) = \underline{1} \tag{4.25}$$

In (4.25), $\underline{1}$ is a column vector of size l_1Ml_2N in which every element is one. To convert the problem into a form of quadratic minimization problem, (4.25) can be written as (4.26), using the definitions in (4.27) and (4.28):

$$A_{eq}z = b_{eq} \tag{4.26}$$

where

$$A_{eq} \triangleq \begin{bmatrix} I_1 & I_2 & \cdots & I_E \end{bmatrix} \tag{4.27}$$

$$b_{eq} \triangleq \underline{1} \tag{4.28}$$

$I_1, ..., I_E$ are the identity matrices of size $l_1Ml_2Nxl_1Ml_2N$ and E shows the number of endmembers.

Minimizing the cost function C_{MAP} given in (4.11) with the UC given in (4.25) and BC estimates the HR abundance maps. Using a single quadratic function gives a joint minimization. Moreover, since minimization problem is quadratic, local minimum point can be found using quadratic programming (QP) methods.

4.1.3 Quadratic Programming

A quadratic program is an optimization problem in which a quadratic objective function is either minimized with respect to finite number of variables subject to inequality and/or equality constraints [97]. A general quadratic function of finite number of variables $z = (z_1, z_2..., z_n)^T$ with both equality and inequality constraints is in the form given in (4.29). Equality and inequality constraints are given in (4.30) and (4.31) respectively.

$$\text{minimize} \quad g(z) = \frac{1}{2}z^T H z + f^T z \tag{4.29}$$

$$\text{subject to} \quad A_{eq} z = b_{eq} \tag{4.30}$$

$$l \leq z \leq h \tag{4.31}$$

When the objective function g(z) is strictly convex for all points then the problem has a unique local minimum which is also the global minimum [97]. To guarantee strictly convexity of objective function necessary and sufficient condition is that H should be positive definite.

In the proposed approach, the cost function C_{MAP} can be rewritten in quadratic form given in (4.29) by defining H_{MAP}, f_{MAP}, l and h as:

$$\begin{aligned} H_{MAP} \triangleq\ & 2D_{DB}^T D_{DB} + 2\lambda.[(I - D_{Sx}^1)^T(I - D_{Sx}^1) + (I - D_{Sx}^{-1})^T(I - D_{Sx}^{-1}) \\ & + (I - D_{Sy}^1)^T(I - D_{Sy}^1) + (I - D_{Sy}^{-1})^T(I - D_{Sy}^{-1})] \end{aligned} \tag{4.32}$$

$$f_{MAP} \triangleq (-2y^T D_{DB})^T \tag{4.33}$$

$$\underline{0} \leq z \leq \underline{1} \quad (l = 0 \quad and \quad h = 1) \tag{4.34}$$

After these rearrangements, the problem can be solved using QP solving techniques such as the interior point method which has been proven to work well in practice [98]. In this study, QP problem is also minimized using the interior point method; and the global minimum point gives the HR abundance maps of the HR HS image.

4.1.4 Post Processing to Solve Oversmoothness

In the cost function, the value of λ is very critical. Higher λ values over smooth the image whereas lower λ values preserve the textures but lead energy minimization into an ill-posed inverse problem. Therefore, finding the optimum λ value is a hard problem and instead of using a constant λ, the method suggested by [1] is used to preserve edges and textures. In this method, cost function is minimized with two times with two different regularization parameters; λ_1 and λ_2 as shown in Figure 4.3. First regularization parameter is chosen to be very close to zero (i.e. $\lambda_1 \approx 0$) and it creates a noisy estimate of the image while preserving textures. This solution can be called as the Maximum Likelihood (ML) estimate. On the other hand, the second regularization parameter is chosen to be much greater than the first one ($\lambda_1 \ll \lambda_2$) and creates an over smoothed SRR estimate. Similarly, it can be called as the MAP estimate. The difference of the first estimate and the second estimate gives the high frequency (HF) image that is composed of edges and textures. Then, Gabor filter is applied to this HF image to detect textures. General form of a Gabor filter with direction of filter θ is given in (4.35). They are family of filters with different orientations. HF image is filtered using these filters separately and for each filter output, the pixels below a predefined threshold are masked. Then, these masked filter outputs are summed to obtain the restored HF image. Eight directions are used between 0 and 180 degree which is sufficient due to the symmetry of the cosine function. In (4.35), λ is inversely proportional to the frequency of the carrier and σ is related to the spread of the Gaussian envelope. After Gabor filtering operation, the restored HF image is summed with the MAP estimate to obtain texture preserved final image as shown in Figure 4.3.

$$G(x,y) = e^{\frac{x^2+y^2}{\sigma^2}} \cos(\frac{2\pi}{\lambda}(x\cos\theta + y\sin\theta)) \tag{4.35}$$

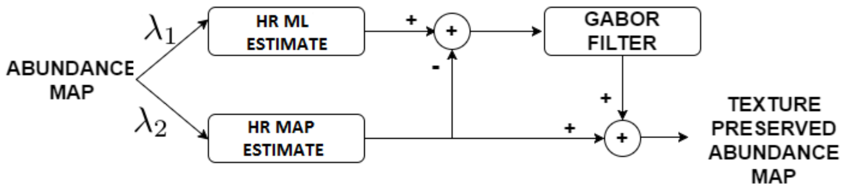

Figure 4.3: Block diagram of the texture preservation

This procedure is applied to each abundance map; so texture preserved HR abundance maps are obtained for all endmembers. Texture preserving operation does not violate the UC since both the ML and the MAP estimates of the abundances satisfy the UC. Hence, summing the unity gain filtered difference of them with MAP estimate also satisfies the UC. Using these HR abundances and spectral signature matrix P, the final HR HS image is constructed.

4.2 A MAP based Fusion Approach

MAP based approaches use image priors to increase the resolution of images. However, if an additional coinciding source of information (i.e. MS or RGB image) with LR HS image is available, then it can be used in the SRR process. In this section, a fusion based method is proposed for the SRR of HS images. The novelty of the method is using the only abundance domain in the resolution enhancement process. Moreover, problem is regularized using a MAP framework. Similar to the previous section, the inverse problem is converted to a joint quadratic energy minimization problem in the abundance domain. The block diagram of the proposed fusion based approach is given in Figure 4.4. Throughout the section, it is assumed that a HR RGB image is available with LR HS image. First, a fusion based approach is introduced, then it is regularized using the proposed MAP method.

In the previous section, the inverse problem is defined with an observation model.

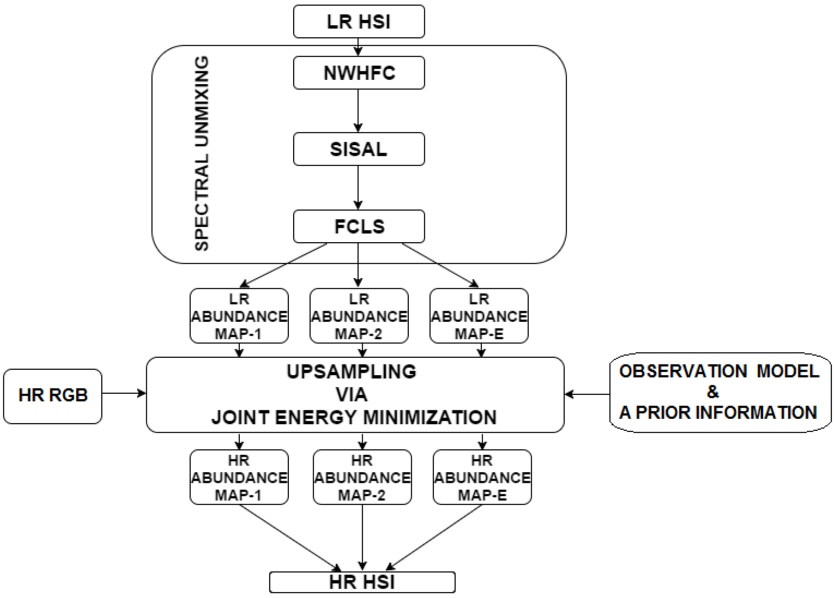

Figure 4.4: MAP based Fusion Approach

Same model can be used for the MAP based fusion method. Spectral response function of the RGB camera can be used to relate the HR HS image and HR RGB. First, the inverse problem can be constructed using the one component of RGB image then it can be extended to other two components. For example, equation (4.36) shows the relation between HR HS image (Z_{HSI}) and Red component (Z_{RED}) of HR RGB image.

$$Z_{RED} = Z_{HSI} R_{RED}^T \tag{4.36}$$

In (4.36),R_{RED} shows the spectral response function of the red component of the RGB image.

From section 4.1.1, it is known that HR HS image can be written using abundance maps (A_Z) and spectral signature matrix (P):

$$Z_{RED} = A_Z P R_{RED}^T \tag{4.37}$$

Using (4.38), (4.37) can be rewritten as in (4.39).

$$A_Z P = A_Z(1)(P^T(1))^T + A_Z(2)(P^T(2))^T + \cdots + A_Z(E)(P^T(E))^T \tag{4.38}$$

$$Z_{RED} = A_Z(1)(P^T(1))^T R_{RED} + A_Z(2)(P^T(2))^T R_{RED} + \cdots + A_Z(E)(P^T(E))^T R_{RED} \tag{4.39}$$

Using the matrices definitions in (4.40) and (4.41) and with the help of the identity in (4.42), (4.39) can be written as in (4.43)

$$w_{i,RED} \triangleq (P^T(i))^T R_{RED} \tag{4.40}$$

$$w_{di,RED} \triangleq \begin{bmatrix} w_{i,RED} & 0 & \cdots & 0 \\ 0 & w_{i,RED} & \cdots & 0 \\ \vdots & \vdots & \ddots & \vdots \\ 0 & 0 & \cdots & w_{i,RED} \end{bmatrix} \tag{4.41}$$

$$A_Z(i) w_{i,RED} = \begin{bmatrix} w_{i,RED} & 0 & \cdots & 0 \\ 0 & w_{i,RED} & \cdots & 0 \\ \vdots & \vdots & \ddots & \vdots \\ 0 & 0 & \cdots & w_{i,RED} \end{bmatrix} A_Z(i) \tag{4.42}$$

$$Z_{RED} = w_{d1,RED} A_Z(1) + w_{d2,RED} A_Z(2) + \cdots + w_{dE,RED} A_Z(E) \tag{4.43}$$

The right hand side of (4.44) can be rewritten concatenating the triangular matrices:

$$Z_{RED} = \begin{bmatrix} w_{d1,RED} & w_{d2,RED} & \cdots & w_{dE,RED} \end{bmatrix} \begin{bmatrix} A_z(1) \\ A_z(2) \\ \vdots \\ A_z(E) \end{bmatrix} \tag{4.44}$$

Using the matrix definitions in (4.13), (4.45) and (4.46), the relation between HR RGB image and HR abundance maps is found as given in (4.47).

$$W_{RGB} \triangleq \begin{bmatrix} w_{d1,RED} & w_{d2,RED} & \cdots & w_{dE,RED} \\ w_{d1,GREEN} & w_{d2,GREEN} & \cdots & w_{dE,GREEN} \\ w_{d1,BLUE} & w_{d2,BLUE} & \cdots & w_{dE,BLUE} \end{bmatrix} \tag{4.45}$$

$$Z_{RGB} \triangleq \begin{bmatrix} Z_{RED} \\ Z_{GREEN} \\ Z_{BLUE} \end{bmatrix} \tag{4.46}$$

$$Z_{RGB} = W_{RGB} z \tag{4.47}$$

After these arrangements, the inverse problem is obtained using the abundance maps and HR RGB image:

$$\widehat{z} = arg\ min_z ||W_{RGB} z - Z_{RGB}||_l^l \tag{4.48}$$

Extending (4.48), the cost function (C_{fuse}) can be defined as:

$$C_{fuse} = z_T W_{RGB}^T W_{RGB} z - z^T W_{RGB}^T Z_{RGB} - Z_{RGB}^T W_{RGB} z - Z_{RGB}^T Z_{RGB} \tag{4.49}$$

Last term in (4.49) is constant and can be removed from the cost function. Moreover, second and third term in (4.49) are scalar and transpose of each other, and can be written as a single term. Therefore, cost function becomes:

$$C_{fuse} = z^T W_{RGB}^T W_{RGB} z - 2 Z_{RGB}^T W_{RGB} z \tag{4.50}$$

Similar to the previous section, the cost function in (4.50) is quadratic with the following definitions:

$$H_{fuse} \triangleq 2 W_{RGB}^T W_{RGB} \tag{4.51}$$

$$f_{fuse} \triangleq (-2Z_{RGB}^{T}W_{RGB})^{T} \tag{4.52}$$

Combining (4.50) with the MAP framework given in the previous section, a cost function for a MAP based fusion is obtained:

$$C_{MAP\_fuse} = \sigma_{MAP}C_{MAP} + \sigma_{fuse}C_{fuse} \tag{4.53}$$

In (4.53), C_{MAP_fuse} is the total cost function. σ_{MAP} and σ_{fuse} are the weights of the cost functions of MAP and fusion based approaches. C_{MAP} and C_{fuse} are the cost functions defined in (4.11) and (4.50) respectively.

The weights of the two approaches are adjusted using a weight parameter w in the following expression:

$$\frac{\sigma_{fuse}}{\sigma_{MAP}} = w\frac{norm(H_{MAP})}{norm(H_{fuse})} \tag{4.54}$$

Since both MAP and fusion approaches are quadratic, a quadratic function is obtained for the MAP based fusion method with the following expressions for the objective function:

$$H_{MAP\_fuse} = H_{MAP} + w\frac{norm(H_{MAP})}{norm(H_{fuse})}H_{fuse} \tag{4.55}$$

$$f_{MAP\_fuse} = f_{MAP} + w\frac{norm(H_{MAP})}{norm(H_{fuse})}f_{fuse} \tag{4.56}$$

Solving the quadratic function defined by the parameters given in (4.55), (4.56) with UC and BC constraints gives the HR abundance maps. Using these maps and spectral signatures, HR HS image reconstructed. No need to use texture preserving since HR RGB image gives the texture information for the HR HS image.

MAP based approach has limited performance compared to fusion based approaches, however, performance is consistent throughout the bands. On the other hand, fusion based approaches have better performance in the matching band range of the auxiliary

HR image whereas their performance sharply decreases in the other bands of the spectrum. Proposed MAP based fusion approach overcomes the limitations of both mentioned approaches. It has superior performance in all the bands of the spectrum.

CHAPTER 5

RESULTS

In this chapter, quantitative experimental results on various hyperspectral datasets are given.

5.1 Performance Metrics

The SRR algorithms are compared quantitatively using four measures: (i) peak signal-to-noise ratio (PSNR), (ii) structural similarity index measure (SSIM), (iii) spectral angle mapper (SAM), and (iv) relative dimensionless global error in synthesis (ERGAS).

The first measure, PSNR, is the ratio between the maximum possible power of a signal and the power of the distorting noise [99]. PSNR is expressed in terms of the logarithmic decibel scale (dB) and higher PSNR means better match of the estimated and reference image. Given an estimated image y and a reference image x both encoded using b bits per pixel, PSNR is computed as:

$$PSNR(x, y) = 10 \log_{10} \left(\frac{2^b - 1}{\frac{1}{mn} \sum_{i=0}^{m-1} \sum_{j=0}^{n-1} [x(i, j) - y(i, j)]^2} \right) \tag{5.1}$$

The second measure, SSIM, is based on the human visual perception which is more sensitive to structural information [100]. PSNR estimates the absolute error whereas SSIM considers image degradation as perceived change in structural information. The SSIM is defined as:

$$SSIM(x,y) = \frac{(2\mu_x\mu_y + C_1)(2\sigma_{xy} + C_2)}{({\mu_x}^2{\mu_y}^2 + C_1)({\sigma_x}^2 + {\sigma_y}^2 + C_2)} \tag{5.2}$$

where μ_x and μ_x are the mean values of the pixels in a window for images x and y. σ_x^2, σ_y^2 and σ_{xy} are the variances of x, y and the covariance of x and y respectively. C_1 and C_2 are two constants used to avoid instability, and are set to 0.01 and 0.03 respectively as in [100].

The third measure, SAM, is one of the most common metrics in hyperspectral processing [101]. SAM is the angle between the estimated i^{th} pixel $x(i)$ and the ground truth i^{th} pixel $y(i)$, averaged over the whole image [102]. It measures the average spectral distortion in radians between two images and given in (5.3) where N is the number of pixels in the image.

$$SAM(x,y) = \frac{1}{N}\sum \arccos \frac{x(i)^T y(i)}{||x(i)||_2||y(i)||_2} \tag{5.3}$$

Last measure is ERGAS which is used to measure the radiometric distortion in the images [103]. The main difference between SAM and ERGAS is that the former is used to measure spectral distortion whereas the latter is concerned with the radiometric distortion. Therefore, both metrics are the most common metrics for quantitative comparisons in HS imaging applications.

$$ERGAS(x,y) = \frac{100}{SR}\sqrt{\frac{1}{p}\sum_{i=1}^{p}(\frac{RMSE(x_i, y_i)}{\mu_i})_2} \tag{5.4}$$

Where p is the total number of bands, SR is the scale ratio of HS and MS spatial resolutions, and μ_i is the average of the i^{th} band. A zero ERGAS value denotes the absence of radiometric distortion, but possible spectral distortion.

In these metrics, while higher PSNR and SSIM measures indicate a better match between the estimation and the ground truth. However, lower SAM and ERGAS values are desired for smaller distortions.

5.2 Experiments on Real Hyperspectral Image Datasets

The proposed method is applied to three different datasets. The first dataset is the Cave dataset which consists of 32 scenes [104]. It is in the 400 nm to 700 nm wavelength range with steps of 10 nm. The resolution is 512x512 pixels. The second database, called Harvard [105], has 50 indoor and outdoor images recorded under daylight illumination. The spatial resolution of these images is 1392x1040 pixels, with 31 spectral bands of 10 nm width, ranging from 420 nm to 720 nm. The last dataset is the Hyperspectral Remote Sensing Scenes (HRSS) dataset of urban areas consisting of 5 images [106]. The area covered is comprised of different sizes of images, with hundred spectral bands from 380 nm to 2500 nm. For all the experiments, centre of the image with patch size 256x256 is used as the reference image. For the Harvard experiment, in the captured images there are movement (or dust) in some regions and these regions are masked out. Therefore, the images with no problem in the centre are used in the experiments. Similarly, for the Cave experiment, 24 images are used in the experiments. In HRSS dataset, corrected images (i.e. indian_pines_-corrected and salinas_corrected) are smaller than 256x256, therefore, for salinas_-corrected and indian_pines_corrected images, image patches are used 200x200 and 128x128, respectively.

These reference images form the ground truth and are used to evaluate the performance of the proposed methods. The LR HS images are obtained from the HR images by blurring the HR HS image using a 3x3 uniform kernel, down sampling the result by two and adding 30 dB additive white Gaussian noise signal.

The proposed methods are compared with three different methods. The first method is called Yang *et al.*'s method which is a state-of the art single image SRR method [107]. This method preserves the structures in the image succesfully. Second is the Xiong *et al.*'s method which is a very recent single image SRR method for HS images [58]. These methods are selected for the fair comparison with our single image MAP based SRR methods for HS images. In addition, a fusion based state-of-the-art method by Lanaras *et al.* is selected. Lanaras *et al.*'s method is a hyperspectral SR method based on the image fusion of a HR RGB image and a LR HS image [88]; which was shown to have a better performance than several other hyperspectral

SR methods [88]. Methods are explained in Chapter 3. In the experimental results, proposed MAP approach without post processing is also given to understand the effect of texture preserving operation on the performance. In experiments, MAP shows the proposed approach without post processing, TP MAP shows the texture preserving MAP method and MAP fusion shows the proposed fusion approach. For the fusion based methods,it is important to note that auxiliary HR image is assumed to be RGB in the experiments. Performance can differ when the auxiliary image is panchromatic or MS. Moreover, HR RGB input images are created by integrating over the original spectral channels of HR HS image using the spectral response of a typical digital camera. Not only HR images but also high pass filtered of the corresponding HR images are also given for a better comparison.

In the metric results, the best performance in each image is underlined for the single image SRR methods and written bold for the fusion based methods. Moreover, in the visual results, for Cave and Harvard datasets RGB bands are used to show HR HS images whereas for the HRSS dataset false RGB images are generated using $60^{th}, 70^{th}\, and \, 80^{th}$ bands of the HR HS image.

Before giving the experimental comparisons, visual and metric results are given to see the effect of the parameters on the performance for the proposed methods.

5.2.1 Effect of λ on Images

In MAP based method, λ value is the most critical parameter that affects the performance. Higher λ smooths the image whereas lower values result in unstable solutions. Equally weighted case is λ_0 and expressed in 5.5. In Figure 5.1, the effect of λ can be seen for different λ values. Metric results are given in Table 5.1.

$$\lambda_0 = \frac{norm(H_{data})}{norm(H_{smoothness})} \tag{5.5}$$

Where

$$H_{data} = 2D_{DB}^{T} D_{DB} \tag{5.6}$$

$$\begin{aligned} H_{smoothness} = 2[&(I - D_{Sx}^{1})^T (I - D_{Sx}^{1}) + (I - D_{Sx}^{-1})^T (I - D_{Sx}^{-1}) \\ &+ (I - D_{Sy}^{1})^T (I - D_{Sy}^{1}) + (I - D_{Sy}^{-1})^T (I - D_{Sy}^{-1})] \end{aligned} \tag{5.7}$$

Table5.1: Metric results for different λ values

	PSNR	SSIM	SAM	ERGAS
$\lambda = 0$	23.480	0.340	0.332	136.286
$\lambda = 0.01\lambda_0$	29.634	0.661	0.158	58.929
$\lambda = 0.1\lambda_0$	**33.028**	0.863	**0.108**	**42.934**
$\lambda = \lambda_0$	32.222	0.857	0.116	48.778
$\lambda = 10\lambda_0$	32.879	**0.962**	0.122	55.494
$\lambda = 100\lambda_0$	28.478	0.939	0.175	74.665

As seen from the Table 5.1, λ values between $0.1\lambda_0$ and λ_0 have better performance in terms of PSNR, SAM and ERGAS metrics. In the experiments, $0.1\lambda_0$ is used for the λ.

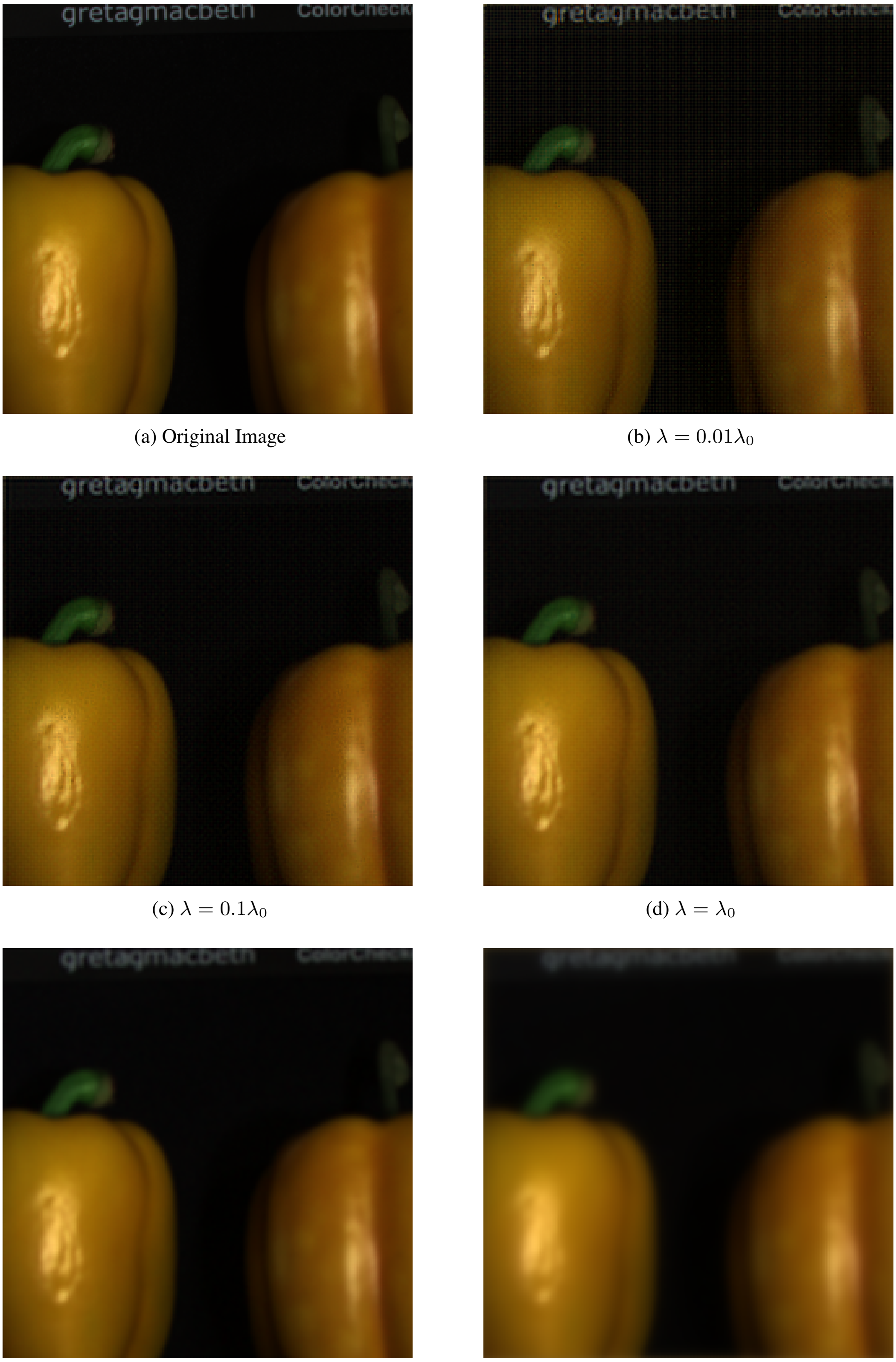

(a) Original Image

(b) $\lambda = 0.01\lambda_0$

(c) $\lambda = 0.1\lambda_0$

(d) $\lambda = \lambda_0$

(e) $\lambda = 10\lambda_0$

(f) $\lambda = 100\lambda_0$

Figure 5.1: MAP based SRR results for different λ values

5.2.2 Effect of Balance Between MAP and Fusion on MAP Fusion Method

In MAP Fusion method, weights of the methods can be adjusted using the expression:

$$H_{MAP\_fuse} = H_{MAP} + \sigma H_{fuse} \tag{5.8}$$

In the proposed approach, MAP and Fusion methods are weighted in the optimization. In order to do so, assuming the weight of the MAP method as unity, the weight of the fusion method is defined in 5.9.

$$\sigma \triangleq w\sigma_0 \tag{5.9}$$

where w is the weight term and σ_0 is defined as:

$$\sigma_0 \triangleq \frac{norm(H_{MAP})}{norm(H_{fuse})} \tag{5.10}$$

In order to see the effect of σ, experiments are conducted for different values and can be seen in Figure 5.2.

Table5.2: Metric results for different σ values

	PSNR	SSIM	SAM	ERGAS
$\sigma = 0$	31.022	0.920	0.110	27.026
$\sigma = 0.01\sigma_0$	30.921	0.924	0.105	25.697
$\sigma = 0.1\sigma_0$	32.689	0.940	0.087	20.962
$\sigma = \sigma_0$	34.688	**0.946**	0.075	18.277
$\sigma = 10\sigma_0$	**35.598**	0.945	**0.072**	**17.694**
$\sigma = 100\sigma_0$	35.054	0.930	0.079	19.551

Similarly, from Table 5.2, σ values between σ_0 and $100\sigma_0$ have better performance. In the experiments, $20\sigma_0$ is used for the σ.

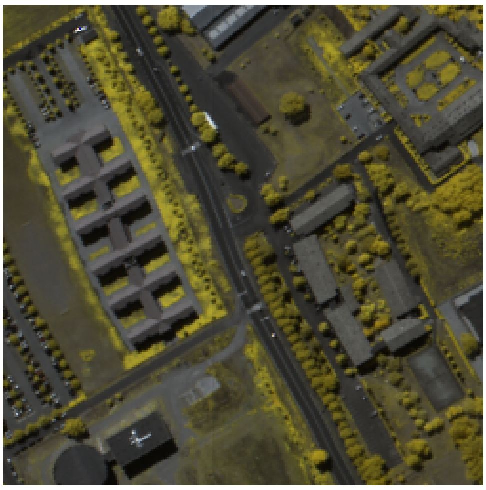

(a) Original Image

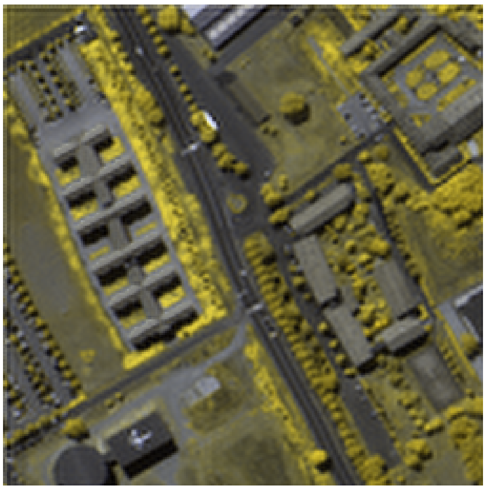

(b) $\sigma = 0.01\sigma_0$

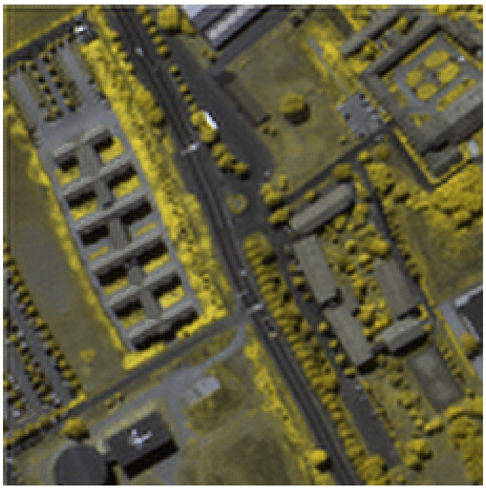

(c) $\sigma = 0.1\sigma_0$

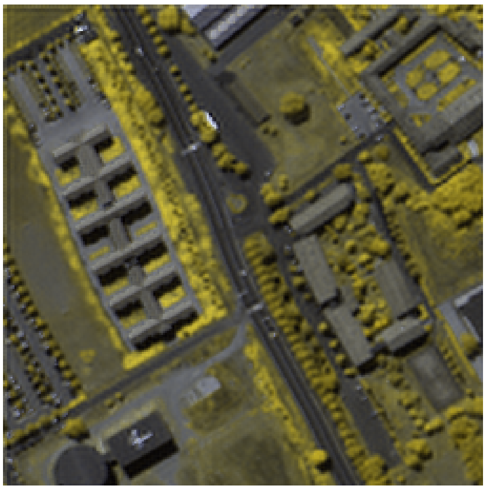

(d) $\sigma = \sigma_0$

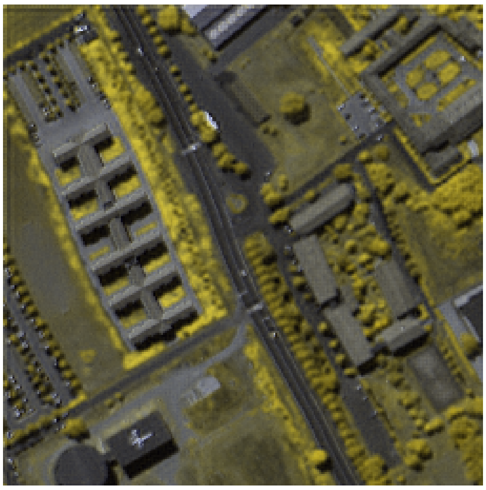

(e) $\sigma = 10\sigma_0$

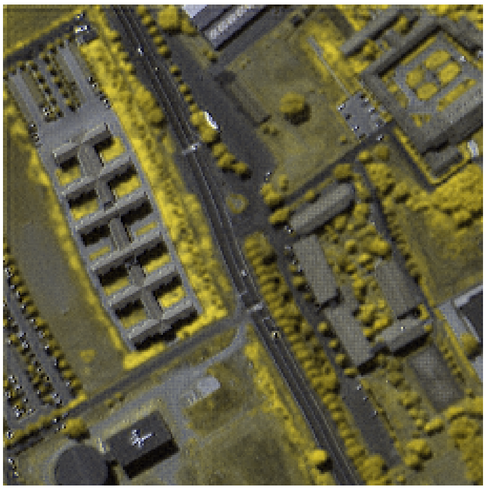

(f) $\sigma = 100\sigma_0$

Figure 5.2: SRR results for different σ values

5.2.3 Effect of Spectral Unmixing on the Performance

Spectral unmixing is the crucial step of the proposed methods. If the number of endmembers are underestimated, then performance will strictly decrease. However, if the number of endmembers are overestimated, then complexity will increase. Therefore, determination of correct number of endmembers has a key role on the performance of the proposed methods. In order to analyse the dependency, a synthetic data is generated using four endmembers and performance plots are given in Figure 5.3 for different number of endmembers. In Figure 5.3, vertical dashed line shows the correct number of endmembers. As clearly seen from the figure, under-estimation of the number of endmembers results in lower performance. On the contrary, over-estimation of the number of endmembers has little effect on the performance. Since in the proposed methods, splitting an abundance to multiple endmembers does not violate any constraints except the smoothness. Therefore, over-estimation of the number of endmembers has stable performance. The increase in the computational complexity is the main drawback of the over-estimation.

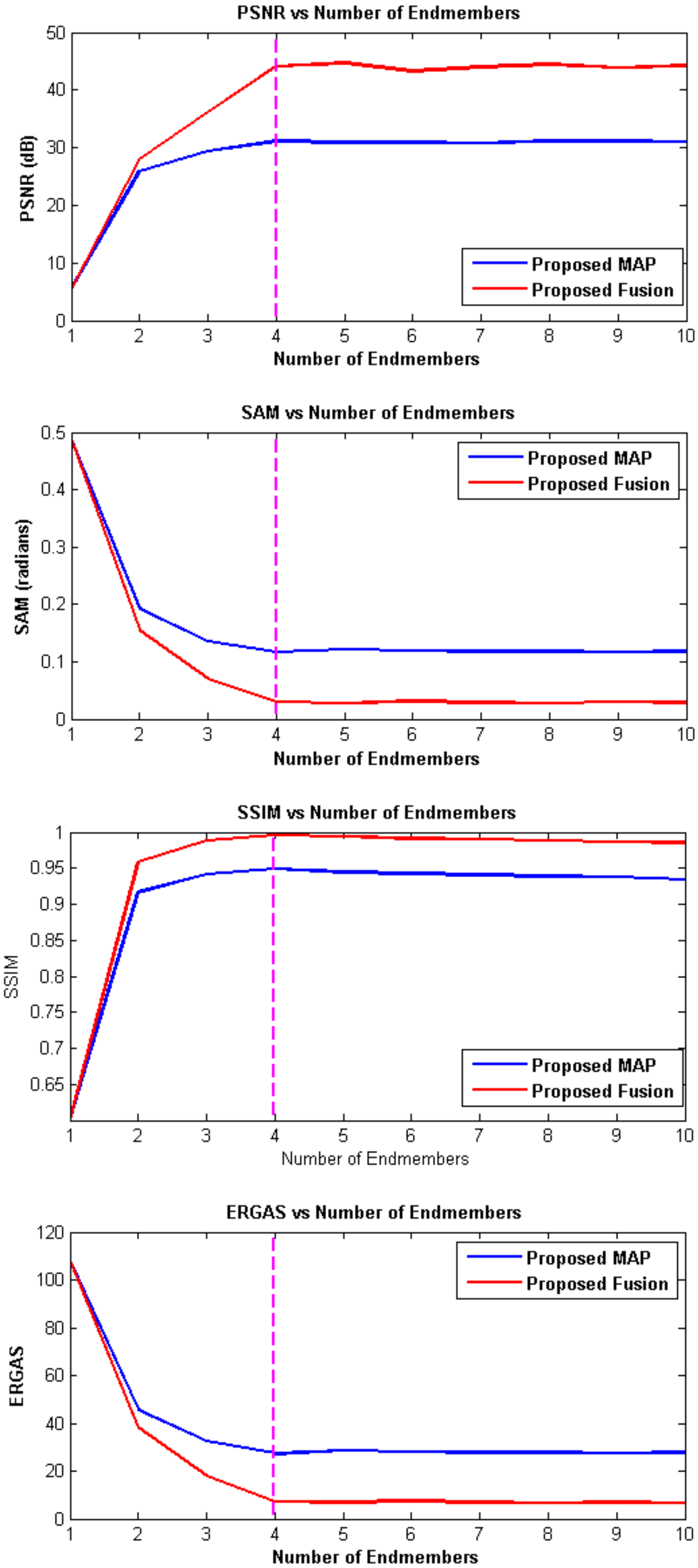

Figure 5.3: Performance of Proposed Methods for Different Number of Endmembers

5.2.4 Experimental Results on Cave Dataset

Table5.3: PSNR (dB) results for the Cave dataset

	Single Image SRR Methods				Fusion Based SRR Methods	
	Yang	Xiong	MAP	TP MAP	Lanaras	MAP Fusion
balloons	37,863	36,159	<u>39,135</u>	38,317	40,028	**46,346**
chart_and_stuffed_toy	31,483	30,904	31,439	<u>31,574</u>	34,559	**38,879**
face	33,657	39,366	38,371	<u>39,903</u>	39,855	**44,080**
fake_and_real_lemons	37,389	37,736	<u>38,979</u>	38,060	37,814	**46,507**
fake_and_real_strawberries	27,887	29,786	33,021	<u>33,840</u>	35,937	**42,558**
glass_tiles	28,360	26,720	30,037	<u>30,311</u>	34,459	**39,450**
real_and_fake_apples	<u>45,111</u>	43,558	43,853	44,353	36,792	**47,003**
real_and_fake_peppers	33,559	32,556	31,039	<u>34,747</u>	37,862	**43,055**
thread_spools	28,483	28,787	32,405	<u>33,158</u>	36,161	**41,908**
beads	29,952	26,906	30,546	<u>30,550</u>	30,896	**36,567**
clay	35,253	32,809	35,743	<u>36,321</u>	30,555	**39,811**
cloth	22,719	23,051	<u>26,958</u>	26,924	32,580	**38,635**
fake_and_real_beers	32,840	37,575	37,341	<u>39,315</u>	41,682	**42,274**
fake_and_real_lemon_slices	24,633	31,607	<u>34,536</u>	33,736	36,655	**46,179**
feathers	35,641	33,082	36,786	<u>37,945</u>	31,269	**44,589**
flowers	32,675	29,737	33,947	<u>34,159</u>	31,787	**41,411**
hairs	32,803	32,876	34,242	<u>34,428</u>	37,601	**41,833**
jelly_beans	30,916	29,309	33,401	<u>33,435</u>	34,806	**42,133**
oil_painting	24,046	27,42	<u>28,951</u>	28,877	35,705	**39,569**
paints	33,560	29,223	35,172	<u>35,687</u>	36,955	**40,283**
photo_and_face	25,316	31,652	34,484	<u>35,023</u>	43,183	**45,236**
pompoms	35,609	34,834	37,302	<u>37,736</u>	32,354	**43,347**
sponges	31,630	33,733	37,303	<u>37,451</u>	32,309	**42,142**
stuffed_toys	<u>33,604</u>	30,134	32,038	32,066	33,146	**35,615**
AVERAGES	31,874	32,063	34,459	<u>34,913</u>	35,623	**42,059**

Table5.4: SSIM results for the Cave dataset

	Single Image SRR Methods				Fusion Based SRR Methods	
	Yang	Xiong	MAP	TP MAP	Lanaras	MAP Fusion
balloons	0,947	0,825	0,966	0,905	**0,985**	0,983
chart_and_stuffed_toy	0,906	0,908	0,932	0,936	0,953	**0,970**
face	0,929	0,966	0,958	0,957	0,979	**0,981**
fake_and_real_lemons	0,953	0,966	0,972	0,916	0,984	**0,986**
fake_and_real_strawberries	0,905	0,943	0,963	0,965	0,972	**0,988**
glass_tiles	0,897	0,887	0,933	0,937	0,965	**0,984**
real_and_fake_apples	0,976	0,976	0,977	0,980	**0,986**	0,980
real_and_fake_peppers	0,937	0,956	0,824	0,963	0,968	**0,978**
thread_spools	0,915	0,920	0,930	0,947	0,970	**0,984**
beads	0,934	0,888	0,931	0,932	0,952	**0,960**
clay	0,909	0,950	0,939	0,927	**0,968**	0,964
cloth	0,822	0,772	0,870	0,880	0,944	**0,980**
fake_and_real_beers	0,897	0,967	0,959	0,970	0,972	**0,980**
fake_and_real_lemon_slices	0,894	0,950	0,953	0,911	0,979	**0,988**
feathers	0,929	0,946	0,944	0,957	0,973	**0,979**
flowers	0,908	0,892	0,938	0,933	0,961	**0,972**
hairs	0,865	0,887	0,896	0,870	**0,978**	0,969
jelly_beans	0,941	0,935	0,957	0,934	0,937	**0,985**
oil_painting	0,726	0,728	0,769	0,760	0,953	**0,964**
paints	0,922	0,934	0,960	0,966	0,962	**0,980**
photo_and_face	0,915	0,968	0,976	0,978	0,976	**0,990**
pompoms	0,912	0,927	0,942	0,946	0,973	**0,981**
sponges	0,861	0,944	0,918	0,938	**0,975**	0,956
stuffed_toys	0,923	0,936	0,952	0,956	0,972	**0,976**
AVERAGES	0,905	0,916	0,931	0,932	0,968	**0,977**

Table5.5: SAM (radians) results for the Cave dataset

	Single Image SRR Methods				Fusion Based SRR Methods	
	Yang	Xiong	MAP	TP MAP	Lanaras	MAP Fusion
balloons	0,036	0,058	0,040	0,044	0,023	**0,018**
chart_and_stuffed_toy	0,085	0,091	0,081	0,081	0,049	**0,038**
face	0,041	0,040	0,045	0,038	0,030	**0,026**
fake_and_real_lemons	0,111	0,114	0,098	0,110	0,092	**0,042**
fake_and_real_strawberries	0,161	0,201	0,139	0,132	0,104	**0,053**
glass_tiles	0,149	0,177	0,126	0,123	0,111	**0,046**
real_and_fake_apples	0,079	0,102	0,095	0,090	0,092	**0,073**
real_and_fake_peppers	0,108	0,127	0,126	0,096	0,096	**0,040**
thread_spools	0,125	0,165	0,112	0,106	0,081	**0,046**
beads	0,136	0,189	0,135	0,133	0,121	**0,076**
clay	0,057	0,071	0,055	0,053	0,053	**0,039**
cloth	0,163	0,197	0,133	0,132	0,105	**0,040**
fake_and_real_beers	0,034	0,033	0,035	0,028	**0,018**	0,021
fake_and_real_lemon_slices	0,094	0,119	0,090	0,101	0,076	**0,033**
feathers	0,060	0,077	0,054	0,048	0,056	**0,025**
flowers	0,079	0,109	0,068	0,067	0,039	**0,033**
hairs	0,060	0,062	0,054	0,056	**0,023**	0,026
jelly_beans	0,109	0,143	0,096	0,099	0,090	**0,036**
oil_painting	0,119	0,130	0,114	0,115	0,071	**0,040**
paints	0,064	0,104	0,057	0,054	0,066	**0,033**
photo_and_face	0,085	0,127	0,096	0,092	0,050	**0,038**
pompoms	0,051	0,061	0,046	0,044	0,049	**0,025**
sponges	0,040	0,047	0,032	0,031	0,024	**0,019**
stuffed_toys	0,042	0,084	0,071	0,070	0,050	**0,046**
AVERAGES	0,087	0,110	0,083	0,081	0,065	**0,038**

Table5.6: ERGAS results for the Cave dataset

	Single Image SRR Methods				Fusion Based SRR Methods	
	Yang	Xiong	MAP	TP MAP	Lanaras	MAP Fusion
balloons	11,673	14,988	10,355	11,585	9,045	**4,986**
chart_and_stuffed_toy	26,741	28,344	25,077	24,997	20,497	**13,663**
face	22,769	11,469	12,659	10,891	12,077	**7,710**
fake_and_real_lemons	44,691	47,499	38,671	43,916	50,012	**15,384**
fake_and_real_strawberries	137,32	83,218	57,493	54,789	48,495	**21,889**
glass_tiles	39,454	46,872	33,121	32,346	31,365	**13,344**
real_and_fake_apples	32,072	39,033	33,701	31,949	52,990	**25,279**
real_and_fake_peppers	47,293	56,385	53,867	42,620	51,127	**16,092**
thread_spools	60,913	57,896	37,339	35,435	32,839	**16,287**
beads	47,222	64,742	47,012	46,002	48,379	**26,065**
clay	16,736	21,122	16,191	15,372	19,599	**12,297**
cloth	60,258	53,242	35,422	35,018	31,318	**11,136**
fake_and_real_beers	12,324	7,737	8,263	6,976	7,123	**5,824**
fake_and_real_lemon_slices	109,43	36,668	27,884	31,156	27,056	**11,262**
feathers	17,597	22,970	15,741	13,954	19,337	**7,285**
flowers	24,373	33,785	20,470	20,314	21,057	**10,752**
hairs	17,715	17,346	14,992	15,354	**7,239**	7,689
jelly_beans	39,214	48,825	32,563	33,586	35,305	**12,865**
oil_painting	58,636	34,923	30,659	30,898	18,423	**12,962**
paints	21,352	34,534	18,199	17,387	28,044	**11,177**
photo_and_face	159,15	55,760	41,456	40,160	22,591	**18,201**
pompoms	15,607	17,403	13,096	12,666	15,648	**7,564**
sponges	14,830	12,698	8,509	8,585	6,521	**5,456**
stuffed_toys	14,985	23,389	20,113	19,836	14,855	**13,540**
AVERAGES	43,848	36,285	27,202	26,491	26,289	**12,863**

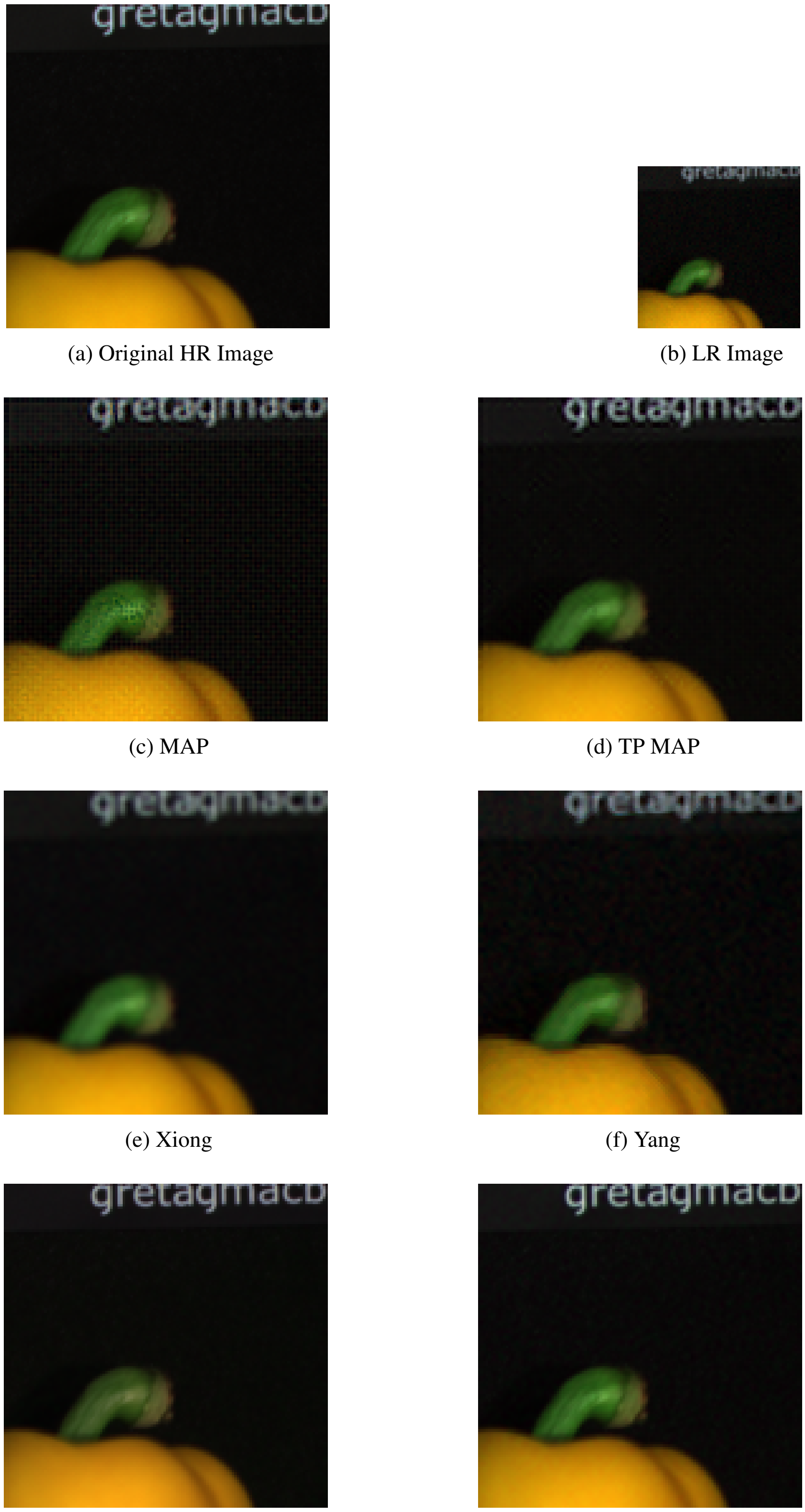

(a) Original HR Image (b) LR Image

(c) MAP (d) TP MAP

(e) Xiong (f) Yang

(g) Lanaras (h) Fusion MAP

Figure 5.4: SRR Results of Example Image Patch A from Cave Dataset

(a) Original HR Image

(b) LR Image

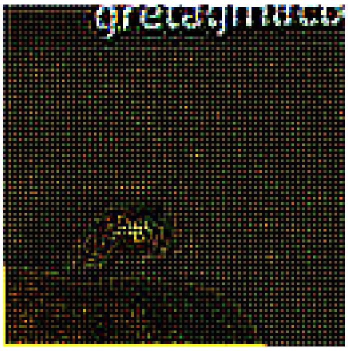

(c) MAP

(d) TP MAP

(e) Xiong

(f) Yang

(g) Lanaras

(h) Fusion MAP

Figure 5.5: High Frequency Results of Example Image Patch A from Cave Dataset

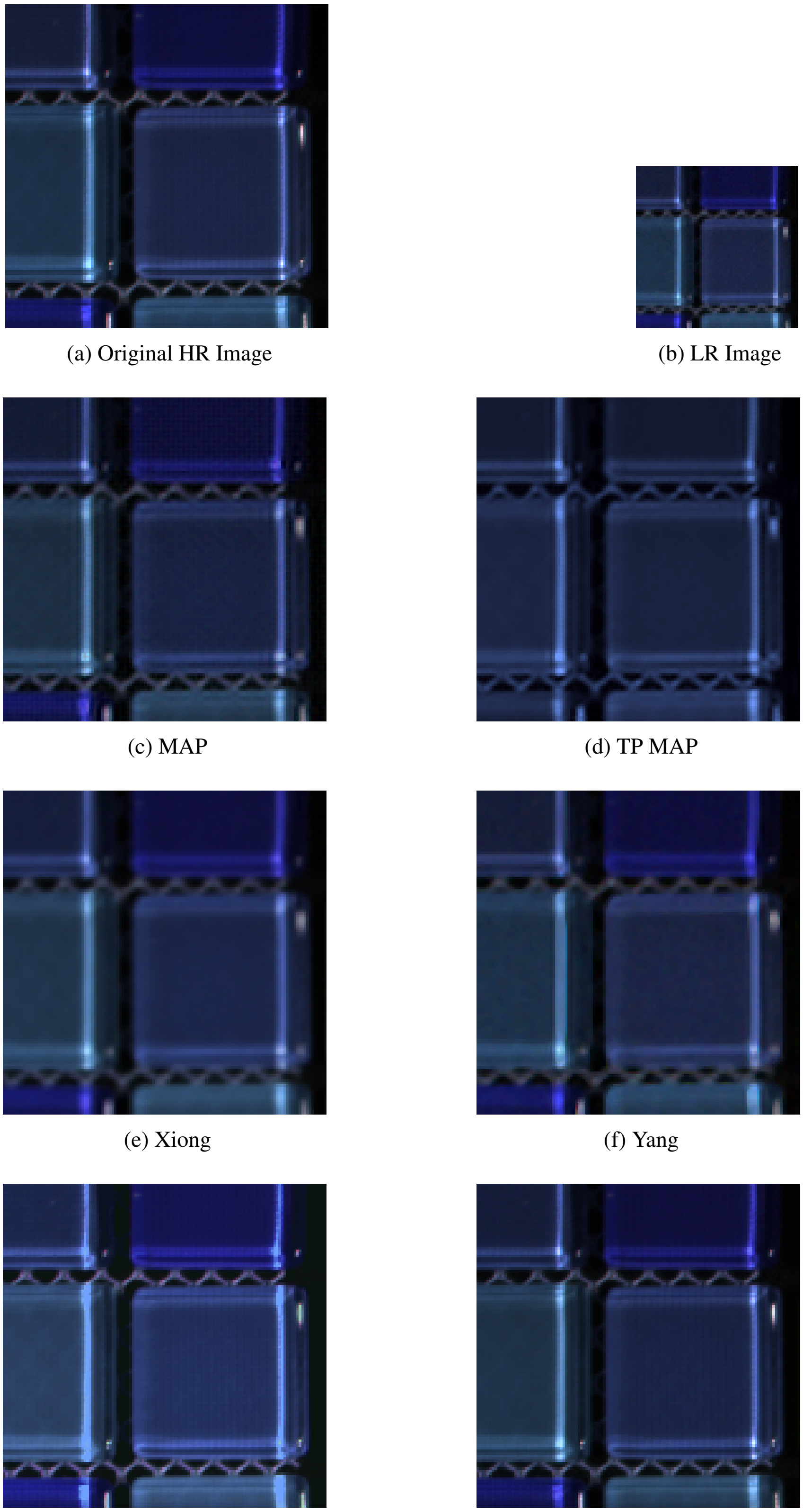

(a) Original HR Image (b) LR Image

(c) MAP (d) TP MAP

(e) Xiong (f) Yang

(g) Lanaras (h) Fusion MAP

Figure 5.6: SRR Results of Example Image Patch B from Cave Dataset

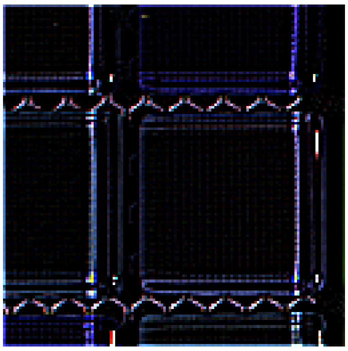

(a) Original HR Image

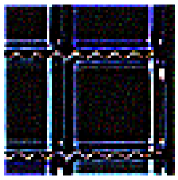

(b) LR Image

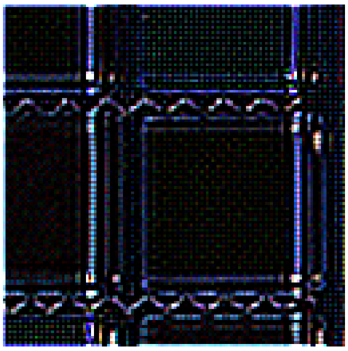

(c) MAP

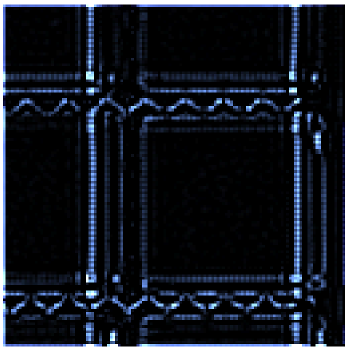

(d) TP MAP

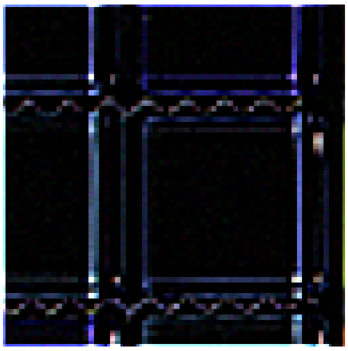

(e) Xiong

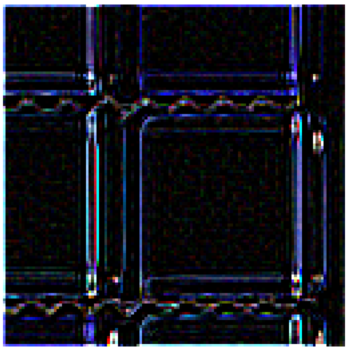

(f) Yang

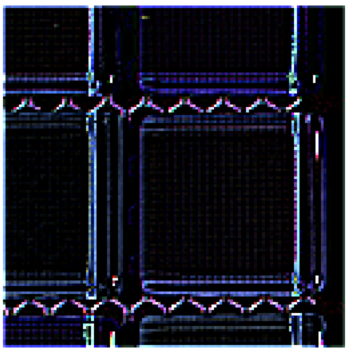

(g) Lanaras

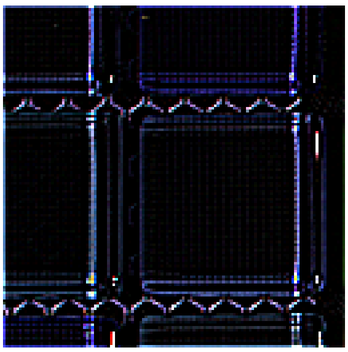

(h) Fusion MAP

Figure 5.7: High Frequency Results of Example Image Patch B from Cave Dataset

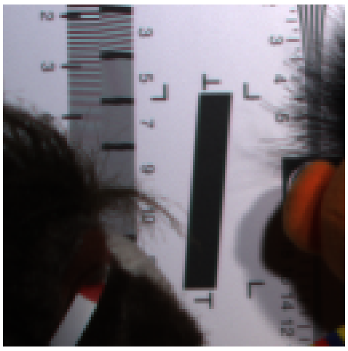

(a) Original HR Image

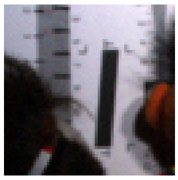

(b) LR Image

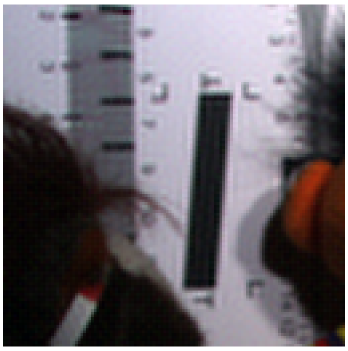

(c) MAP

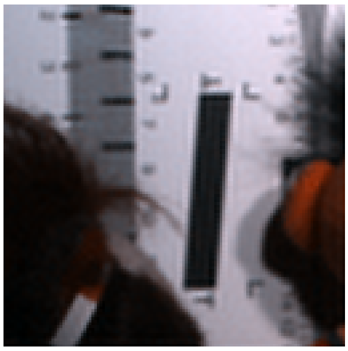

(d) TP MAP

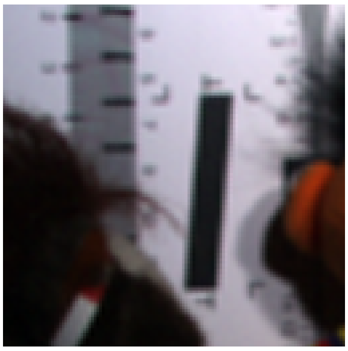

(e) Xiong

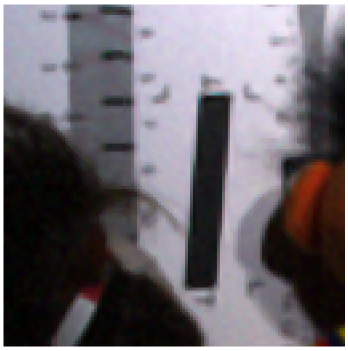

(f) Yang

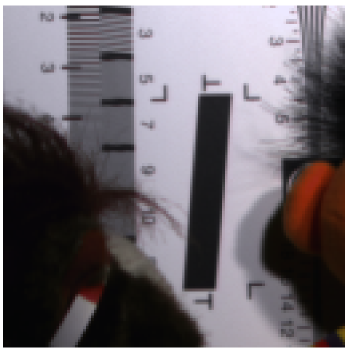

(g) Lanaras

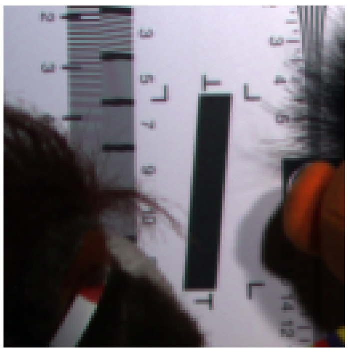

(h) Fusion MAP

Figure 5.8: SRR Results of Example Image Patch C from Cave Dataset

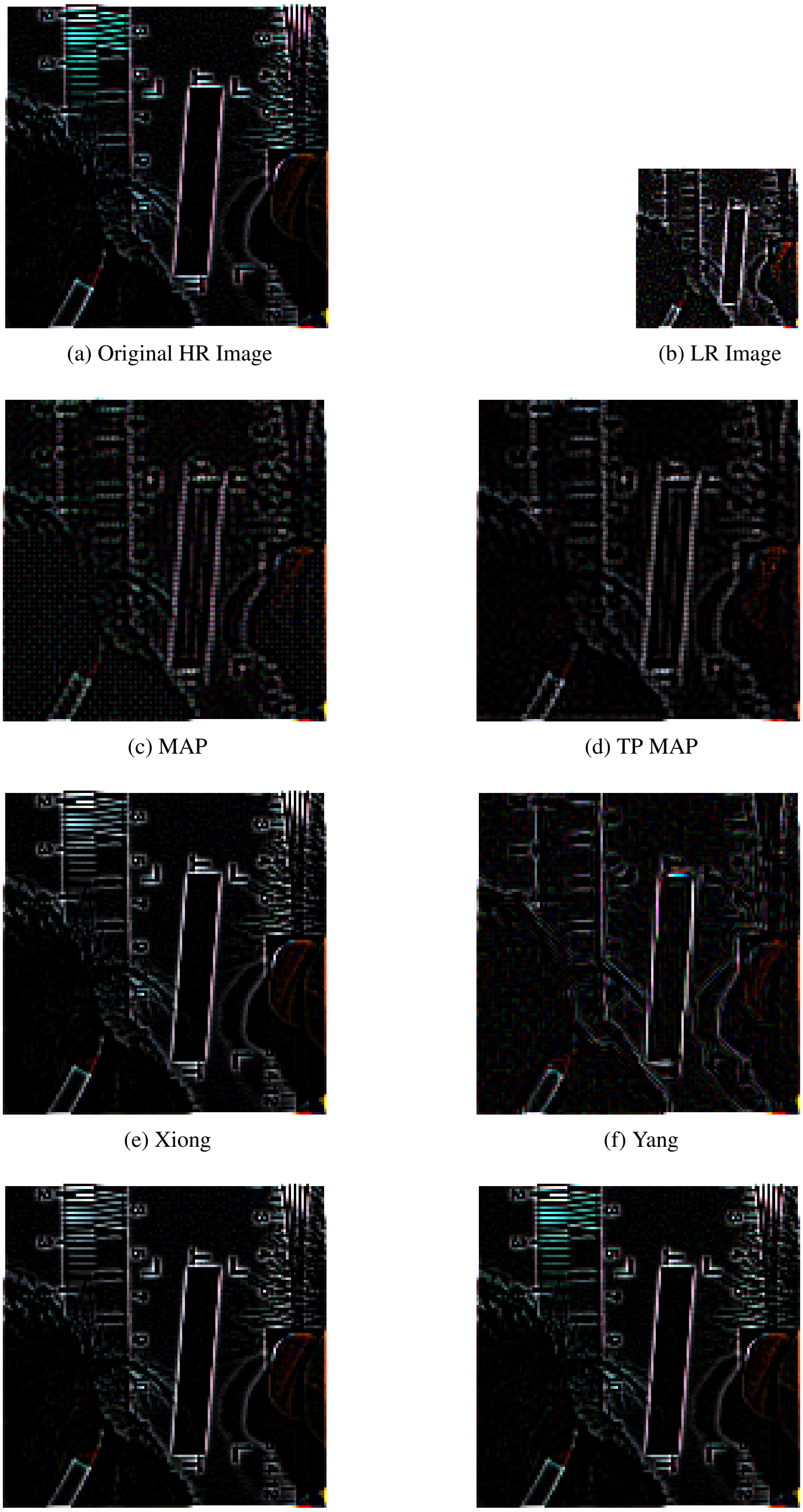

(a) Original HR Image
(b) LR Image
(c) MAP
(d) TP MAP
(e) Xiong
(f) Yang
(g) Lanaras
(h) Fusion MAP

Figure 5.9: High Frequency Results of Example Image Patch C from Cave Dataset

5.2.5 Experimental Results on Harvard Dataset

Table5.7: PSNR (dB) results for the Harvard dataset

	Single Image SRR Methods				Fusion Based SRR Methods	
	Yang	Xiong	MAP	TP MAP	Lanaras	MAP Fusion
imga2	27,548	26,371	27,650	27,457	27,428	**28,379**
imga6	31,524	31,356	32,343	32,775	30,677	**34,404**
imga7	28,276	27,594	28,884	28,945	31,036	**35,190**
imgb0	30,526	29,230	32,191	32,224	38,021	**39,962**
imgb1	30,562	29,441	32,824	32,854	36,823	**38,017**
imgb3	35,456	35,073	35,905	36,096	32,063	**37,708**
imgb5	35,307	35,342	36,683	36,553	33,349	**40,753**
imgb6	31,356	29,080	33,464	33,632	29,539	**42,308**
imgb7	34,573	31,630	32,265	33,253	30,298	**34,368**
imgb9	31,356	35,939	38,860	39,604	37,485	**42,223**
imgc7	35,129	35,939	35,104	35,388	38,728	**39,014**
imgc8	33,471	29,343	31,183	31,231	33,240	**33,446**
imgd2	34,554	33,003	35,144	35,706	**43,200**	42,986
imgd3	34,203	31,971	35,733	36,339	34,734	**40,943**
imgd7	28,386	26,669	28,939	28,909	32,054	**33,385**
imgd8	37,817	35,716	38,595	39,326	38,981	**41,709**
imgd9	30,909	32,470	32,127	31,998	31,209	**33,333**
imge7	31,458	29,509	33,428	32,951	36,312	**38,924**
imgf4	34,122	31,307	34,767	35,067	38,891	**44,310**
imgf6	25,847	25,756	26,941	27,222	27,003	**33,124**
imgf7	30,868	29,868	31,708	32,071	33,461	**38,882**
imgf8	26,547	25,912	28,532	28,648	23,658	**35,975**
imgh0	29,779	27,443	31,866	31,673	32,804	**34,306**
imgh1	35,352	33,829	37,952	37,299	35,091	**44,797**
imgh2	34,749	32,668	35,804	36,287	37,905	**39,028**
imgh3	20,698	19,294	21,601	21,846	23,382	**28,621**
averages	31,553	30,452	32,711	32,898	33,360	**37,542**

Table5.8: SSIM results for the Harvard dataset

	Single Image SRR Methods				Fusion Based SRR Methods	
	Yang	Xiong	MAP	TP MAP	Lanaras	MAP Fusion
imga2	<u>0,638</u>	0,595	0,625	0,616	0,657	**0,661**
imga6	0,757	0,771	<u>0,812</u>	0,807	0,840	**0,851**
imga7	0,738	0,753	<u>0,805</u>	0,799	0,913	**0,931**
imgb0	0,834	0,840	<u>0,892</u>	0,880	0,952	**0,954**
imgb1	0,810	0,830	<u>0,883</u>	0,878	0,933	**0,938**
imgb3	0,851	0,872	<u>0,881</u>	0,876	0,890	**0,894**
imgb5	0,877	0,922	<u>0,924</u>	0,906	0,936	**0,939**
imgb6	0,853	0,825	<u>0,918</u>	0,908	0,961	**0,973**
imgb7	0,870	0,883	0,859	<u>0,891</u>	0,893	**0,900**
imgb9	0,853	0,917	0,928	<u>0,929</u>	0,944	**0,946**
imgc7	0,854	<u>0,917</u>	0,880	0,876	**0,916**	**0,916**
imgc8	0,866	0,892	0,907	<u>0,909</u>	**0,934**	0,933
imgd2	0,911	0,933	0,942	<u>0,944</u>	**0,973**	0,972
imgd3	0,901	0,912	<u>0,926</u>	0,923	0,940	**0,942**
imgd7	0,695	0,724	<u>0,733</u>	<u>0,733</u>	**0,810**	0,800
imgd8	0,890	0,924	0,921	<u>0,925</u>	0,930	**0,932**
imgd9	0,671	<u>0,749</u>	0,734	0,729	0,750	**0,776**
imge7	0,844	0,851	<u>0,889</u>	0,860	0,929	**0,933**
imgf4	0,890	0,894	<u>0,941</u>	0,932	0,977	**0,982**
imgf6	0,753	0,758	0,781	<u>0,784</u>	0,862	**0,867**
imgf7	0,840	0,871	0,861	<u>0,886</u>	**0,924**	0,923
imgf8	0,792	0,800	<u>0,850</u>	0,848	0,881	**0,908**
imgh0	0,860	0,864	<u>0,899</u>	0,897	0,914	**0,917**
imgh1	0,932	<u>0,955</u>	<u>0,955</u>	0,949	**0,962**	**0,962**
imgh2	0,871	0,902	0,899	<u>0,903</u>	**0,915**	0,914
imgh3	0,504	0,424	<u>0,657</u>	0,629	0,846	**0,912**
averages	0,814	0,830	<u>0,858</u>	0,855	0,899	**0,907**

Table5.9: SAM (radians) results for the Harvard dataset

	Single Image SRR Methods				Fusion Based SRR Methods	
	Yang	Xiong	MAP	TP MAP	Lanaras	MAP Fusion
imga2	0,075	0,081	0,074	0,075	0,071	**0,069**
imga6	0,050	0,049	0,044	0,043	0,040	**0,037**
imga7	0,072	0,072	0,065	0,064	0,041	**0,032**
imgb0	0,091	0,102	0,077	0,077	0,039	**0,035**
imgb1	0,057	0,062	0,045	0,045	0,028	**0,027**
imgb3	0,056	0,057	0,054	0,052	0,063	**0,045**
imgb5	0,065	0,061	0,052	0,051	0,055	**0,034**
imgb6	0,122	0,146	0,097	0,097	0,082	**0,044**
imgb7	0,077	0,098	0,093	0,086	0,094	**0,077**
imgb9	0,122	0,080	0,063	0,059	0,051	**0,044**
imgc7	0,064	0,080	0,060	0,058	0,041	**0,040**
imgc8	0,077	0,106	0,091	0,090	**0,061**	0,073
imgd2	0,087	0,102	0,084	0,078	**0,036**	0,037
imgd3	0,100	0,116	0,085	0,082	0,069	**0,050**
imgd7	0,064	0,071	0,060	0,059	0,040	**0,038**
imgd8	0,062	0,070	0,053	0,050	0,048	**0,039**
imgd9	0,046	0,038	0,040	0,039	0,040	**0,035**
imge7	0,078	0,093	0,066	0,070	0,041	**0,037**
imgf4	0,103	0,134	0,092	0,089	0,058	**0,035**
imgf6	0,138	0,140	0,124	0,122	0,091	**0,074**
imgf7	0,098	0,108	0,090	0,085	0,058	**0,045**
imgf8	0,183	0,187	0,147	0,146	0,150	**0,086**
imgh0	0,058	0,071	0,046	0,046	0,040	**0,036**
imgh1	0,127	0,146	0,100	0,099	0,100	**0,052**
imgh2	0,067	0,082	0,059	0,056	0,050	**0,044**
imgh3	0,151	0,161	0,131	0,135	0,095	**0,066**
averages	0,088	0,097	0,076	0,075	0,061	**0,047**

Table5.10: ERGAS results for the Harvard dataset

	Single Image SRR Methods				Fusion Based SRR Methods	
	Yang	Xiong	MAP	TP MAP	Lanaras	MAP Fusion
imga2	16,445	17,699	16,654	16,737	16,060	**15,844**
imga6	10,368	10,089	9,337	9,165	8,682	**8,093**
imga7	14,832	14,807	13,308	13,253	9,079	**7,209**
imgb0	21,999	24,420	18,524	18,531	10,578	**9,662**
imgb1	12,604	13,693	10,162	10,177	**6,729**	6,816
imgb3	12,751	12,754	12,405	12,128	14,661	**10,958**
imgb5	19,619	17,900	15,561	15,395	17,028	**11,569**
imgb6	27,351	32,031	21,628	21,860	18,452	**11,243**
imgb7	19,024	22,942	22,451	20,741	22,423	**18,856**
imgb9	27,351	19,548	15,612	14,797	12,978	**11,749**
imgc7	16,012	18,160	14,994	14,481	11,031	**10,981**
imgc8	18,286	24,862	21,737	21,513	**15,211**	18,113
imgd2	32,186	37,826	31,097	29,166	**14,745**	15,345
imgd3	26,066	29,610	21,969	21,178	18,992	**14,057**
imgd7	14,335	15,571	13,582	13,351	10,243	**9,829**
imgd8	25,437	28,440	21,569	20,313	20,943	**16,893**
imgd9	10,628	9,720	9,585	9,364	9,763	**8,821**
imge7	18,343	21,742	15,566	16,320	10,485	**9,590**
imgf4	34,130	44,527	30,507	29,617	21,595	**12,623**
imgf6	33,479	33,872	30,257	29,838	23,024	**19,856**
imgf7	28,226	30,938	25,868	24,614	17,281	**14,168**
imgf8	43,695	43,842	34,510	34,335	35,782	**22,001**
imgh0	12,516	15,178	10,383	10,325	9,472	**8,856**
imgh1	43,224	51,210	34,331	34,216	35,517	**19,234**
imgh2	20,490	25,897	18,205	17,454	16,009	**14,176**
imgh3	31,200	33,456	27,228	27,994	20,213	**15,366**
averages	22,715	25,028	19,886	19,494	16,422	**13,150**

(a) Original HR Image

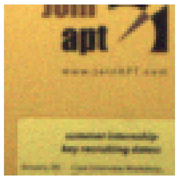

(b) LR Image

(c) MAP

(d) TP MAP

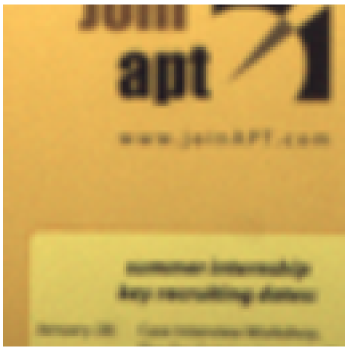

(e) Xiong

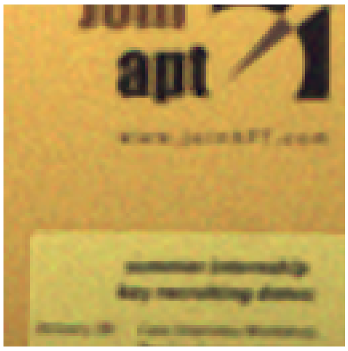

(f) Yang

(g) Lanaras

(h) Fusion MAP

Figure 5.10: SRR Results of Example Image Patch A from Harvard Dataset

(a) Original HR Image (b) LR Image

(c) MAP (d) TP MAP

(e) Xiong (f) Yang

(g) Lanaras (h) Fusion MAP

Figure 5.11: High Frequency Results of Example Image Patch A from Harvard Dataset

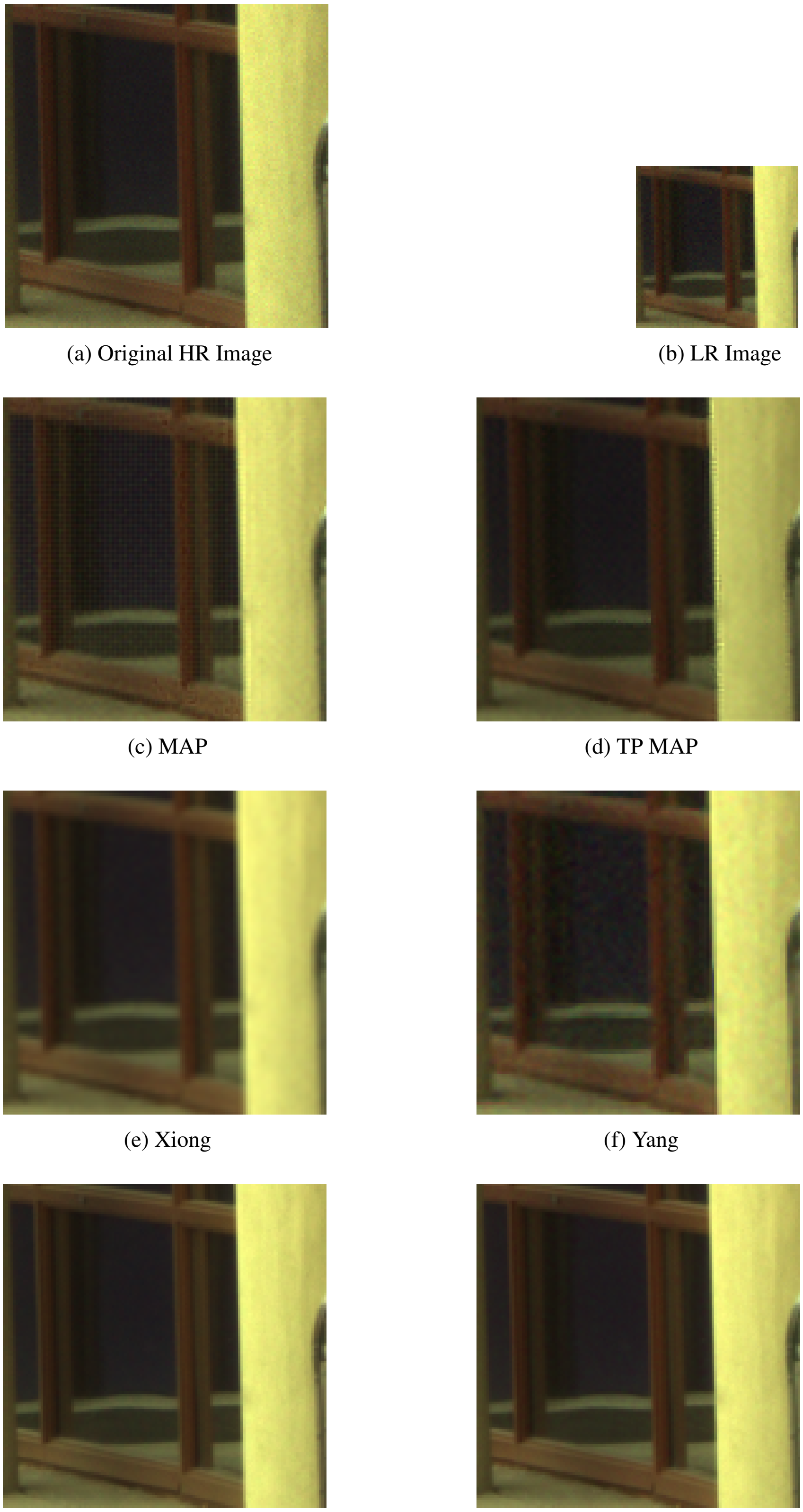

(a) Original HR Image
(b) LR Image
(c) MAP
(d) TP MAP
(e) Xiong
(f) Yang
(g) Lanaras
(h) Fusion MAP

Figure 5.12: SRR Results of Example Image Patch B from Harvard Dataset

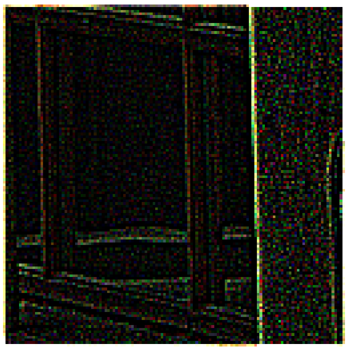

(a) Original HR Image

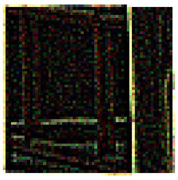

(b) LR Image

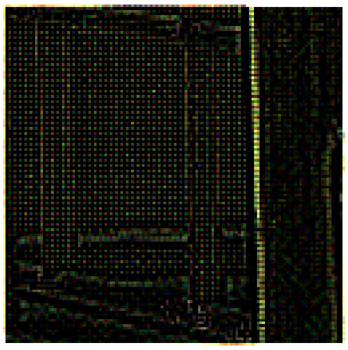

(c) MAP

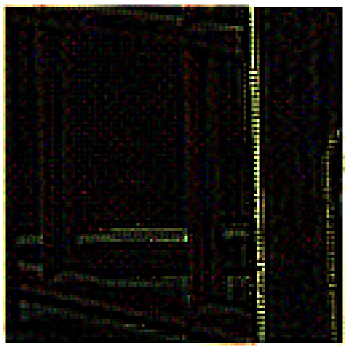

(d) TP MAP

(e) Xiong

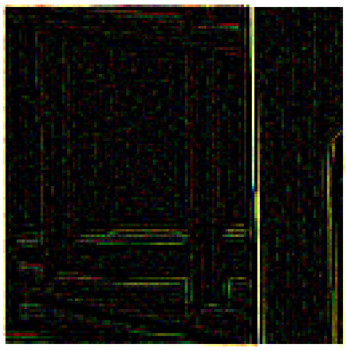

(f) Yang

(g) Lanaras

(h) Fusion MAP

Figure 5.13: High Frequency Results of Example Image Patch B from Harvard Dataset

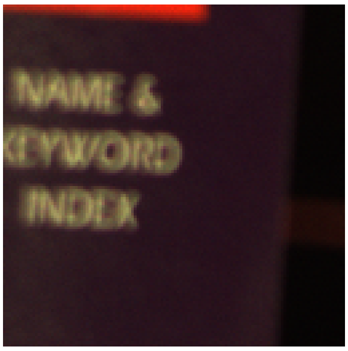

(a) Original HR Image

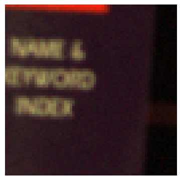

(b) LR Image

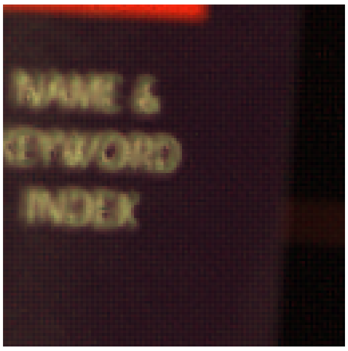

(c) MAP

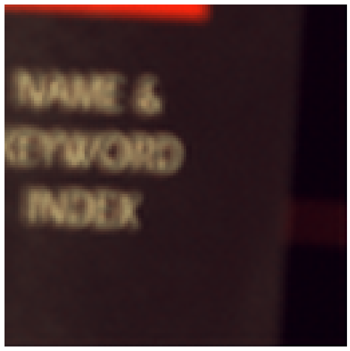

(d) TP MAP

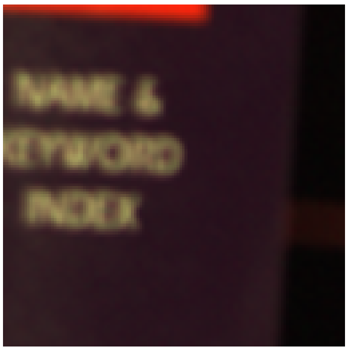

(e) Xiong

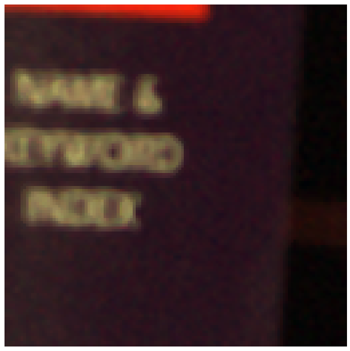

(f) Yang

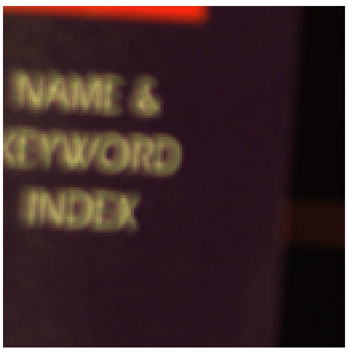

(g) Lanaras

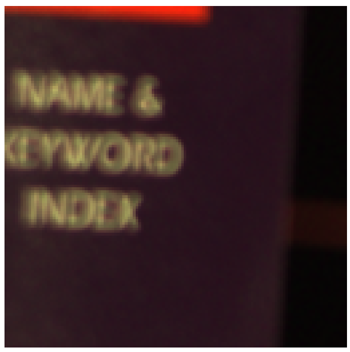

(h) Fusion MAP

Figure 5.14: SRR Results of Example Image Patch C from Harvard Dataset

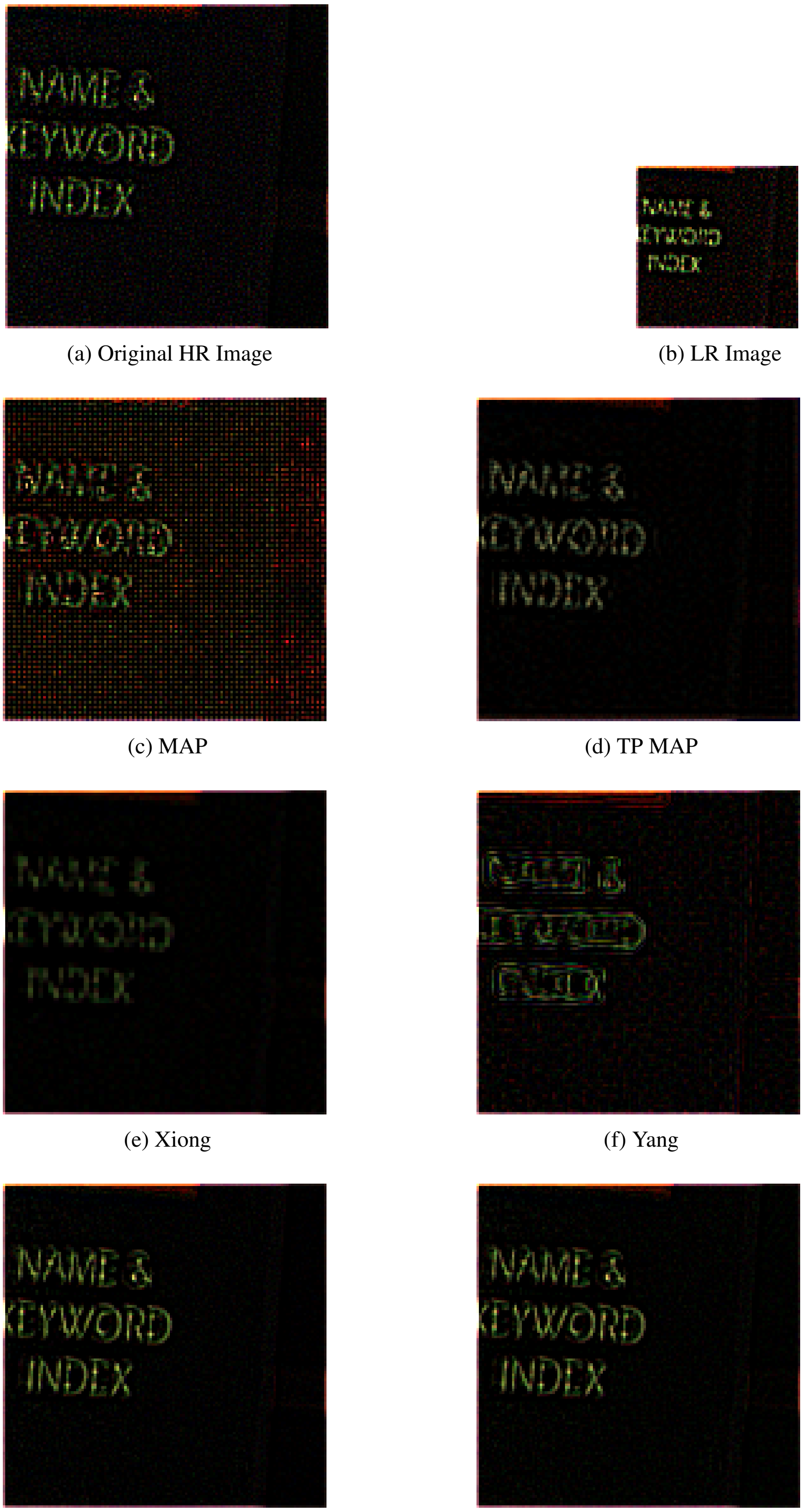

(a) Original HR Image (b) LR Image

(c) MAP (d) TP MAP

(e) Xiong (f) Yang

(g) Lanaras (h) Fusion MAP

Figure 5.15: High Frequency Results of Example Image Patch C from Harvard Dataset

5.2.6 Experimental Results on HRSS Dataset

Table5.11: PSNR (dB) results for the HRSS dataset

	Single Image SRR Methods				Fusion Based SRR Methods	
	Yang	Xiong	MAP	TP MAP	Lanaras	MAP Fusion
botswana	28,494	29,110	30,833	30,887	33,496	**36,268**
indian_pines_corrected	29,634	29,284	29,940	29,868	**30,935**	30,296
pavia	28,560	26,097	29,376	29,631	22,753	**34,221**
paviaU	29,296	26,372	30,537	30,886	25,448	**35,039**
salinas_corrected	28,930	28,891	31,189	31,171	22,185	**34,472**
averages	28,983	27,951	30,375	30,489	26,963	**34,059**

Table5.12: SSIM results for the HRSS dataset

	Single Image SRR Methods				Fusion Based SRR Methods	
	Yang	Xiong	MAP	TP MAP	Lanaras	MAP Fusion
botswana	0,696	0,752	0,820	0,823	0,880	**0,905**
indian_pines_corrected	0,719	0,807	0,837	0,836	0,822	**0,844**
pavia	0,868	0,827	0,904	0,909	0,859	**0,941**
paviaU	0,875	0,841	0,912	0,915	0,857	**0,943**
salinas_corrected	0,775	0,874	0,908	0,901	0,753	**0,929**
averages	0,786	0,820	0,876	0,877	0,834	**0,912**

Table5.13: SAM (radians) results for the HRSS dataset

	Single Image SRR Methods				Fusion Based SRR Methods	
	Yang	Xiong	MAP	TP MAP	Lanaras	MAP Fusion
botswana	0,076	0,068	0,059	0,058	0,056	**0,045**
indian_pines_corrected	0,045	0,047	0,045	0,045	**0,044**	0,045
pavia	0,156	0,191	0,138	0,135	0,181	**0,096**
paviaU	0,128	0,164	0,112	0,110	0,146	**0,074**
salinas_corrected	0,109	0,082	0,068	0,069	0,155	**0,055**
averages	0,103	0,110	0,085	0,083	0,116	**0,063**

Table5.14: ERGAS results for the HRSS dataset

	Single Image SRR Methods				Fusion Based SRR Methods	
	Yang	Xiong	MAP	TP MAP	Lanaras	MAP Fusion
botswana	17,472	14,989	13,063	16,926	13,274	**10,881**
indian_pines_corrected	9,554	10,493	9,959	9,992	**9,762**	9,773
pavia	38,054	46,479	34,149	36,934	44,698	**24,189**
paviaU	30,989	39,846	27,547	30,514	34,966	**18,136**
salinas_corrected	52,910	23,421	21,496	21,510	39,843	**20,034**
averages	29,796	27,046	21,243	23,175	28,509	**16,603**

5.3 Spectral Consistency Results

Spectral consistency is another important issue in SRR of HS images. Especially for the fusion based methods, in general, visual results are satisfactory since HR RGB image gives the textures and edges. However, the performance of these methods sharply decreases beyond the visible spectrum since auxiliary image does not give information from these bands. Therefore, spectral consistency is a significant metric for SRR of HS images. For each dataset, two images are selected having the best metric results for MAP and Lanaras. In the selected figures, the spectral characteristics of an average of 8-neighbourhood pixels of the center pixel is calculated and given in Tables 5.15- 5.16- 5.17. In order to see the effect of the band on spectral consistency, spectral reflectance characteristics of selected figures from HRSS dataset will be also given in Figure 5.22 and 5.23. Related figures from Cave and Harvard dataset are not given since these datasets have fewer bands and the spectrum of the methods are almost overlapped, interpretable figures are difficult to obtain. In Figure 5.22 and 5.23, it is clearly seen that Lanaras method gives inconsistent results beyond the visible spectrum. Actually, a fusion based SRR method may have problems with the non-overlapped bands of the HR auxiliary image. Therefore, for the fusion based SRR methods, a fair comparison should be done using the HS images which are extending the visible spectrum such as remote sensing images having hundreds of bands.

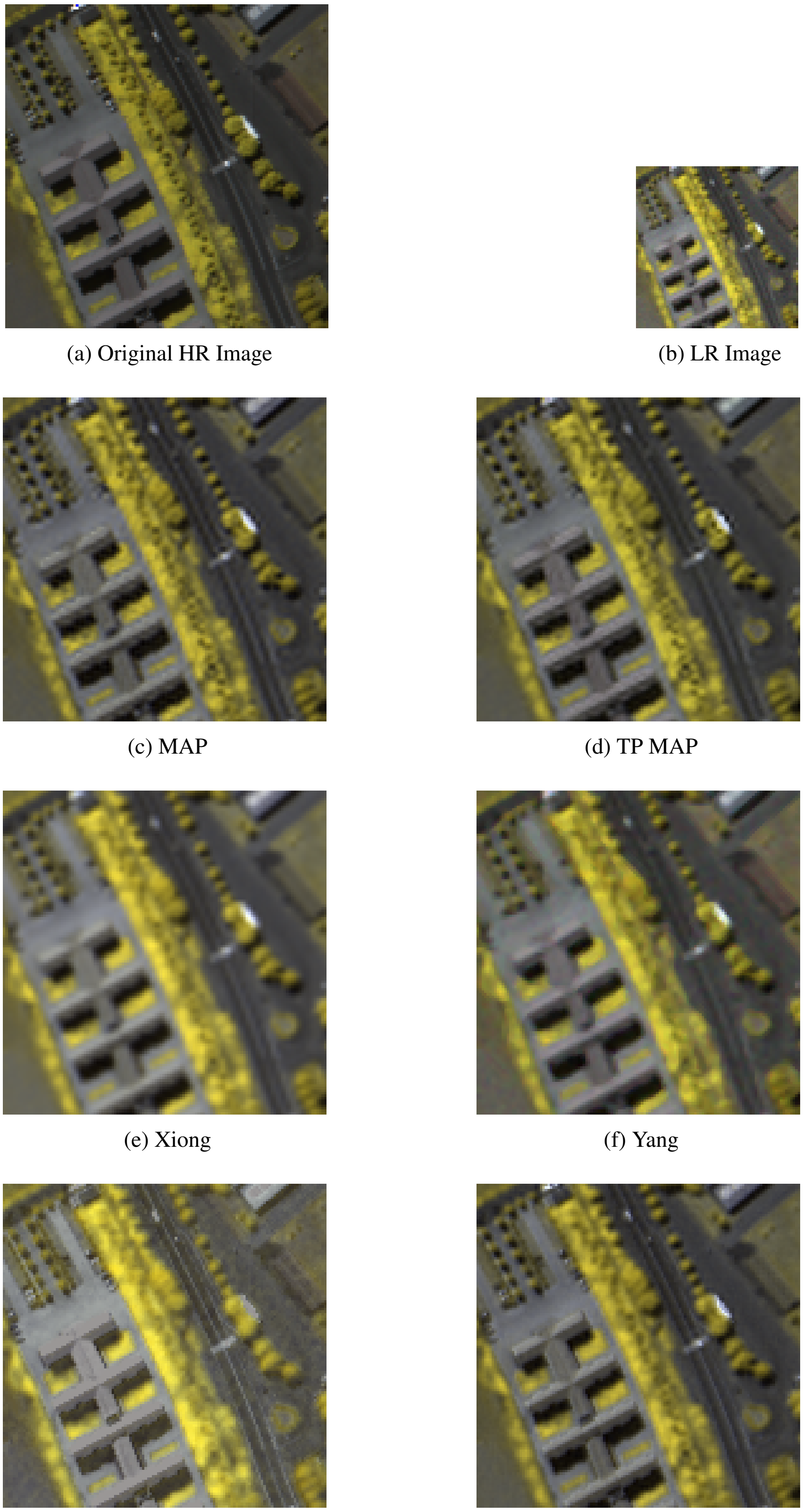

(a) Original HR Image
(b) LR Image
(c) MAP
(d) TP MAP
(e) Xiong
(f) Yang
(g) Lanaras
(h) Fusion MAP

Figure 5.16: SRR Results of Example Image Patch A from HRSS Dataset

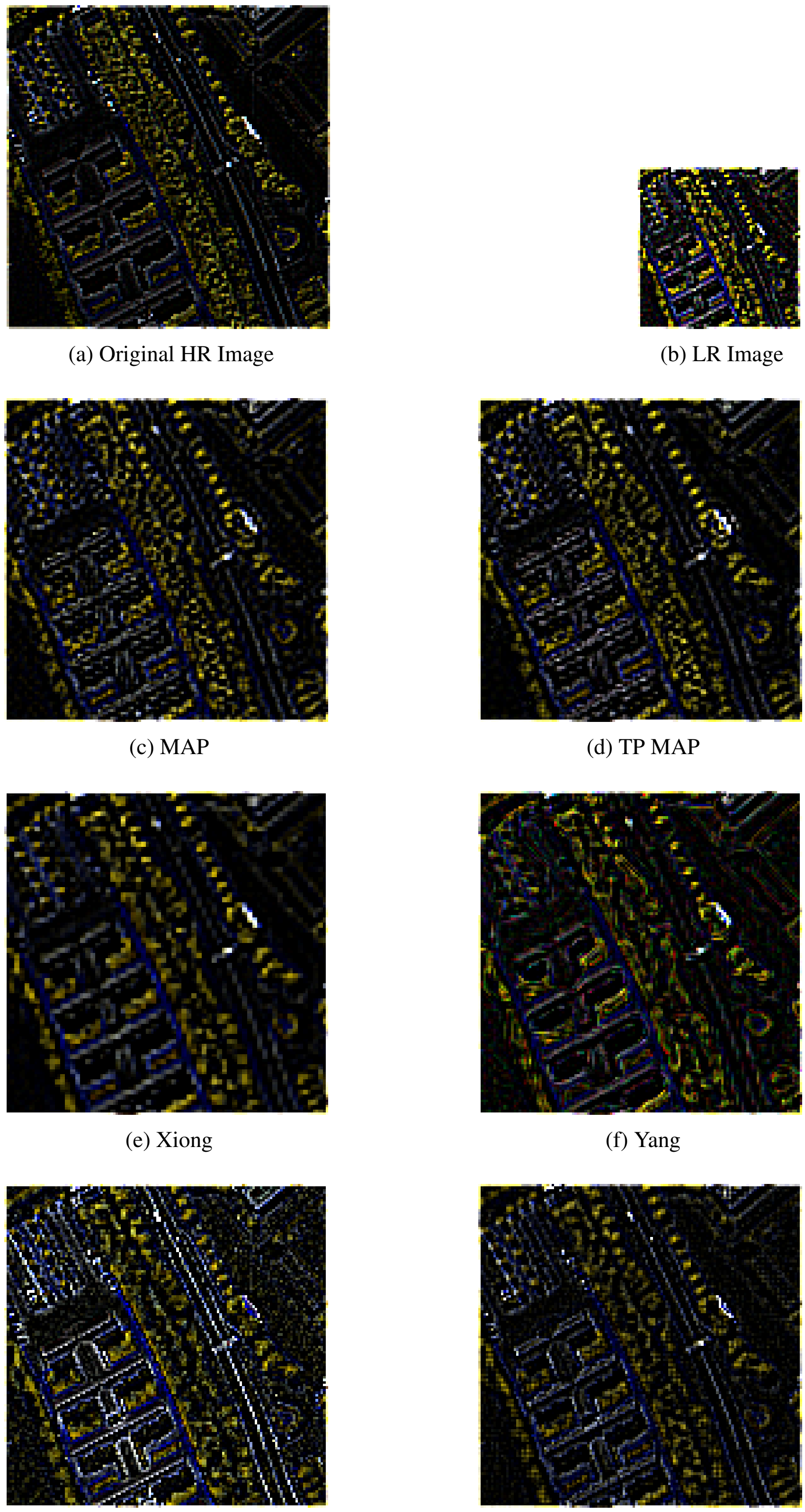

(a) Original HR Image

(b) LR Image

(c) MAP

(d) TP MAP

(e) Xiong

(f) Yang

(g) Lanaras

(h) Fusion MAP

Figure 5.17: High Frequency Results of Example Image Patch A from HRSS Dataset

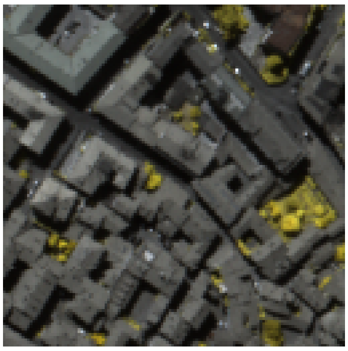

(a) Original HR Image

(b) LR Image

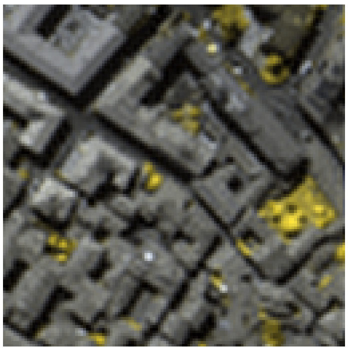

(c) MAP

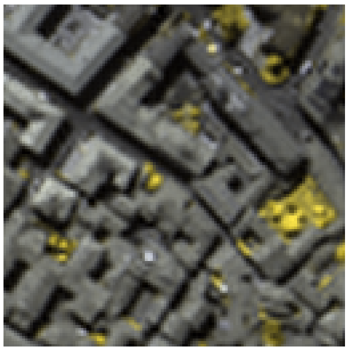

(d) TP MAP

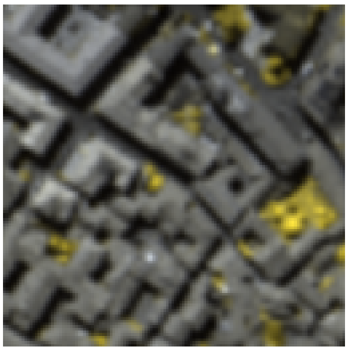

(e) Xiong

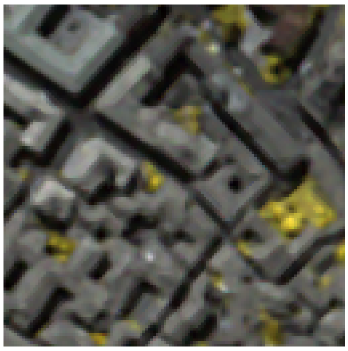

(f) Yang

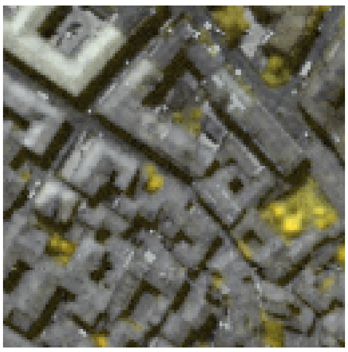

(g) Lanaras

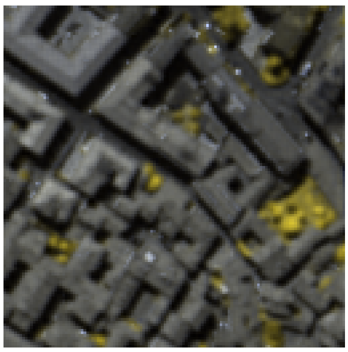

(h) Fusion MAP

Figure 5.18: SRR Results of Example Image Patch B from HRSS Dataset

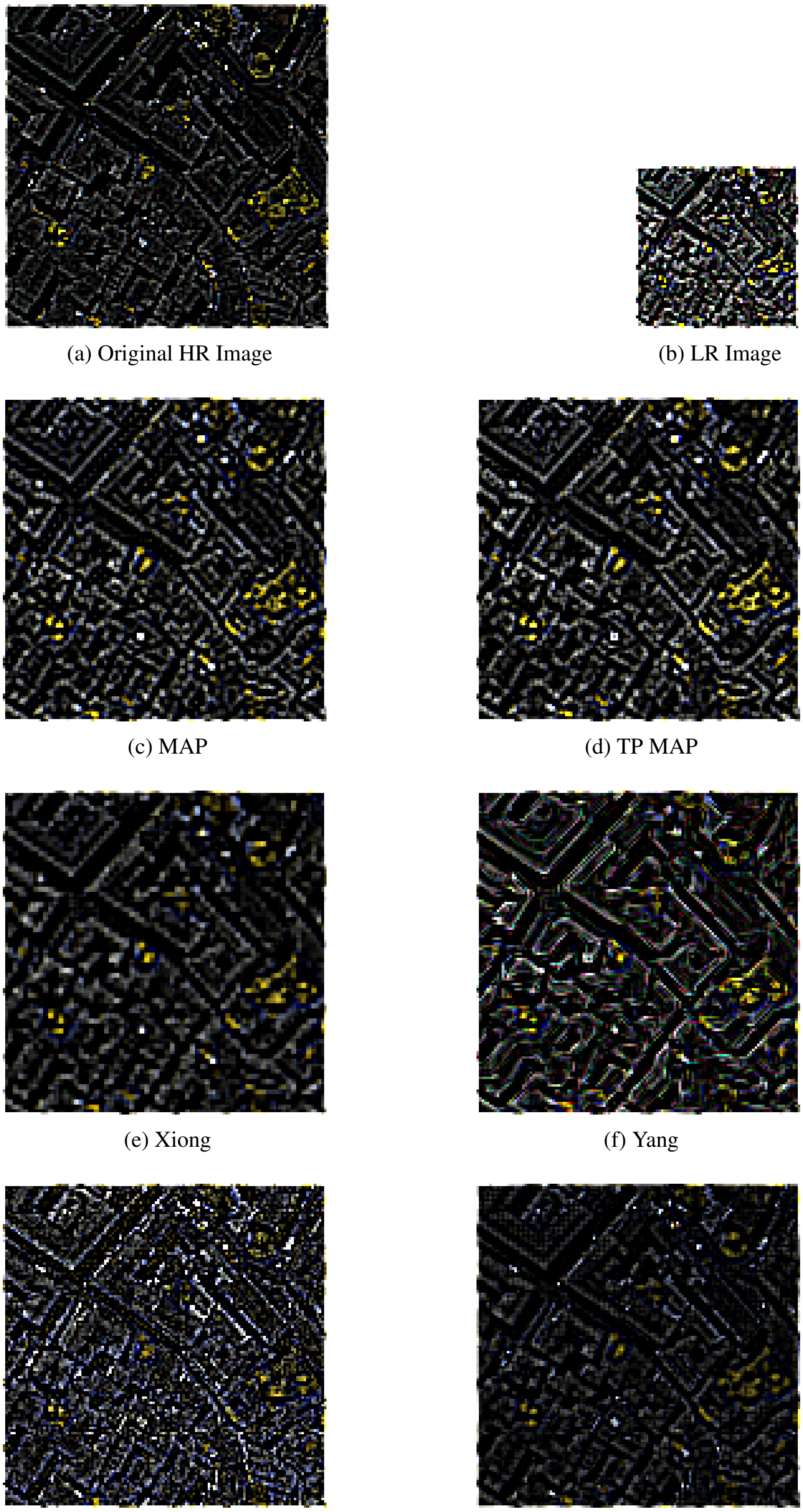

(a) Original HR Image

(b) LR Image

(c) MAP

(d) TP MAP

(e) Xiong

(f) Yang

(g) Lanaras

(h) Fusion MAP

Figure 5.19: High Frequency Results of Example Image Patch B from HRSS Dataset

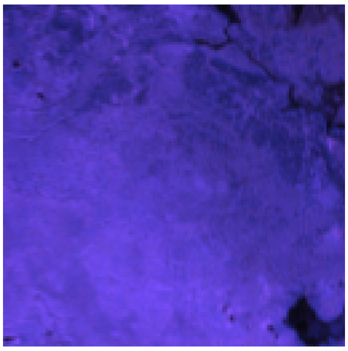

(a) Original HR Image

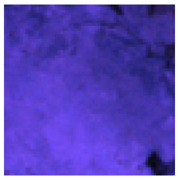

(b) LR Image

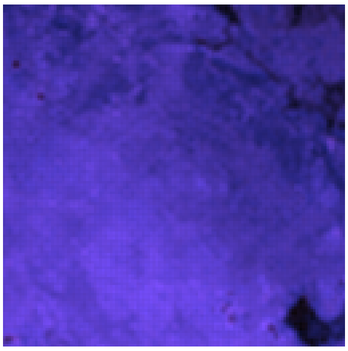

(c) MAP

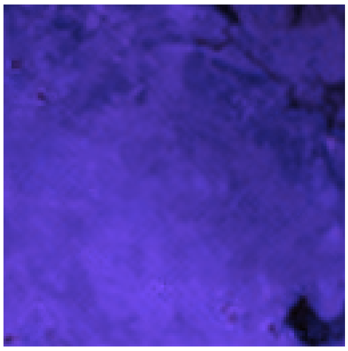

(d) TP MAP

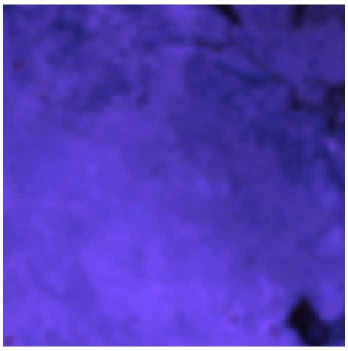

(e) Xiong

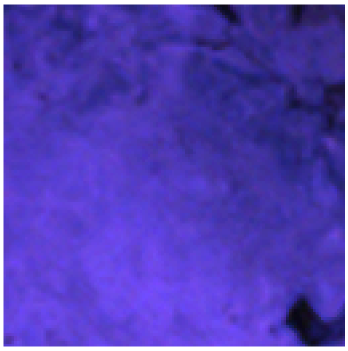

(f) Yang

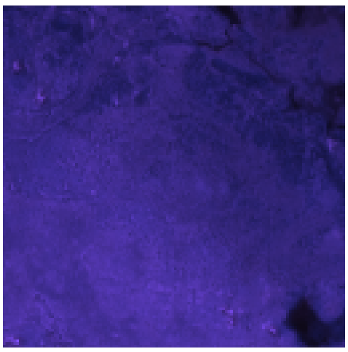

(g) Lanaras

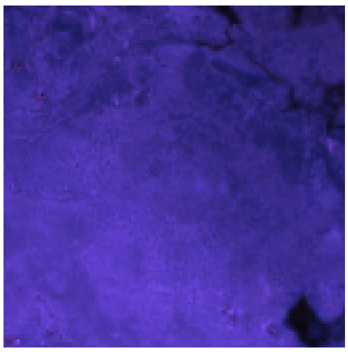

(h) Fusion MAP

Figure 5.20: SRR Results of Example Image Patch C from HRSS Dataset

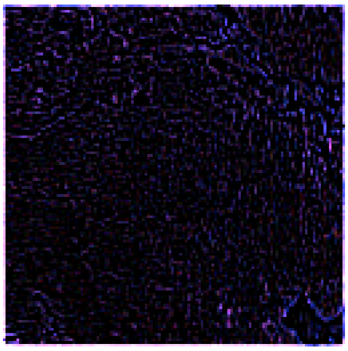

(a) Original HR Image

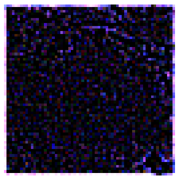

(b) LR Image

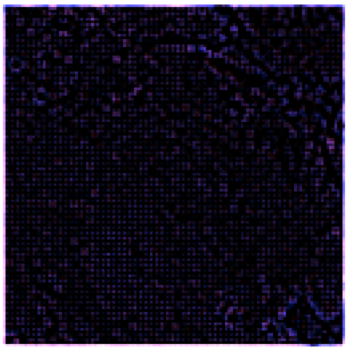

(c) MAP

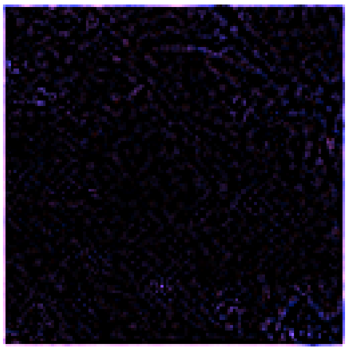

(d) TP MAP

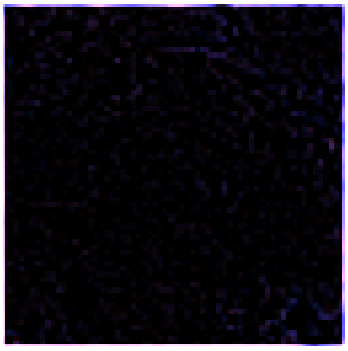

(e) Xiong

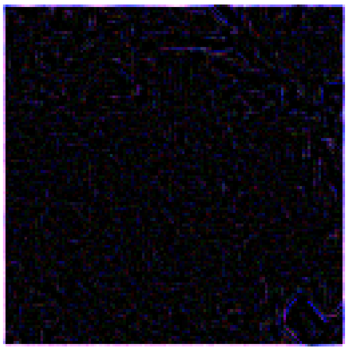

(f) Yang

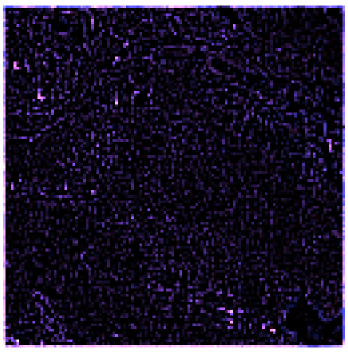

(g) Lanaras

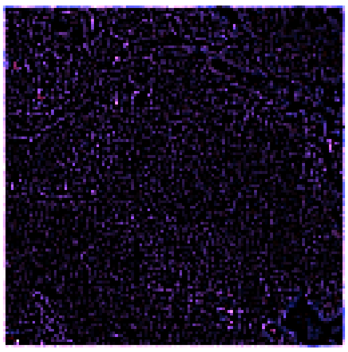

(h) Fusion MAP

Figure 5.21: High Frequency Results of Example Image Patch C from HRSS Dataset

Table5.15: Correlation in spectral reflectance (%) between ground truth and SRR methods for Cave dataset

	Yang	Xiong	MAP	TP MAP	Lanaras	MAP Fusion
Cave-glass_tiles	91.55	84.20	87.52	88.09	80.50	**91.93**
Cave-hairs	99.88	99.96	**99.97**	**99.97**	99.95	**99.97**

Table5.16: Correlation in spectral reflectance (%) between ground truth and SRR methods for Harvard dataset

	Yang	Xiong	MAP	TP MAP	Lanaras	MAP Fusion
Harvard-img_d3	99.46	**99.88**	99.87	**99.88**	99.61	99.86
Harvard-img_d2	99.39	99.77	99.82	99.78	99.77	**99.88**

Table5.17: Correlation in spectral reflectance (%) between ground truth and SRR methods for HRSS dataset

	Yang	Xiong	MAP	TP MAP	Lanaras	MAP Fusion
HRSS-salinas_corrected	99.93	99.98	99.98	99.97	96.33	**99.99**
HRSS-botswana	99.87	**99.90**	99.89	99.84	99.63	**99.90**

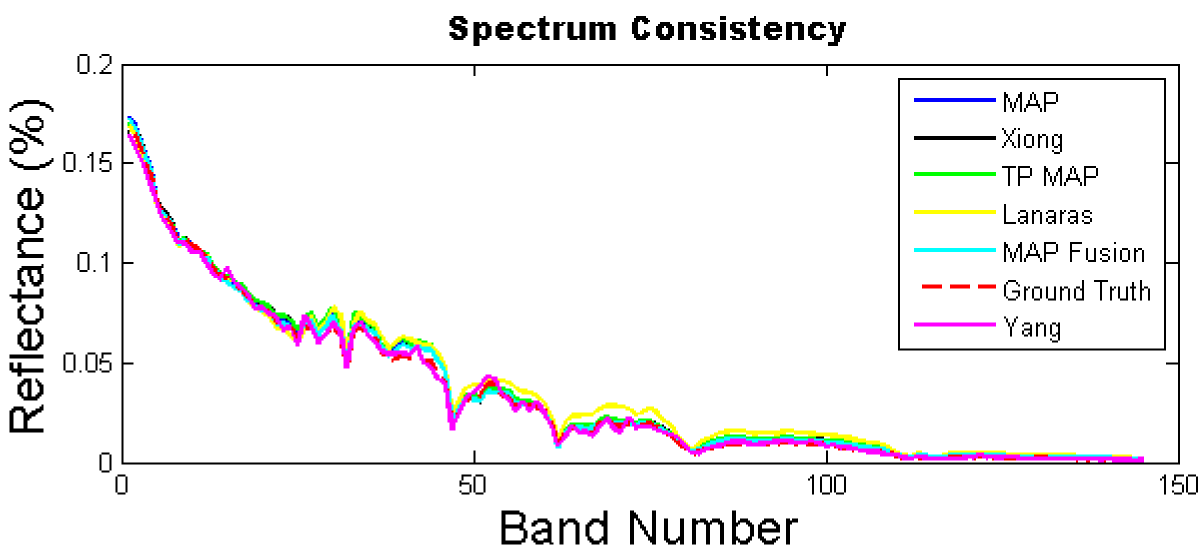

Figure 5.22: Spectral reflectance characteristics of HRSS-botswana image

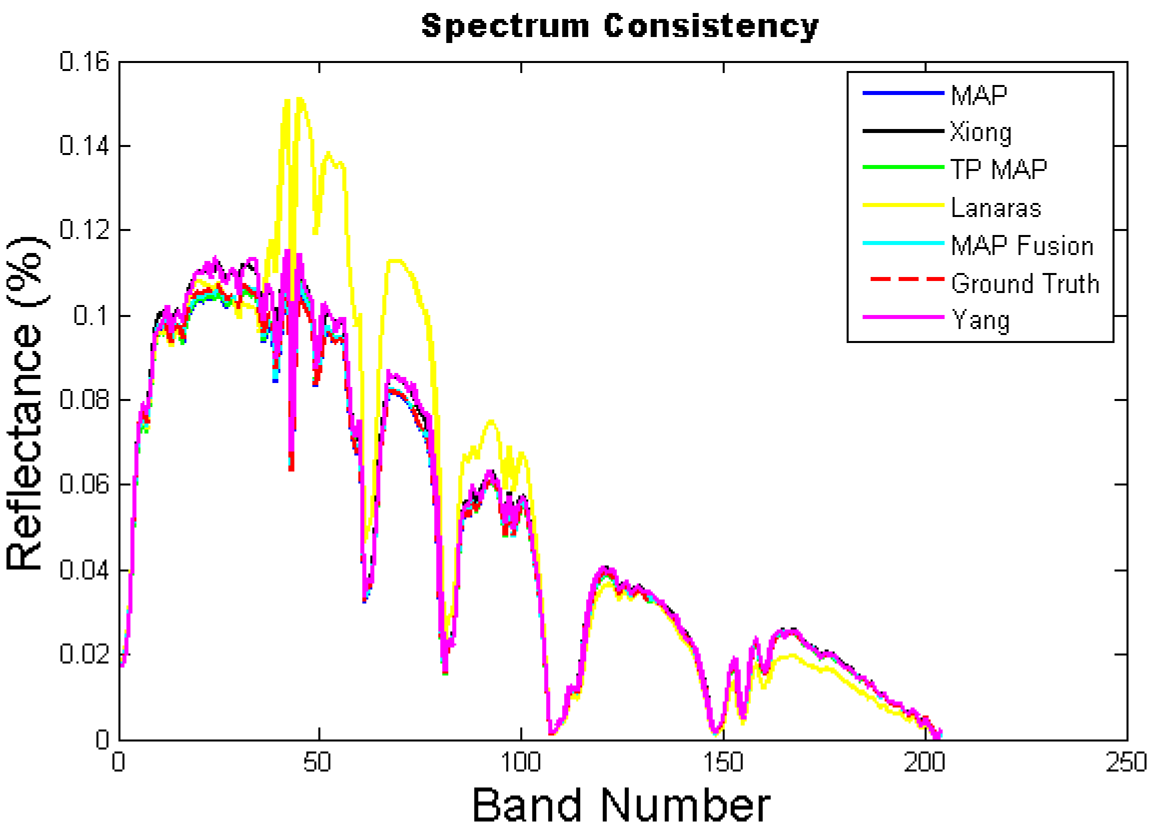

Figure 5.23: Spectral reflectance characteristics of HRSS-salinas_corrected image

5.4 Discussion

Firstly, upon observing the results, in all datasets, proposed MAP based approaches outperform the Yang and Xiong method in all metrics. Moreover, when compared with the Lanaras method, proposed MAP based approach outperforms the Lanaras method on all metrics in the HRSS dataset despite the fact that Lanaras method uses an HR RGB image with LR HS image. This is due to the fact that there are only 31 bands in the Cave and Harvard datasets as opposed to the more than 100 bands in the HRSS dataset. Therefore, for the cases where the number of spectral bands are low, the HR RGB gives reasonably high information in the fusion based methods. On the other hand, when the number of spectral bands increase, the effect of the extra information provided by the RGB image is not as substantial; and the performance of the fusion based method degrades. This is particularly critical in remote sensing applications where HS image consists of hundreds of bands.

Secondly, proposed MAP based fusion has the best performance in all datasets. The advantage of the method can be seen interpreting the Cave, Harvard and HRSS datasets together. MAP based methods have limited performance since single HS image is not enough to recover HR HS image. On the other hand, fusion based methods have excellent performance in the overlapping bands with auxiliary image. In fact, non-overlapping bands show the real performance of the fusion based methods and the performance sharply decreases in these bands. This is the reason why Lanaras method has lower performance in HRSS dataset. On the contrary, MAP based fusion approach gives an optimal solution to the SRR problem for HS images with merging MAP framework with fusion. From the conducted experiments, it is clearly seen that MAP based fusion method has better performance in all datasets. In almost all the HS images of each dataset, proposed MAP fusion method beat the other methods. Lanaras beats the proposed MAP based fusion in few images having sharp textures and edges extremely violating the smoothness constraint.

Thirdly, SRR methods should keep the spectrum consistency as much as possible while enhancing the spatial resolution of HS images. In terms of spectrum consistency, proposed MAP approach and proposed MAP based fusion approach have better results as compared to Lanaras method. The figures show that Lanaras has problems beyond the visible band and this approach highly degrades the spectrum consistency. Metric results also show the poor correlation of spectrum of HR HS image with the original HS image in this method. When comparing other methods between each other in terms of spectrum consistency, our proposed methods have slightly better results than the Yang and Xiong method.

Lastly, computation time is also important. Our current implementations have not been optimised for speed and computation times depend on the image size and number of endmembers. For a 256×256 image, typically, it takes ≈ 8 minutes for MAP and MAP based fusion methods. Texture preserving nearly doubles the computation times of the MAP method. On the other hand, processing time of Yang method directly depends on the number of spectral bands and has ≈ 1 minute for Cave and Harvard datasets and ≈ 7 minutes for the HRSS dataset. Xiong method has ≈ 1 minute and Lanaras method has ≈ 4 minutes depending on the number of iterations and convergence parameters.

CHAPTER 6

SUMMARY AND CONCLUSION

6.1 Summary

Chapter 2 presents a general information about HS imaging. Moreover, spectral unmixing concept, process of finding materials and their fractions in the HS image, is introduced in this chapter. Spectral unmixing consists of three stages, namely, determination of number of endmembers, estimation of their signatures and extracting the abundance maps. A survey on these methods are given in detail.

In Chapter 3, a survey on SRR for both natural and HS images are introduced. HS SRR is roughly divided into two groups: single image based and fusion based methods. Single image SRR methods increase the resolution of HS images without using any other source of information whereas fusion based methods fuse LR HS image with HR auxiliary image in order to obtain HR HS image.

In Chapter 4, two SRR methods from different perspectives for HS images are proposed. First method is a novel MAP based SRR method for HS images when there is no any other source of information. The idea of the proposed approach is that instead of using the spectral images, the correlation of neighbouring pixels in terms of abundances of the endmembers in the scene are used in the SRR process. Moreover, ill-posed inversion problem of SRR is further regularized with constraints specific to abundance maps results in more stable solutions. Another advantage of using the abundances in SRR process is obtaining spectrally more consistent results in HR HS images. In this approach, first, hyperspectral data is unmixed and abundances of the endmembers are found. Then, using the LR abundance maps as the basic DC, an energy function is defined using an SC from a priori information with a UC and a BC for the abundance maps. Energy function is converted to a quadratic optimization problem and jointly minimized using QP techniques. Moreover, in order to preserve textures, a post processing is applied to the HR abundance maps. After finding the HR abundance maps, HR HS image is constructing using these maps and corresponding material spectrum.

Second proposed approach utilizes the same concept when an auxiliary HR image is available with LR HS image. Similarly, fusion problem is converted to a quadratic optimization problem in abundance map domain. Moreover, it is regularized with a MAP framework. Solving the quadratic MAP based fusion problem, HR abundance maps are found and used for the reconstruction HR HS image.

Chapter 5 gives the experimental results. Experiments are conducted on three real hyperspectral datasets and compared to three other state-of-the-art SRR methods. The results show that the proposed algorithms produce better results in all quantitative metrics as compared to its competitors. In addition, upon observing the individual pixels for spectral consistency, the proposed methods are closest to the ground truth in the experiments.

6.2 Conclusion

In this thesis, two different approaches are studied for the SRR of HS images. First method can be used for SRR of single HS image when there is no auxiliary information such as a coinciding HR image. This method shows that using abundance maps gives robust and effective solutions to the SRR of HS images as compared to single band SRR methods. Since single band SRR methods do not use the band to band correlation of HS images, they have poorer performance as compared to methods that use inherent intra band informations. Moreover, using joint energy minimization with the quadratic programming significantly increases the performance as compared the regularization based single image HS SRR methods. However, unmixing is the most critical part of the methods using abundance maps in any step of processing. In the proposed MAP based method, under-estimation of the number of endmembers significantly reduces the performance. Peak performance is achieved when the number of endmembers are correctly determined. Over-smoothing is another problem related to approaches using smoothing for regularization. Nonetheless, over-smoothing problem is successfully solved using a post-processing technique. Instead of adding an edge preserving regularizer to the quadratic function, using post-processing simplifies the minimization problem and removes the parameter tuning for the regularizer. In addition, using abundance maps in the minimization gives robust solutions to the noise problem since spectral unmixing stages decrease the noise in the abundance maps. Therefore, spectral unmixing and abundance maps have been used in noise removal algorithms in recent years [10, 108].

Second method is a novel HS image fusion method. Similarly, proposed fusion method converts the fusion problem to a quadratic optimization problem in the abundance maps domain. Moreover, MAP framework is also included in the optimization. Regularizing the fusion problem with MAP framework gives the ability to overcome the problems of the fusion based methods beyond the visible spectrum and shows superior performance in all the spectral bands throughout the spectrum. The solution of the joint optimization problem is unique and gives the HR abundance maps. Instead of using alternating minimization, joint minimization of abundance maps gives better results in the visible bands as compared to the fusion based methods. Moreover, spectral consistency is preserved throughout the spectrum using MAP framework. Under-estimating the number of endmembers also reduces the performance in the proposed fusion method and performance is satisfactory when the estimated number of endmembers are greater than the actual number of endmembers.

In both methods, HR HS image is reconstructed using the HR abundance maps and spectral signatures of the endmembers. Experimental results show that performance and spectral consistency of the proposed methods are better than the existing state-of-the-art methods.

REFERENCES

[1] Emre Turgay and Gozde B Akar. Texture and edge preserving multiframe super-resolution. *IET Image Processing*, 8(9):499–508, 2014.

[2] RY Tsai and TS Huang. Multiframe image restoration and register. *Advances in Computer Vision and Image Processing, JAL Press Inc*, 1984.

[3] Marco Cristani, Dong Seon Cheng, Vittorio Murino, and Donato Pannullo. Distilling information with super-resolution for video surveillance. In *Proceedings of the ACM 2nd international workshop on Video surveillance & sensor networks*, pages 2–11. ACM, 2004.

[4] Sharon Peled and Yehezkel Yeshurun. Superresolution in mri: application to human white matter fiber tract visualization by diffusion tensor imaging. *Magnetic resonance in medicine*, 45(1):29–35, 2001.

[5] Bahadir K Gunturk, Aziz Umit Batur, Yucel Altunbasak, Monson H Hayes, and Russell M Mersereau. Eigenface-domain super-resolution for face recognition. *IEEE transactions on image processing*, 12(5):597–606, 2003.

[6] Alina Zare and Paul Gader. Hyperspectral band selection and endmember detection using sparsity promoting priors. *IEEE Geoscience and Remote Sensing Letters*, 5(2):256–260, 2008.

[7] Nirmal Keshava. A survey of spectral unmixing algorithms. *Lincoln Laboratory Journal*, 14(1):55–78, 2003.

[8] Liguo Wang and Chunhui Zhao. *Hyperspectral Image Processing*. Springer, 2015.

[9] Miguel Veganzones and Manuel Grana. Endmember extraction methods: A short review. In *Knowledge-Based Intelligent Information and Engineering Systems*, pages 400–407. Springer, 2008.

[10] Daniele Cerra, Rupert Muller, and Peter Reinartz. Noise reduction in hyperspectral images through spectral unmixing. *IEEE Geoscience and Remote Sensing Letters*, 11(1):109–113, 2014.

[11] Pablo J Martínez, Rosa M Pérez, Antonio Plaza, Pedro L Aguilar, María C Cantero, and Javier Plaza. Endmember extraction algorithms from hyperspectral images. 2006.

[12] C Chang. Virtual dimensionality for hyperspectral imagery. *SPIE Newsroom*, 10(2.1200909):1749, 2009.

[13] Wei Xiong, Chein-I Chang, and Ching-Tsorng Tsai. Estimation of virtual dimensionality in hyperspectral imagery by linear spectral mixture analysis. In *Geoscience and Remote Sensing Symposium (IGARSS), 2010 IEEE International*, pages 979–982. IEEE, 2010.

[14] José MP Nascimento and José M Bioucas-Dias. Unsupervised hyperspectral signal subspace identification. In *Seventh Conference on Telecommunications*, volume 1, pages 441–444, 2009.

[15] M Ghamary Asl and B Mojaradi. Virtual dimensionality estimation in hyperspectral imagery based on unsupervised feature selection. *ISPRS Annals of Photogrammetry, Remote Sensing & Spatial Information Sciences*, 3(7), 2016.

[16] Kelly Canham, Ariel Schlamm, Bill Basener, and David Messinger. High spatial resolution hyperspectral spatially adaptive endmember selection and spectral unmixing. In *SPIE Defense, Security, and Sensing*, pages 80481O–80481O. International Society for Optics and Photonics, 2011.

[17] Chein-I Chang and Qian Du. Estimation of number of spectrally distinct signal sources in hyperspectral imagery. *IEEE Transactions on geoscience and remote sensing*, 42(3):608–619, 2004.

[18] JC Harsanyi, WH Farrand, and Chein-I Chang. Determining the number and identity of spectral endmembers: an integrated approach using neyman-pearson eigen-thresholding and iterative constrained rms error minimization. In *Proceedings of the Thematic Conference on Geologic Remote Sensing*, volume 1, pages 395–395. Enviromental Research Institute of Michigan, 1993.

[19] José M Bioucas-Dias and José MP Nascimento. Hyperspectral subspace identification. *IEEE Transactions on Geoscience and Remote Sensing*, 46(8):2435–2445, 2008.

[20] Farzeen Chaudhry, Chao-Cheng Wu, Weimin Liu, Chein-I Chang, and Antonio Plaza. Pixel purity index-based algorithms for endmember extraction from hyperspectral imagery. *Recent advances in hyperspectral signal and image processing*, 37(2):29–62, 2006.

[21] Chein-I Chang. *Hyperspectral data processing: algorithm design and analysis*. John Wiley & Sons, 2013.

[22] Hsuan Ren and Chein-I Chang. Automatic spectral target recognition in hyperspectral imagery. *IEEE Transactions on Aerospace and Electronic Systems*, 39(4):1232–1249, 2003.

[23] Michael E Winter. N-findr: An algorithm for fast autonomous spectral endmember determination in hyperspectral data. In *SPIE's International Symposium on Optical Science, Engineering, and Instrumentation*, pages 266–275. International Society for Optics and Photonics, 1999.

[24] José MP Nascimento and José MB Dias. Vertex component analysis: A fast algorithm to unmix hyperspectral data. *IEEE transactions on Geoscience and Remote Sensing*, 43(4):898–910, 2005.

[25] José M Bioucas-Dias. A variable splitting augmented lagrangian approach to linear spectral unmixing. In *Hyperspectral Image and Signal Processing: Evolution in Remote Sensing, 2009. WHISPERS'09. First Workshop on*, pages 1–4. IEEE, 2009.

[26] Mark Berman, Harri Kiiveri, Ryan Lagerstrom, Andreas Ernst, Rob Dunne, and Jonathan F Huntington. Ice: A statistical approach to identifying endmembers in hyperspectral images. *IEEE transactions on Geoscience and Remote Sensing*, 42(10):2085–2095, 2004.

[27] Alina Zare and Paul Gader. Sparsity promoting iterated constrained endmember detection in hyperspectral imagery. *IEEE Geoscience and Remote Sensing Letters*, 4(3):446–450, 2007.

[28] Seniha Esen Yuksel, Sefa Kucuk, and Paul D Gader. Spicee: An extension of spice for sparse endmember estimation in hyperspectral imagery. *IEEE Geoscience and Remote Sensing Letters*, 13(12):1910–1914, 2016.

[29] Guoxu Zhou, Shengli Xie, Zuyuan Yang, Jun-Mei Yang, and Zhaoshui He. Minimum-volume-constrained nonnegative matrix factorization: Enhanced ability of learning parts. *IEEE transactions on neural networks*, 22(10):1626–1637, 2011.

[30] Daniel C Heinz et al. Fully constrained least squares linear spectral mixture analysis method for material quantification in hyperspectral imagery. *IEEE transactions on geoscience and remote sensing*, 39(3):529–545, 2001.

[31] Xue-fen Wan and Yi Yang. Super-resolution image reconstruction. In *Computer Application and System Modeling (ICCASM), 2010 International Conference on*, volume 8, pages V8–351. IEEE, 2010.

[32] Jianchao Yang and Thomas Huang. Image super-resolution: Historical overview and future challenges. *Super-resolution imaging*, pages 20–34, 2010.

[33] Danny Keren, Shmuel Peleg, and Rafi Brada. Image sequence enhancement using sub-pixel displacements. In *Computer Vision and Pattern Recognition, 1988. Proceedings CVPR'88., Computer Society Conference on*, pages 742–746. IEEE, 1988.

[34] Matan Protter and Michael Elad. Super resolution with probabilistic motion estimation. *IEEE Transactions on Image Processing*, 18(8):1899–1904, 2009.

[35] JJ Clark, MR Palmer, and PD Lawrence. A transformation method for the reconstruction of functions form nonuniformly spaced samples. *IEEE Trans. On Acoustics, Speech, and Signal Processing*, pages 1151–1165.

[36] SP Kim, Nirmal K Bose, and HM Valenzuela. Recursive reconstruction of high resolution image from noisy undersampled multiframes. *IEEE Transactions on Acoustics, Speech, and Signal Processing*, 38(6):1013–1027, 1990.

[37] Michael E Tipping, Christopher M Bishop, et al. Bayesian image super-resolution. In *NIPS*, volume 15, pages 1279–1286, 2002.

[38] Richard R Schultz and Robert L Stevenson. Extraction of high-resolution frames from video sequences. *IEEE transactions on image processing*, 5(6):996–1011, 1996.

[39] Lyndsey C Pickup, David P Capel, Stephen J Roberts, and Andrew Zisserman. Bayesian image super-resolution, continued. In *NIPS*, volume 19, 2006.

[40] Giannis Chantas, Nikolaos P Galatsanos, Rafael Molina, and Aggelos K Katsaggelos. Variational bayesian image restoration with a product of spatially weighted total variation image priors. *IEEE transactions on image processing*, 19(2):351–362, 2010.

[41] Andrew Blake, Pushmeet Kohli, and Carsten Rother. *Markov random fields for vision and image processing*. Mit Press, 2011.

[42] Russell C Hardie, Kenneth J Barnard, and Ernest E Armstrong. Joint map registration and high-resolution image estimation using a sequence of undersampled images. *IEEE Transactions on Image Processing*, 6(12):1621–1633, 1997.

[43] Michal Irani and Shmuel Peleg. Improving resolution by image registration. *CVGIP: Graphical models and image processing*, 53(3):231–239, 1991.

[44] Michal Irani and Shmuel Peleg. Motion analysis for image enhancement: Resolution, occlusion, and transparency. *Journal of Visual Communication and Image Representation*, 4(4):324–335, 1993.

[45] Milan N Bareja and Chintan K Modi. An effective iterative back projection based single image super resolution approach. In *Communication Systems and Network Technologies (CSNT), 2012 International Conference on*, pages 95–99. IEEE, 2012.

[46] Anil B Gavade and Vijay S Rajpurohit. A survey on image reconstruction using super resolution.

[47] Henry Stark and Peyma Oskoui. High-resolution image recovery from image-plane arrays, using convex projections. *JOSA A*, 6(11):1715–1726, 1989.

[48] A Murat Tekalp, Mehmet K Ozkan, and M Ibrahim Sezan. High-resolution image reconstruction from lower-resolution image sequences and space-varying image restoration. In *Acoustics, Speech, and Signal Processing, 1992. ICASSP-92., 1992 IEEE International Conference on*, volume 3, pages 169–172. IEEE, 1992.

[49] Michael Elad and Arie Feuer. Restoration of a single superresolution image from several blurred, noisy, and undersampled measured images. *IEEE transactions on image processing*, 6(12):1646–1658, 1997.

[50] William T Freeman, Thouis R Jones, and Egon C Pasztor. Example-based super-resolution. *IEEE Computer graphics and Applications*, 22(2):56–65, 2002.

[51] Sanket B Kasturiwala and SA Ladhake. Patch based image superresolution: application to leaf diseased image. 2013.

[52] M Valvi Jignasha and Chirag N Paunwala. Learning based single frame super-resolution using lorentzian error norm & gabor filter. In *Signal Processing, Computing and Control (ISPCC), 2013 IEEE International Conference on*, pages 1–6. IEEE, 2013.

[53] Dai-Viet Tran, Sébastien Li-Thiao-Té, Marie Luong, Thuong Le-Tien, Françoise Dibos, and Jean-Marie Rocchisani. Example-based super-resolution for enhancing spatial resolution of medical images. In *Engineering in Medicine and Biology Society (EMBC), 2016 IEEE 38th Annual International Conference of the*, pages 457–460. IEEE, 2016.

[54] Hong Chang, Dit-Yan Yeung, and Yimin Xiong. Super-resolution through neighbor embedding. In *Computer Vision and Pattern Recognition, 2004. CVPR 2004. Proceedings of the 2004 IEEE Computer Society Conference on*, volume 1, pages I–I. IEEE, 2004.

[55] Toygar Akgun, Yucel Altunbasak, and Russell M Mersereau. Super-resolution reconstruction of hyperspectral images. *IEEE Transactions on Image Processing*, 14(11):1860–1875, 2005.

[56] Lijuan Su, Shubo Zhou, and Yan Yuan. High spatial resolution image restoration from subpixel-shifted hyperspectral images. *Journal of Applied Remote Sensing*, 9(1):095093–095093, 2015.

[57] Jonathan Cheung-Wai Chan, Jianglin Ma, and Frank Canters. A comparison of superresolution reconstruction methods for multi-angle chris/proba images. In *SPIE Remote Sensing*, pages 710904–710904. International Society for Optics and Photonics, 2008.

[58] Xiong Xu, Xiaohua Tong, Jie Li, Huan Xie, Yanfei Zhong, Liangpei Zhang, and Dongmei Song. Hyperspectral image super resolution reconstruction with a joint spectral-spatial sub-pixel mapping model. In *Geoscience and Remote Sensing Symposium (IGARSS), 2016 IEEE International*, pages 6129–6132. IEEE, 2016.

[59] Alberto Villa, Jocelyn Chanussot, Jon Atli Benediktsson, M Ulfarsson, and Christian Jutten. Super-resolution: an efficient method to improve spatial resolution of hyperspectral images. In *Geoscience and Remote Sensing Symposium (IGARSS), 2010 IEEE International*, pages 2003–2006. IEEE, 2010.

[60] Alp Ertürk, Mehmet Kemal Güllü, Davut Çeşmeci, Deniz Gerçek, and Sarp Ertürk. Spatial resolution enhancement of hyperspectral images using unmixing and binary particle swarm optimization. *IEEE Geoscience and Remote Sensing Letters*, 11(12):2100–2104, 2014.

[61] B Msellmi, ZB Rabah, and IR Farah. Super-resolution algorithm based on sub-pixels spatial correlation for hyperspectral image classification. In *Advanced Technologies for Signal and Image Processing (ATSIP), 2016 2nd International Conference on*, pages 613–618. IEEE, 2016.

[62] Zhaohui Guo, Todd Wittman, and Stanley Osher. L1 unmixing and its application to hyperspectral image enhancement. In *SPIE Defense, Security, and Sensing*, pages 73341M–73341M. International Society for Optics and Photonics, 2009.

[63] Shiying He, Haiwei Zhou, Yao Wang, Wenfei Cao, and Zhi Han. Super-resolution reconstruction of hyperspectral images via low rank tensor modeling and total variation regularization. In *Geoscience and Remote Sensing Symposium (IGARSS), 2016 IEEE International*, pages 6962–6965. IEEE, 2016.

[64] Teerasit Kasetkasem, Manoj K Arora, and Pramod K Varshney. Super-resolution land cover mapping using a markov random field based approach. *Remote Sensing of Environment*, 96(3):302–314, 2005.

[65] Fereidoun A Mianji, Ye Zhang, Humayun Karim Sulehria, Asad Babakhani, and Mohammad Reza Kardan. Super-resolution challenges in hyperspectral imagery. *Information Technology Journal*, 7(7):1030–1036, 2008.

[66] Stephen Boyd. Alternating direction method of multipliers. In *Talk at NIPS Workshop on Optimization and Machine Learning*, 2011.

[67] Hasan Irmak, Gözde B Akar, and Seniha Esen Yüksel. A map-based approach to resolution enhancement of hyperspectral images. In *Workshop on Hyperspectral Image and Signal Processing: Evolution in Remote Sensing (WHISPERS)*, pages 1–4, 2015.

[68] Hasan Irmak, Gözde Bozdağı Akar, and Seniha Esen Yüksel. Hyperspectral imagery superresolution. In *Signal Processing and Communication Application Conference (SIU), 2016 24th*, pages 1057–1060. IEEE, 2016.

[69] Hasan Irmak, Gözde B Akar, Seniha Esen Yuksel, and Hakan Aytaylan. Super-resolution reconstruction of hyperspectral images via an improved map-based approach. In *Geoscience and Remote Sensing Symposium (IGARSS), 2016 IEEE International*, pages 7244–7247. IEEE, 2016.

[70] Fereidoun A Mianji, Yanfeng Gu, Ye Zhang, and Junping Zhang. Enhanced self-training superresolution mapping technique for hyperspectral imagery. *IEEE Geoscience and Remote Sensing Letters*, 8(4):671–675, 2011.

[71] Andrew J Tatem, Hugh G Lewis, Peter M Atkinson, and Mark S Nixon. Super-resolution land cover pattern prediction using a hopfield neural network. *Remote Sensing of Environment*, 79(1):1–14, 2002.

[72] Yuan Yuan, Xiangtao Zheng, and Xiaoqiang Lu. Hyperspectral image super-resolution by transfer learning. *IEEE Journal of Selected Topics in Applied Earth Observations and Remote Sensing*, 2017.

[73] Huijuan Huang, Anthony G Christodoulou, and Weidong Sun. Super-resolution hyperspectral imaging with unknown blurring by low-rank and group-sparse modeling. In *Image Processing (ICIP), 2014 IEEE International Conference on*, pages 2155–2159. IEEE, 2014.

[74] Massimo Fornasier and Holger Rauhut. Compressive sensing. In *Handbook of mathematical methods in imaging*, pages 187–228. Springer, 2011.

[75] Murat Şimşek and Ediz Polat. Sparse representation-based dictionary learning methods for hyperspectral super-resolution. In *Signal Processing and Communication Application Conference (SIU), 2016 24th*, pages 753–756. IEEE, 2016.

[76] Yun Zhang. Understanding image fusion. *Photogrammetric engineering and remote sensing*, 70(6):657–661, 2004.

[77] Jan Flusser, Filip Sroubek, and Barbara Zitova. Image fusion: principles, methods, and applications. *Tutorial Eusipco*, 2007.

[78] Naoto Yokoya, Claas Grohnfeldt, and Jocelyn Chanussot. Hyperspectral and multispectral data fusion: A comparative review. *IEEE Geoscience and Remote Sensing Magazine (GRSM)*, 2017.

[79] Janja Avbelj, Dorota Iwaszczuk, Rupert Müller, Peter Reinartz, and Uwe Stilla. Line-based registration of dsm and hyperspectral images. *Int. Arch. Photogramm. Remote Sens. Spatial Inf. Sci.*, 40:13–18, 2013.

[80] A Ardeshir Goshtasby and Jacqueline Le Moigne. Special issue on image registration. *Pattern Recognition*, 32(1), 1999.

[81] Laetitia Loncan, Luis B de Almeida, José M Bioucas-Dias, Xavier Briottet, Jocelyn Chanussot, Nicolas Dobigeon, Sophie Fabre, Wenzhi Liao, Giorgio A Licciardi, Miguel Simoes, et al. Hyperspectral pansharpening: A review. *IEEE Geoscience and remote sensing magazine*, 3(3):27–46, 2015.

[82] Gemine Vivone, Rocco Restaino, Giorgio Licciardi, Mauro Dalla Mura, and Jocelyn Chanussot. Multiresolution analysis and component substitution techniques for hyperspectral pansharpening. In *Geoscience and remote sensing symposium (IGARSS), 2014 IEEE international*, pages 2649–2652. IEEE, 2014.

[83] Claire Thomas, Thierry Ranchin, Lucien Wald, and Jocelyn Chanussot. Synthesis of multispectral images to high spatial resolution: A critical review of fusion methods based on remote sensing physics. *IEEE Transactions on Geoscience and Remote Sensing*, 46(5):1301–1312, 2008.

[84] Bruno Aiazzi, Stefano Baronti, and Massimo Selva. Improving component substitution pansharpening through multivariate regression of ms + pan data. *IEEE Transactions on Geoscience and Remote Sensing*, 45(10):3230–3239, 2007.

[85] JG Liu. Smoothing filter-based intensity modulation: A spectral preserve image fusion technique for improving spatial details. *International Journal of Remote Sensing*, 21(18):3461–3472, 2000.

[86] Kaiming He, Jian Sun, and Xiaoou Tang. Guided image filtering. *IEEE transactions on pattern analysis and machine intelligence*, 35(6):1397–1409, 2013.

[87] Naoto Yokoya, Takehisa Yairi, and Akira Iwasaki. Coupled nonnegative matrix factorization unmixing for hyperspectral and multispectral data fusion. *IEEE Transactions on Geoscience and Remote Sensing*, 50(2):528–537, 2012.

[88] Charis Lanaras, Emmanuel Baltsavias, and Konrad Schindler. Hyperspectral super-resolution by coupled spectral unmixing. In *Proceedings of the IEEE International Conference on Computer Vision*, pages 3586–3594, 2015.

[89] Russell C Hardie, Michael T Eismann, and Gregory L Wilson. Map estimation for hyperspectral image resolution enhancement using an auxiliary sensor. *IEEE Transactions on Image Processing*, 13(9):1174–1184, 2004.

[90] Michael Theodore Eismann. *Resolution enhancement of hyperspectral imagery using maximum a posteriori estimation with a stochastic mixing model.* 2004.

[91] Miguel Simões, José Bioucas-Dias, Luis B Almeida, and Jocelyn Chanussot. A convex formulation for hyperspectral image superresolution via subspace-based regularization. *IEEE Transactions on Geoscience and Remote Sensing*, 53(6):3373–3388, 2015.

[92] Marian-Daniel Iordache, José M Bioucas-Dias, and Antonio Plaza. Total variation spatial regularization for sparse hyperspectral unmixing. *IEEE Transactions on Geoscience and Remote Sensing*, 50(11):4484–4502, 2012.

[93] Javier Plaza, Eligius MT Hendrix, Inmaculada García, Gabriel Martín, and Antonio Plaza. On endmember identification in hyperspectral images without pure pixels: A comparison of algorithms. *Journal of Mathematical Imaging and Vision*, 42(2):163–175, 2012.

[94] Heinz Werner Engl, Martin Hanke, and Andreas Neubauer. *Regularization of inverse problems*, volume 375. Springer Science & Business Media, 1996.

[95] Stan Z Li. *Markov random field modeling in image analysis*. Springer Science & Business Media, 2009.

[96] S Li. Markov random field models in computer vision. *Computer Vision—ECCV'94*, pages 361–370, 1994.

[97] David L. Jensen and Alan J. King. A decomposition method for quadratic programming. *IBM systems journal*, 31(1):39–48, 1992.

[98] Thomas Reslow Kruth. Interior-point algorithms for quadratic programming. Master's thesis, Technical University of Denmark, DTU, DK-2800 Kgs. Lyngby, Denmark, 2008.

[99] Alain Hore and Djemel Ziou. Image quality metrics: Psnr vs. ssim. In *Pattern Recognition (ICPR), 2010 20th International Conference on*, pages 2366–2369. IEEE, 2010.

[100] Zhou Wang, Alan C Bovik, Hamid R Sheikh, and Eero P Simoncelli. Image quality assessment: from error visibility to structural similarity. *IEEE transactions on image processing*, 13(4):600–612, 2004.

[101] Nirmal Keshava. Distance metrics and band selection in hyperspectral processing with applications to material identification and spectral libraries. *IEEE Transactions on Geoscience and remote sensing*, 42(7):1552–1565, 2004.

[102] S Rashmi, A Swapna, S Venkat, and S Ravikiran. Spectral angle mapper algorithm for remote sensing image classification. *IJISET–International Journal of Innovative Science, Engineering & Technology*, 50(4):201–205, 2014.

[103] Tania Stathaki. *Image fusion: algorithms and applications*. Academic Press, 2011.

[104] Fumihito Yasuma, Tomoo Mitsunaga, Daisuke Iso, and Shree K Nayar. Generalized assorted pixel camera: postcapture control of resolution, dynamic range, and spectrum. *IEEE transactions on image processing*, 19(9):2241–2253, 2010.

[105] Ayan Chakrabarti and Todd Zickler. Statistics of real-world hyperspectral images. In *Computer Vision and Pattern Recognition (CVPR), 2011 IEEE Conference on*, pages 193–200. IEEE, 2011.

[106] Hyperspectral remote sensing scenes. `http://www.ehu.eus/ccwintco/index.php?title=Hyperspectral_Remote_Sensing_Scenes`. (Date last accessed 05-Sept-2016).

[107] Fan Yang, Don Xie, Huizhu Jia, Rui Chen, Guoqing Xiang, and Wen Gao. Structure preserving single image super-resolution. In *Image Processing (ICIP), 2016 IEEE International Conference on*, pages 1409–1413. IEEE, 2016.

[108] Alp Ertürk. Denoising in hyperspectral images by superpixel based unmixing. In *Signal Processing and Communication Application Conference (SIU), 2016 24th*, pages 2189–2192. IEEE, 2016.

CURRICULUM VITAE

PERSONAL INFORMATION

Surname, Name: IRMAK, Hasan

Nationality: Turkish (TC)

Date and Place of Birth: 02.02.1985, ANKARA

Marital Status: Married

Phone: 0 505 6231792

e-mail: hasan.irmak@metu.edu.tr

EDUCATION

Degree	Institution	Year
M.S.	Electrical and Electronics Engineering Department, METU	2010
B.S. Minor	Computer Engineering Department, METU	2008
B.S.	Electrical and Electronics Engineering Department, METU	2008
High School	Ankara Gölbaşı Anatolian High School	2003

PROFESSIONAL EXPERIENCE

Year	Place	Enrollment
2008-2010	Aselsan/MGEO	Digital Design Engineer
2011-2017	Aselsan/REHİS	Digital Design Engineer

PUBLICATIONS

International Conference Publications, Oral Presentations

- H. Irmak, G. B. Akar, and S. E. Yuksel, "A map-based approach to resolution enhancement of hyperspectral images," in *IEEE workshop on hyperspectral image and signal processing (WHISPERS).* IEEE, 2015
- H. Irmak, G. B. Akar, S. E. Yuksel, and H. Aytaylan, "Superresolution reconstruction of hyperspectral images via an improved map-based approach," in *2016 IEEE International Geoscience and Remote Sensing Symposium (IGARSS).* IEEE, 2016.

National Conference Publications, Oral Presentations

- H. Irmak, G. B. Akar, and S. E. Yuksel, "Hiperspektral görüntülerde süperçözünürlük," *24. Sinyal İşleme ve İletişim Uygulamaları Kurultayı (SIU)* IEEE, 2016, pp.1057–1060
- H. Yalcin, H. Irmak, M. M. Bulut, and G. B. Akar, "Real-time Traffic Sign detection and Recognition on FPGA," *21. Sinyal İşleme ve İletişim Uygulamaları Kurultayı (SIU).* IEEE, 2013, pp. 1–4.

Submitted Journal Publications

- H. Irmak, G. B. Akar, and S. E. Yuksel, "A map-based approach for Hyperspectral imagery super-resolution in *IEEE Transactions on Image Processing* **(Major Revision)**